



**HAL**  
open science

# Imaging the changes in electronic structure across phase transitions in the strongly correlated materials V O and URu Si

Maximilian Thees

► **To cite this version:**

Maximilian Thees. Imaging the changes in electronic structure across phase transitions in the strongly correlated materials V O and URu Si . Strongly Correlated Electrons [cond-mat.str-el]. Université Paris-Saclay, 2022. English. NNT : 2022UPASP069 . tel-03890768

**HAL Id: tel-03890768**

**<https://theses.hal.science/tel-03890768>**

Submitted on 8 Dec 2022

**HAL** is a multi-disciplinary open access archive for the deposit and dissemination of scientific research documents, whether they are published or not. The documents may come from teaching and research institutions in France or abroad, or from public or private research centers.

L'archive ouverte pluridisciplinaire **HAL**, est destinée au dépôt et à la diffusion de documents scientifiques de niveau recherche, publiés ou non, émanant des établissements d'enseignement et de recherche français ou étrangers, des laboratoires publics ou privés.

Imaging the changes in electronic  
structure across phase transitions in the  
strongly correlated materials  $V_2O_3$  and  
 $URu_2Si_2$

*Visualisation des changements de la structure électronique  
lors des transitions de phase dans les matériaux fortement  
corrélés  $V_2O_3$  et  $URu_2Si_2$*

**Thèse de doctorat de l'université Paris-Saclay**

École doctorale n°564: physique en Île-de-France (PIF)  
Spécialité de doctorat: Physique  
Graduate School: Physique  
Réfèrent: Faculté des sciences d'Orsay

Thèse préparée à l'**Institut des Sciences Moléculaires d'Orsay** (Université Paris-Saclay, CNRS), sous la direction d'**Andrés Felipe SANTANDER-SYRO**,  
Maître de conférences (HDR)

**Thèse soutenue à Paris-Saclay, le 5 juillet 2022**

**Maximilian Peter Tassilo THEES**

**Composition du jury**

<b>Odile STÉPHAN</b> Professeure, Université Paris-Saclay	Présidente
<b>Rolf MÖLLER</b> Professeur, Universität Duisburg-Essen	Rapporteur & Examineur
<b>Marie d'ANGELO</b> Maîtresse de conférences (HDR), Sorbonne Université	Rapporteuse & Examinatrice
<b>Roser VALENTI</b> Professeure, Goethe-Universität Frankfurt am Main	Examinatrice
<b>Elena BASCONES</b> Directrice de recherche, Directrice de recherche Instituto de Ciencia de Materiales de Madrid, CSIC	Examinatrice
<b>Andrés Felipe SANTANDER-SYRO</b> Maître de conférences (HDR), Université Paris-Saclay	Directeur de thèse

**Titre:** Visualisation des changements de la structure électronique lors des transitions de phase dans les matériaux fortement corrélés  $V_2O_3$  et  $URu_2Si_2$

**Mots clés:** systèmes d'électrons fortement corrélés, fermions lourds, transitions de phase, structure électronique, ARPES

**Résumé:** Les systèmes d'électrons fortement corrélés peuvent présenter différents états fondamentaux concurrents, conduisant à des transitions de phase vers des états exotiques de la matière. Cette thèse explore expérimentalement, en utilisant la spectroscopie de photoémission résolue en angle (ARPES), les changements de structure électronique à travers deux transitions de phase paradigmatiques des matériaux corrélés: la transition métal-isolant de Mott en fonction de la température dans  $V_2O_3$  et la transition critique quantique en fonction du dopage dans  $URu_2Si_2$ .

Dans le  $V_2O_3$  volumique, une transition métal-isolant (TMI) de premier ordre se produit à une température de transition de  $T_{TMI} \approx 160$  K, caractérisée par une forte augmentation de la résistivité de plus de 6 ordres de grandeur et l'ouverture d'un gap électronique d'environ 750 meV au niveau de Fermi. Cette thèse présente une étude complète des changements de la structure électronique à travers la TMI induite par la température dans des films de  $V_2O_3$ , dont l'intégrité cristalline, contrairement aux monocristaux, n'est pas affectée par la transition.

Les résultats montrent des bandes dispersives de quasi-particules et de Mott-Hubbard dans l'état métallique, ainsi que des signatures spectrales uniques, différentes de celles d'une instabilité conventionnelle de la surface de Fermi, accompagnant la TMI: l'ouverture d'un gap au niveau de Fermi, associé à une diminution du poids spectral de la bande de quasi-particules, sans aucun changement de sa masse effective. La bande de Mott-Hubbard reste par ailleurs non affectée par la TMI. Le poids spectral de la bande de quasi-particules est transféré à une bande non dispersive, de caractère orbital différent, dont l'énergie de liaison diminue à mesure que son poids spectral augmente. En outre, les données montrent une hystérésis thermique dans la gap et le poids spectral de la bande de quasi-particule, ce qui est interprété en termes

de l'évolution de la concentration des domaines microscopiques métalliques/isolants, et qui capture quantitativement l'hystérésis de la résistivité mesurée dans les mêmes échantillons.

L' $URu_2Si_2$  subit quant à lui une transition de phase à 17,5 K, dont le paramètre d'ordre est encore inconnu trois décennies après sa première observation dans des mesures de chaleur spécifique. La température de transition peut être abaissée par un dopage au phosphore jusqu'à sa suppression totale à un point critique quantique. Un dopage encore plus fort donne naissance à un état fondamental antiferromagnétique. Les transitions induites par le dopage sont intéressantes d'un point de vue fondamental: Une transition de phase continue au zéro absolu implique une criticité quantique, où la transition vers le nouveau état fondamental ne peut pas être induite par des excitations thermique comme dans les transitions de phase conventionnelles, et nécessite plutôt les fluctuations quantiques du point zéro dues à l'incertitude d'Heisenberg. Cette thèse présente des mesures ARPES de la structure électronique de l' $URu_2Si_2$  à travers les transitions à température constante depuis l'ordre caché (HO) vers la phase paramagnétique (PM) et ensuite vers la phase antiferromagnétique (AFM) induites par le dopage au phosphore. Il est constaté que les changements de la structure électronique autour du point Gamma entre ces phases s'apparentent à ceux rapportés précédemment pour les transitions HO-PM-AFM purement induites par la température. De plus, au point X, nous observons que le dopage en phosphore induit des changements importants dans la dispersion d'un état de surface de type trou et la suppression de son hybridation avec la bande de quasi-particules U-5f dans l'état paramagnétique, contrairement au cas de la transition induite par la température, indiquant qu'une telle hybridation est une caractéristique unique de la phase d'ordre caché.

**Title:** Imaging the changes in electronic structure across phase transitions in the strongly correlated materials  $V_2O_3$  and  $URu_2Si_2$

**Keywords:** Strongly correlated electron systems, heavy fermions, phase transitions, electronic structure, ARPES

**Abstract:** In systems with strongly correlated electrons, different competing ground states can lead to exotic states of matter and new phase transitions. This thesis explores experimentally, using angle-resolved photoelectron spectroscopy (ARPES), how the electronic structure changes across two such paradigmatic transitions: the Mott metal-to-insulator transition as a function of temperature in  $V_2O_3$  and the quantum phase transition as a function of doping in  $URu_2Si_2$ .

In bulk  $V_2O_3$ , a first-order Metal-to-Insulator Transition occurs at a transition temperature of  $T_{MIT} \approx 160$  K, as evidenced by a sharp rise in resistivity of more than 6 orders of magnitude and the opening of a gap of about 750 meV. The thesis presents a comprehensive study of the electronic structure using angle-resolved photoemission spectroscopy (ARPES), across the temperature-induced MIT in  $V_2O_3$  films, whose crystal integrity, contrary to single crystals, is not affected by the transition.

The results show dispersive quasi-particle and Mott-Hubbard bands in the metallic state, and the observation of unique spectral signatures, different to those of a conventional Fermi-surface instability, accompanying the MIT: the opening of a gap at the Fermi level associated to a decrease in spectral weight of the quasiparticle band, without any change in its effective mass, while the Mott-Hubbard-band remains unaffected by the MIT. The spectral weight is transferred from the conduction band to a non-dispersive band of different orbital character, as the latter moves down in binding energy. Furthermore a clear thermal hysteresis in the gap and the quasi-particle's spectral weight is observed, which is interpreted in terms of the evo-

lution of ratios of metallic/insulating microscopic domains, and that precisely capture the hysteresis in resistivity measured in the same samples.

$URu_2Si_2$  undergoes a phase transition at 17.5 K, whose order parameter is still unknown to researchers over three decades after its first observation in specific heat measurements. The transition temperature can be lowered by phosphorous doping up to its suppression at a quantum-critical point. Stronger doping then gives rise to an antiferromagnetic ground state. The doping-induced transitions are of interest on a fundamental level: A continuous phase transition at absolute zero implies quantum criticality, where the transition into the new ground state cannot be driven by thermal excitations like in conventional first order phase transitions, and requires instead zero-point fluctuations due to Heisenberg uncertainty.

This thesis presents angle-resolved photoemission spectroscopy measurements of the electronic structure of  $URu_2Si_2$  across the transitions from the low temperature hidden order (HO) to the paramagnetic and then into the antiferromagnetic phase driven by Phosphorous doping. It is found that the changes in electronic structure around the Gamma high symmetry point, that have been previously reported across a purely temperature-driven Hidden Order transition, can be reproduced by the doping, independently of temperature. Furthermore, at the X-point, strong changes in the dispersion of a hole-like surface state and suppression of its hybridization with the U5f-quasiparticle band in the paramagnetic state are observed with the doping, in contrast to the temperature-driven transition, indicating that such hybridization is a unique feature of the hidden order phase.



# Contents

<b>1</b>	<b>Introduction</b>	<b>7</b>
<b>2</b>	<b>A Short Tale of Band Theory and Phase Transitions</b>	<b>9</b>
2.1	Classical Band Theory . . . . .	9
2.1.1	From Bands in Independent-Electron Systems to Electronic States in Strongly Correlated Systems . . . . .	9
2.1.2	Reciprocal Space and Band Structure . . . . .	10
2.2	Strong Correlations . . . . .	11
2.2.1	Hybridization . . . . .	11
2.2.2	The Mott-transition . . . . .	12
2.3	Phase Transitions . . . . .	14
2.3.1	Of Phases and Ordering . . . . .	14
2.3.2	1st and 2nd Order Transitions . . . . .	15
2.3.3	Critical Points . . . . .	16
2.3.4	Crystal Growth Phases . . . . .	16
2.3.5	Quantum Criticality . . . . .	17
<b>3</b>	<b>Photoelectron Spectroscopy 101</b>	<b>21</b>
3.1	Photoelectron Spectroscopy . . . . .	21
3.1.1	The Photoelectric Effect . . . . .	21
3.1.2	Core Level Spectroscopy . . . . .	21
3.1.3	Three-Step Model . . . . .	22
3.2	Angle Resolution . . . . .	26
3.2.1	Conservation of Momentum . . . . .	26
3.3	ARPES in Practice . . . . .	28
3.3.1	General Constraints to the Experiment . . . . .	28
3.3.2	Reciprocal Space in 3 Dimensions and Fermi Surface Measurements . . . . .	29
3.3.3	Light Sources . . . . .	30
3.3.4	Hemispherical Analysers . . . . .	30
3.3.5	Geometry and Systems of Reference . . . . .	31
<b>4</b>	<b>The Metal-to-Insulator Transition of <math>V_2O_3</math></b>	<b>33</b>
4.1	Previous Work . . . . .	33
4.1.1	Crystal Structure . . . . .	33
4.1.2	Phase Diagram . . . . .	33
4.1.3	Focus on the Triple-Transition . . . . .	34
4.2	Methods . . . . .	40
4.2.1	Thin Films . . . . .	40
4.2.2	Annealing and Preparation . . . . .	40

4.2.3	Temperature Cycles at KEK and Cassiopee . . . . .	42
4.3	Results . . . . .	45
4.3.1	Reproducibility of Results in the Paramagnetic Metal Phase . . . . .	45
4.3.2	Spectral Weight Transfer . . . . .	49
4.3.3	Correlation Between Resistivity Changes and Spectral Weight Transfer . . . . .	54
4.3.4	The Spectral Weight Transfer and Lack of Symmetry Changes . . . . .	56
4.3.5	Lack of Oxidation State Changes . . . . .	57
<b>5</b>	<b>Driving the Hidden Order Transition in URu<sub>2</sub>Si<sub>2</sub> by P-doping</b>	<b>59</b>
5.1	Previous Work . . . . .	59
5.1.1	Basic Information about URu <sub>2</sub> Si <sub>2</sub> . . . . .	59
5.1.2	The Electronic Structure in the Paramagnetic and Hidden Order Phases . . . . .	64
5.1.3	Phosphorous Doping . . . . .	67
5.2	Our Experiments . . . . .	67
5.2.1	Our Samples . . . . .	67
5.2.2	Experimental Methods . . . . .	67
5.3	Results . . . . .	69
5.3.1	Fermi Surface Changes around Gamma . . . . .	69
5.3.2	Hybridisation Changes around X . . . . .	71
<b>6</b>	<b>Perspectives</b>	<b>75</b>
6.1	Vanadates . . . . .	75
6.1.1	Further Experiments on the Phase Transitions of V <sub>2</sub> O <sub>3</sub> . . . . .	75
6.1.2	The Metal-to-Insulator Transitions of other Vanadates . . . . .	76
6.2	The Hidden Order . . . . .	76
<b>7</b>	<b>Conclusion</b>	<b>77</b>
<b>8</b>	<b>Acknowledgements</b>	<b>79</b>
<b>9</b>	<b>Annex</b>	<b>81</b>
9.1	Software for Modelling Brillouin Zone Symmetries in Igor Pro . . . . .	81
<b>10</b>	<b>Synthèse en Français</b>	<b>105</b>
10.1	Motivation . . . . .	105
10.2	Cadre Théorique . . . . .	105
10.3	V <sub>2</sub> O <sub>3</sub> . . . . .	106
10.4	URu <sub>2</sub> Si <sub>2</sub> . . . . .	107

# 1 - Introduction

La science, mon garçon, est faite d'erreurs, mais d'erreurs qu'il est bon de commettre, car elles mènent peu à peu à la vérité.

---

Jules Verne, *Voyage au Centre de la Terre*

From its inception in works of Aristotle to the development of quantum mechanics and relativity, physics has sought to reveal the fundamental principles of nature. The idea that any system is assembled of basic building blocks like the elementary particles of the Standard model led physicists to believe that once these principles were known, the physics of any system would become evident, or just the result of a profane application of *ab initio* methods, and a scientist knowing these basic principles would therefore be omniscient.

With the discovery of quantum mechanics, this changed. As scientists realized the sheer complexity of a large number of interacting particles is prohibitive to such an approach, and the idea of a model that makes the universe evident at all scales had to be abandoned. The reductionist hypothesis, stating that a few fundamental principles dictate the physics across all scales, is not invalidated by this, and nearly undisputed among physicists. The fundamental laws' usefulness to predict the behaviour of large systems, however, is severely limited, causing scientists to search for alternative approaches to make such predictions. This search led to the emergence of statistical and many-body physics, and the notion of collective phenomena being treated as a new kind of physics is described concisely in Philip W. Anderson's famous dictum "More is different" [1].

A testament to how powerful a concept many-body physics is lies in how the advances in computational power of the last decades have not only been employed in resurgence of *ab-initio* methods, but led to the rise of dynamical mean-field theory as a prevalent tool and to the development of experimental techniques, such as angle-resolved photoemission spectroscopy, to tackle the fundamental aspects of quantum-mechanical many-body systems.

This thesis tries to give a small, experimental contribution to our understanding of two of these emerging phenomena: The Metal-to-Insulator transition in  $V_2O_3$  and the quantum phase transitions in  $URu_2Si_2$ . It is structured into six main chapters:

- Chapter 2 gives a short overview over aspects of band theory and phase transitions that are relevant to the work
- Chapter 3 is an introduction to angle-resolved photoelectron spectroscopy, the primary experimental method for this thesis

- Chapter 4 introduces the Metal-to-Insulator transition in  $V_2O_3$  and presents a detailed study of the electronic structure throughout the transition
- Chapter 5 approaches the Quantum phase transitions in  $URu_2Si_2$  and shows how they can be driven by Silicon-to-Phosphorous substitution
- Chapter 6 finishes by summarising the perspectives for future research these results lead to
- Last, but not least, an Annex provides a brief description of a tool I developed to be able to understand how the ARPES measurements slice the complex 3D reciprocal space of  $V_2O_3$  and, by generalization, of any crystalline system.

## 2 - A Short Tale of Band Theory and Phase Transitions

### 2.1. Classical Band Theory

Even though the aim of this thesis is to explore strongly correlated systems, in which classical band theory is insufficient to describe the physics, several key concepts from it are required. This section will be limited to the relevant parts, as there are several excellent textbooks on the subject that give a thorough introduction [2-4]

#### 2.1.1. From Bands in Independent-Electron Systems to Electronic States in Strongly Correlated Systems

##### The Tight Binding Approach

At the dawn of time (but well after atoms were formed and fused into complex elements, so for the universe, it wasn't really dawn, but rather the brunchtime around which lazy PhD students arrive at the lab, to stay in the metaphor), before crystals appeared, there were atoms, with electrons in the eigenstates of the spherical Coulomb potential of the nuclei. With the formation of crystals, the core concept of solid state physics came to be: the periodic potential of the crystal lattice necessitates, as shown by Bloch's theorem, the combination of the atomic orbitals into eigenstates with the same periodicity, the bands. In the tight binding model, these are described by virtually bound states in between which the electrons can tunnel. However, the eigenstates are still completely delocalised throughout the crystal. A single one such band is described by the Hamiltonian

$$H_t = -t \sum_{i,j,\sigma} \left( c_{i,\sigma}^\dagger c_{j,\sigma} + \text{H.c.} \right) - \mu N \quad (2.1)$$

where  $c_{i,\sigma}^\dagger$  is the creation operator. Note that, as is common in second quantization, H.c. represents the hermitian conjugate of a term, as required by symmetry of the Hamiltonian. The hopping term  $t$  depends on the overlap of the atomic orbitals that form the band, and determines the bandwidth. In turn, for strongly bound core levels,  $t$  becomes small, and accordingly narrow bandwidth results in a spectrum that is discrete in binding energy. Lastly, the term  $\mu N$  describes the chemical potential.

##### The Orbital Character of the Bands

It is worth noting that the symmetries of the constituent orbitals are carried over into the bands, which is often described as its *character*. For example, in transition metal oxides, the conduction band is often formed by  $d$ -orbitals of the transition metals and neighbouring Oxygen  $2p$ -orbitals. It is of particular interest

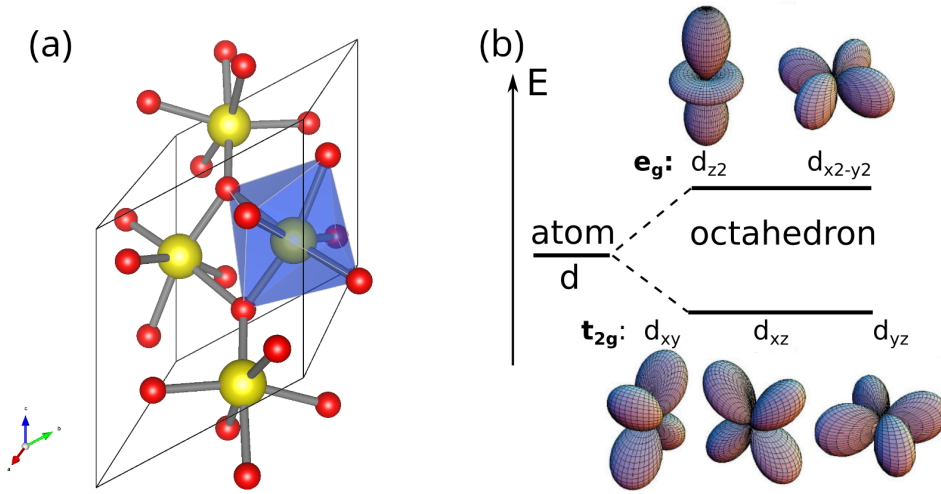


Figure 2.1: The crystal field of octahedral ligands in some transition metal oxides lifts the degeneracy of the  $d$  orbitals. (a) Unit cell of  $V_2O_3$ . Each Vanadium atom (yellow) is surrounded by an octahedron (blue) of Oxygen atoms (red). (b) The crystal field of octahedral ligands in some transition metal oxides like  $V_2O_3$  lifts the degeneracy of the  $d$  orbitals and splits them into a doublet of  $d$ -orbitals pointing at the ligands forming the higher energy  $e_g$  states, and the lower energy  $t_g$  triplet pointing in between. Adapted from [5].

for this thesis that in compounds with octahedral ligands around the transition metal atoms, like  $V_2O_3$ , the degeneracy of the  $d$  orbitals is lifted by the stronger negative charge of the Oxygen. This splits the  $d$ -orbitals into a doublet of  $d$ -orbitals pointing at the ligands forming the higher energy  $e_g$  states, and the lower energy  $t_g$  triplet pointing in between. This symmetry is shown in Fig. 2.1.

### 2.1.2. Reciprocal Space and Band Structure

#### Quasiparticles

In basic solid state physics, it is established that the collective states of delocalised electrons have an energy  $E$  that disperses with the crystal momentum wavevector  $\vec{k}$ , which in turn is defined modulo the reciprocal lattice vectors  $\vec{G}$ . The behaviour of such collective states can be described similarly to that of electron-like *quasiparticles* in vacuum. In particular, their response to external forces is governed by their effective mass

$$m_{eff} = \hbar^2 \left( \frac{d^2 E}{d^2 k} \right)^{-1} \quad (2.2)$$

similar to the inertial mass of real particles. The effective mass is normally anisotropic, and it can take negative values. In this case, the behaviour of the collective of electrons is described more simply by considering a single electron

vacancy, the hole quasiparticle, that carries a positive charge and has a positive  $m_{eff}$ .

### Metals and Insulators

In the approach of classical band theory, that neglects the interactions between electrons, the Eigenstates of the Hamiltonian are populated at  $T = 0$  K by the available electrons in the system, from the bottom up. If the highest occupied state is filled partially, electrons can move to an adjacent virtually bound site into an unoccupied state, and are mobile, making the system metallic. On the other hand, if the highest occupied state is filled completely, there are no free states available to move, and the system is insulating. In metals, the energy up to which states are occupied at 0 K is called the *Fermi energy*, the wavevectors of the dispersing states where they cross the Fermi energy are the *Fermi momenta* and the 2-dimensional manifold of the Fermi momenta in a 3-dimensional reciprocal space is called the *Fermi surface*.

The demarcation between metals and insulators is a binary classification defined at 0 K (a semiconductor is an insulator whose bandgap is small compared to possible excitations at room temperature), and should not change with temperature. The very existence of a temperature-driven metal-to-insulator transition as it will be presented in chapter 4 thus shows the assumptions of classical band theory to be invalid for the system.

## 2.2. Strong Correlations

The assumption that causes these limitations of classical band theory is that it completely neglects electron-electron interactions. For the electron correlations to be strong, the local electron density must be high, corresponding to a narrow distribution of the wavefunction in space. Orbitals with higher angular momentum quantum number, namely  $d$  and  $f$  shells, are highly directional and thus fulfill this condition better. Consequently, strong correlations are found in compounds with transition metals (partially filled  $d$ -orbitals) or rare earth elements (partially filled  $f$ -orbitals). Strongly correlated systems is a collective term for all materials where these interactions give rise to interesting behaviour and new physics, like mixed-valence systems, high- $T_C$  superconductivity in cuprates [6], Kondo insulators like  $\text{SmB}_6$  [7], and the metal-to-insulator transitions like in  $\text{V}_2\text{O}_3$ .

### 2.2.1. Hybridization

An important example for the understanding of the interactions between electrons is the Kondo effect. Experimentally, this is an unexpected rise by several orders of magnitude in the resistivity of gold wires, which Jun Kondo explained in 1964 with the scattering of conduction electrons off magnetic impurities [8]. Such localised magnetic moments, however, need not come from impurities, but can actually be a part of the crystal lattice itself. This periodic Kondo effect is

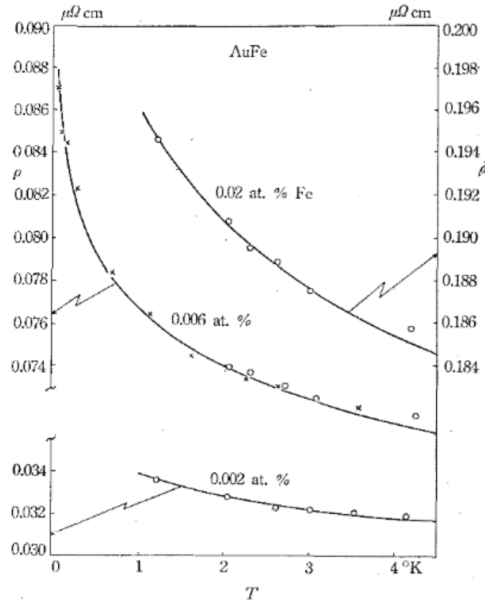


Figure 2.2: Kondo's measurements for the resistivity (dots) of iron-doped gold wires and predicted logarithmic behaviour from his publication in 1964 [8]. The rise in resistivity at low temperatures is caused by conduction electrons interacting with the local magnetic moments of iron atoms.

particularly prevalent in rare earth compounds with partially filled f-orbitals.

If the eigenstates of the non-interacting Hamiltonian are a delocalised conduction band dispersing with  $E = \frac{\hbar^2}{2m_{eff}}k^2$ , and a localized state at energy  $E_f$ , the interactions can be treated as a perturbation. This causes a hybridization of the eigenstates close to the original crossing point, where a narrow gap in the range of 10 meV opens, as has been observed in  $\text{SmB}_6$ , the first experimentally confirmed Kondo insulator [7] - i.e., a material in which the gap due to the hybridization between the dispersing and localized states opens right at the Fermi level. Phenomenologically, the signature of these strong correlations is a notable increase in the effective mass of the quasiparticle bands, establishing the term *heavy Fermions*. The formation of the heavy bands is illustrated in Fig. 2.3.

### 2.2.2. The Mott-transition

The opening of a hybridisation gap by scattering is far from the only effect that can result of strong correlations. When considering the interaction between electrons, the dominant force should be their Coulomb repulsion, and as this repulsion becomes stronger, it progressively inhibits the movement of electrons throughout the lattice. Therefore, as interactions increase, a previously metallic compound undergoes a transition to an insulator, a process described by N. F. Mott. [10]

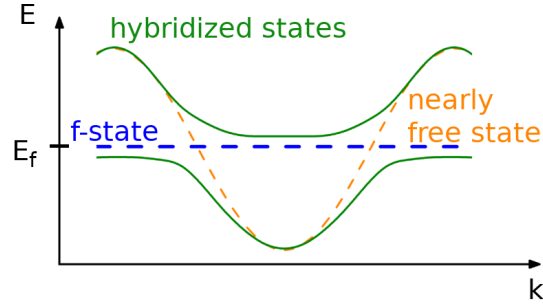


Figure 2.3: The hybridization of a localized f-state (blue) and a nearly free state (orange) in k-space. The perturbation is strongest in the area of avoided crossing, where a narrow band-gap in the range of 10 meV opens between the hybridized states (green). Taken from [9].

Mott's approach takes a single electron orbital at each lattice site, filled with one electron. This can be represented by the Hubbard model

$$H_H = H_t + H_U - \mu N \quad (2.3)$$

with the orbital overlap component from the tight binding model

$$H_t = -t \sum_{i,j,\sigma} \left( c_{i,\sigma}^\dagger c_{j,\sigma} + \text{H.c.} \right) \quad (2.4)$$

and the on-site interaction

$$H_U = U \sum_i \left( n_{i,\uparrow} - \frac{1}{2} \right) \left( n_{i,\downarrow} - \frac{1}{2} \right) \quad (2.5)$$

where  $n_{i,\sigma}$  is the number operator for a spin  $\sigma$ . Without repulsion ( $U = 0$ ), this is the simple tight binding model, but as  $\frac{U}{t}$  becomes important, the previously unique band splits into two components: one at lower energy, corresponding to exactly one electron at a lattice site, and one at higher energy with 2 electrons on that site. In between these two *Mott-Hubbard bands*, a gap opens, rendering the system insulating. This behaviour is shown schematically in Fig. 2.4.

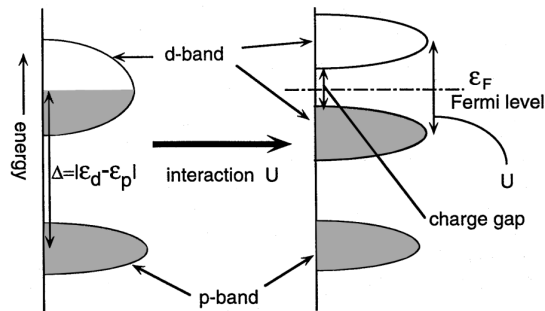


Figure 2.4: The Mott-metal-to-insulator transition. A partially filled d-band in the metallic phase (left) allows for conduction, but as repulsion increases, so does the energetic cost of electron proximity, and the band splits into 2 subbands (right): A fully filled lower Mott-band with one electron per lattice site, and a completely empty upper Mott-band representing a site with 2 electrons. Since electrons can only move into the unoccupied upper Mott-band, they become immobile without excitation. Figure taken from [11].

## 2.3. Phase Transitions

Ludwig Boltzmann, who spent much of his life studying statistical mechanics, died in 1906, by his own hand. Paul Ehrenfest, carrying on the work, died similarly in 1933. Now it is our turn to study statistical mechanics. Perhaps it will be wise to approach the subject cautiously.

---

David L. Goodstein, *States of Matter*

### 2.3.1. Of Phases and Ordering

On general grounds, phases are regions in the thermodynamic parameter space of a system, with uniform physical properties. Known examples include the states of matter - solid, liquid, gas and plasma - the presence of magnetism, or - of particular interest for this work - the occurrence of exotic quasiparticle states. They are often visualized in *phase diagrams*, where the coordinates represent the parameters, and the phases and their borders are shown. For example, typical phase diagram for solid, liquid and gas phases in matter is shown in Fig. 2.5

A phase transition occurs when the parameters of the system are changed externally and it crosses one of the borders in the phase diagram. It is worth noting that most phase transitions imply the breaking of a symmetry of the system, introducing a long-range order. For example, the onset of ferromagnetism when lowering the temperature below the Curie-temperature of a system breaks the rotational symmetry, and when water crystallizes to ice, translational symmetry is

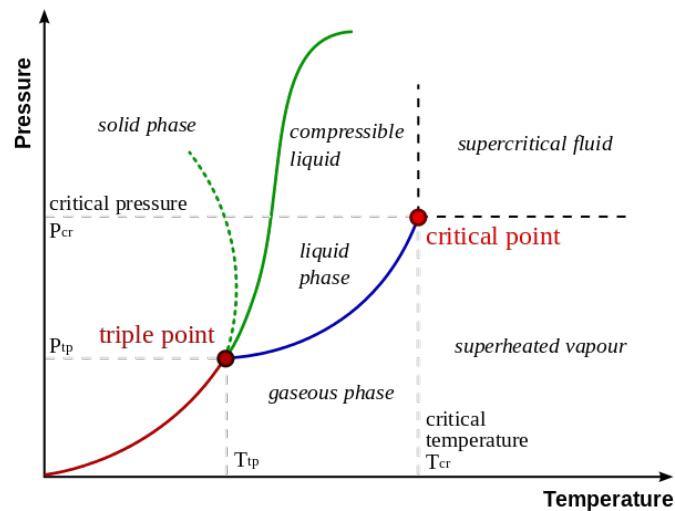


Figure 2.5: Typical phase diagram for transitions between solid, liquid and gas phases in matter. The dashed line in green describes the special anomaly of water. Taken from [12].

broken by the lattice. On the other hand, when a gas becomes liquid or is ionized to a plasma, no fundamental symmetry is broken or introduced. For a transition that introduces order, one can identify an *order parameter*, which quantifies the long range order and must necessarily be 0 in the unordered phase, while finite in the ordered one.<sup>1</sup> Identifying an order parameter is useful to define the exact point in the parameter space where the transition occurs, and one can define the phases themselves via the values of all relevant order parameters. Abstractly, this implies that the phases are the space between phase transitions, rather than the transitions being the intersection of phases.

### 2.3.2. 1st and 2nd Order Transitions

So far, we have only considered transitions with an abrupt change in the physical properties of the system - often making the order parameter itself discontinuous. These are known as *first order* phase transitions. In such a case, the long range ordering at the transition implies a loss of entropy, and thus the emission of a latent heat. In reality, this requirement for latent heat defines how a sample behaves across the transition: At a finite transition temperature, thermal excitation can put some of the sample into the unordered state, while other parts are in the

<sup>1</sup>For phase transitions that do not introduce order, one can sometimes still find an order parameter that satisfies the zero-to-nonzero rule in order to apply parts of the formalism. Examples include the ionization rate for the plasma formation, or the difference in density for evaporation. However, since there is no long range order that can be quantified in these transitions, these are not **order** parameters in the true sense.

ordered state. These parts form spatially separate domains, and this phase coexistence across them broadens the transition in the phase diagram. When crossing the broadened transition into an ordered state, one can observe the nucleation of small ordered domains, that grow in size until the transition is complete and long range order is obtained. When going back into the unordered state, the inverse process happens, but due to the nature of the disordering, there is a hysteresis.

Phase transitions that happen continuously (which is fundamentally different from an abrupt change broadened by phase coexistence and domain formation) are of *second order*. More precisely, the quantity that defines whether the transition is of first or second order is the Free Energy  $F$ . The order of the transition is then defined as the lowest derivative of  $F$  with a discontinuity: Its *first* derivative  $F'$  is discontinuous across a first order transition, while for a second order transition, the  $F'$  is continuous and the *second* derivative  $F''$  is discontinuous. This second derivative is the response function  $\chi$  of the system, e.g. for temperature-driven transitions,  $\frac{d^2 F}{dT^2}$  is proportional to the specific heat, and  $\frac{dF}{dT}$  to the entropy. In the case of a first order transition, the finite jump in  $F'$  always causes the response function to diverge. In the case of a second order transition, a  $\lambda$ -shaped divergence can still occur, with  $F'$  looking like an infinitely steep sigmoid function in the vicinity of the critical point.<sup>2</sup> These divergences of the response function are characteristic hallmarks of phase transitions, and as we will see in 5, the hidden order transition was first discovered because of such a specific heat divergence.

### 2.3.3. Critical Points

For first order transitions, the discontinuity in entropy  $\Delta S$  is not fixed throughout the phase diagram, but can change for different parameters. Consequently, at a point where it closes to  $\Delta S = 0$ , it changes the nature of the transition from first order to second. Such a point is called a *critical point*, with a well known example given by the liquid-gas mixtures, that above a critical temperature and pressure become continuous - there is no more abrupt change in density. A more detailed treatment of Landau theory, which describes the physics of second order phase transition and its effects in the region around a critical point, would exceed the scope of this thesis.

### 2.3.4. Crystal Growth Phases

Up to here, we have only mentioned system parameters are controllable while measuring the physical properties of a sample, but the physics of phases and transitions is not limited to that.

At Hokkaido University in the 1930s, Japanese physicist Ukichiro Nakaya extensively studied the formation of snow flakes, and managed to grow the first artificial snow crystals. Water crystalizes in a hexagonal structure, but he found

---

<sup>2</sup>Landau theory for 2nd order phase transitions actually shows that the divergence of the response function depends on the critical exponent.

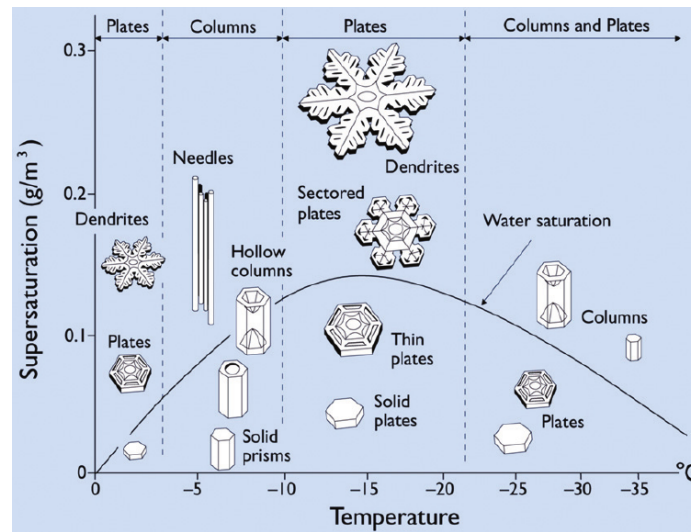


Figure 2.6: The crystal diagram of snow flakes as found by Nakaya [13]. Figure taken from [14]

that for minimizing surface energy during the growth process, it became energetically favourable for water molecules to settle either along the c-axis (perpendicular to the hexagonal plane) from another molecule, or within that plane, depending on the ambient temperature and humidity. The first would result in conically shaped crystals, while the latter would give flat flakes, and the resulting crystals' shape would be permanently determined by the parameters during their growth.

The crystal phase can therefore not be changed by the thermodynamic parameters at a later point in time, and crystal phase diagrams can include a combination of growth parameters like doping or deposition rate, and measurement parameters like temperature or applied magnetic fields. Of particular interest for this work is the observation that in some cases, a doping during growth can mimic the effects of hydrostatic pressure on a crystal. By substituting smaller atoms with equal oxidation (they are found in the same group of the periodic table as the atoms they are replacing) on some lattice sites, one can create negative chemical pressure, while positive pressure is obtained by larger dopants.

### 2.3.5. Quantum Criticality

The ongoing interest in quantum effects, especially at low temperatures, confronts scientists with a new kind of phase transition: if changing a parameter in a system shifts its quantum mechanical ground state to one with different ordering, the transition will also happen at a temperature of absolute zero. In this case, instead of thermal fluctuations, that are impossible at 0 K, the transition is driven by quantum fluctuations. The Heisenberg uncertainty principle states that for two non-commuting operators,  $\hat{A}$  and  $\hat{B}$ , their expectation values  $a$  and  $b$  can not be

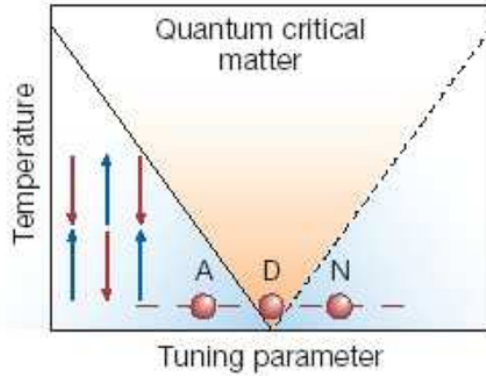


Figure 2.7: Schematic illustration of a quantum critical phase diagram with a transition from a normal (N) to an antiferromagnetic (A) region through the quantum critical point (D). For finite temperatures, the quantum critical region in orange expands in a V-shape. Figure adapted from [16].

completely determined at the same time.

$$\Delta a \Delta b = \frac{1}{2} \left| \langle [\hat{A}, \hat{B}] \rangle \right| \quad (2.6)$$

This uncertainty allows fluctuations of physical quantities even at 0 K, that can destroy order and in turn drive a continuous phase transition.

In the phase diagram of a quantum phase transition, as illustrated in Figure 2.7, the point where the two phases meet at absolute 0 is called the quantum critical point (QCP). In the vicinity of this point, the wavefunction of the system behaves according to the corresponding phase on large length scales. Below a certain scale, on the other hand, the effects of the quantum fluctuations cause the wavefunction to assume characteristic properties of the quantum critical point.[15] This scale diverges at the QCP, as the system is now in a complex superposition of the corresponding ground states of the neighbouring phases. It is this state for which the term *quantum critical matter* is often used.

From these considerations, one might assume that the notion of quantum criticality is purely of theoretical interest, as we can not reach 0 K in reality. However, it has been found that thermal effects do not immediately overshadow the quantum critical scale, but instead increase the scale in which the quantum critical behaviour of the wavefunction occurs. This means that the quantum critical phase actually extends to a V-shaped, finite area above absolute zero in the phase diagram. [15, 16] This is shown in Figure 2.7.

Quantum criticality has been found experimentally in a variety of metallic compounds [17–19] and specifically, heavy Fermion metals [20]. In these studies, it was found that in the quantum critical regime, physical properties can behave dramatically different from normal metals, like a diverging Sommerfeld coefficient (the

ratio  $C/T$  of the specific heat  $C$  and the temperature) with decreasing temperature and a resistivity that is linear instead of quadratic in temperature. [17] The collectivity of these phenomena is referred to as *non-Fermi-liquid behaviour*. [21]



## 3 - Photoelectron Spectroscopy 101

The energy- and momentum-resolved electronic structure of solids can be probed by Angle-resolved photoelectron spectroscopy (ARPES). Looked at from the outside, ARPES is a photon-in-electron-out technique. Thus, to master this method, we need to understand the photoelectric process that links the photon we send and the electron we measure. As a short guide to this powerful technique, this chapter will first concentrate on the photoelectric process, and further explain how this effect can be used as an elaborate experimental technique.

### 3.1. Photoelectron Spectroscopy

#### 3.1.1. The Photoelectric Effect

The photoelectric effect, in one sentence, is the excitation of an electron in a solid by an incoming photon, and its subsequent emission. After it was discovered by Heinrich Hertz [22] and Wilhelm Hallwachs [23], Albert Einstein managed to explain this effect in 1905 [24] and was awarded Nobel prize for it: An electron is emitted from a solid state body by absorbing a photon of energy  $\hbar\omega$ , as seen in Fig. 3.1. Energy conservation dictates the kinetic energy of the emitted photoelectron by

$$E_{kin} = \hbar\omega - \Phi - |E_B| \quad (3.1)$$

where  $\Phi$  denotes the work function of the sample and  $E_B$  is the binding energy of the initial state within the sample.  $\Phi$  as the difference between the vacuum level and the Fermi energy depends solely on the material the electron is emitted from. However, in experimental photoelectron spectroscopy, we normally measure the difference between the work functions of the sample and the detector.  $E_B$ , on the other hand, is a core property of the initial electronic state, and as we have seen in chapter 2.1, it can be a discrete spectrum in the case of core levels, or disperse continuously with crystal momentum in the case of itinerant states. These energy levels are illustrated in 3.1. The emitted electron can be detected, and a spectrum depending on the kinetic energy of the electrons can be recorded, and the initial binding energies can be calculated allowing to measure the density of occupied states in the sample. In the late 1950s, this was developed into an experimental technique by physicists around Kai Siegbahn, who received a Nobel price for it in 1981.

#### 3.1.2. Core Level Spectroscopy

If a photon with sufficiently high energy is used for the excitation, a strongly bound core state can be probed. The binding energy of these core states is affected

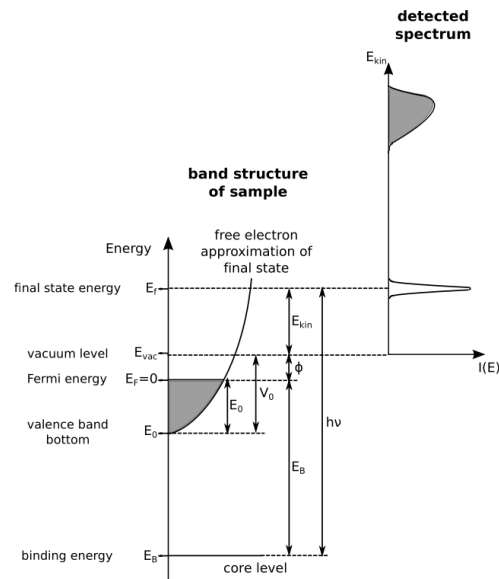


Figure 3.1: Energy levels involved in photoemission process. Electrons are excited to a final state at an energy  $E_f$  that is  $h\nu$  above their initial binding energy  $E_B$ . When leaving the sample, the electron needs to overcome a potential barrier of the inner potential  $V_0$ . Adapted from [25]

by the chemical surroundings of the atom. Thus, this photoelectric spectrum contains detailed information about the chemical composition of a sample. which is why this technique is sometimes called *Electron Spectroscopy for Chemical Analysis* (ESCA). The nowadays more common name is X-Ray Photoelectron Spectroscopy (XPS) for the high energy photons involved.

In contrast to these core levels, the valence and conduction bands close to the Fermi level have their binding energy disperse with the crystal momentum, occupying a wide energy range. In 3.2, we will see how this dispersion can be measured.

### 3.1.3. Three-Step Model

A common model to describe the photoelectric effect, the *three-step model*, treats this physical process as split into three consecutive and independent steps:

1. Photon absorption and subsequent optical excitation of an electron between bulk Bloch states
2. The photoelectron travelling to the surface
3. It leaves the sample and becomes a free electron

We the describe the physics of each step in detail.

### Photon Absorption

The probability of a photoelectron excited in the first step is given by the product of the initial state being occupied (according to the Fermi-Dirac distribution  $f(E_i)$ ) and the transition probability  $w_{f,i}$ . The photoelectron intensity  $I$  is thus related to the incident photon intensity  $I_0$

$$I = I_0 \sum_{f,i} f(E_i) w_{f,i} \quad (3.2)$$

The interaction Hamiltonian of an electron with momentum  $\mathbf{p}$  in the electromagnetic field with scalar potential  $\phi$  and vector potential  $\mathbf{A}$ , given by our photon, is

$$\mathbf{H}_{int} = -\frac{e}{2mc} (\mathbf{A} \cdot \mathbf{p} + \mathbf{p} \cdot \mathbf{A}) - e\phi + \frac{e^2}{2mc^2} \mathbf{A}^2 \quad (3.3)$$

We choose the gauge so that the  $\phi$  vanishes. Since in UV photoelectron spectroscopy the wavelength of the light is much larger ( $> 10^2 \text{ \AA}$ ) than the interatomic distances (several  $\text{\AA}$ ), the vector potential can be assumed to be constant in space ( $\nabla A = 0$ ) and the commutator  $[\mathbf{A}, \mathbf{p}] = i\hbar (\nabla \mathbf{A})$  thus be neglected. This is called the *dipole approximation*.

Furthermore, for the light intensities usually employed in photoemission experiments, the fields are weak, and the quadratic term in  $\mathbf{A}$  can be neglected as well (*linear approximation*). The interaction Hamiltonian is simplified to

$$\mathbf{H}_{int} = -\frac{e}{mc} \mathbf{A} \cdot \mathbf{p} \quad (3.4)$$

From perturbation theory, the absorption of the photon in the first step can be described by Fermi's golden rule, where the absorption probability is proportional to

$$w_{f,i} = \frac{2\pi}{\hbar} |\langle \Psi_f | \mathbf{H}_{int} | \Psi_i \rangle|^2 \delta(E_f - E_i - \hbar\omega) \quad (3.5)$$

The squared scalar product expression is referred to as the *matrix element*. As we will see later, it includes dipole selection rules.

While the transition in reality occurs from a N-electron correlated state to a (N-1)-electron correlated state and the nearly-free one-electron state, one can simplify this transition with some assumptions. As a simple model, one can assume the initial wavefunction as a tensor product of the individual wavefunctions

$$|\Psi_i(N)\rangle = |\Phi_i\rangle |\Psi_i(N-1)\rangle \quad (3.6)$$

This wavefunction needs to be antisymmetrised for Fermion statistics. The (N-1)-particle state  $|\Psi_i(N-1)\rangle$  is the remainder of the N-particle state  $|\Psi_i(N)\rangle$  after factorising out the single-electron wavefunction, and is an eigenstate of the (N-1)-particle Hamiltonian.

In order to write the final state, it is a helpful approximation to assume the photoemission process to be a instantaneous removal of the photoelectron, unaffected by a possible relaxation of the (N-1)-particle state. This is called the *sudden approximation* (giving names to our approximations makes it easier to discuss in cases where they reach their limit). The final state can then be factorized into the nearly free state and an excited remaining (N-1)-particle wavefunction.

$$|\Psi_f(N)\rangle = |\Phi_f\rangle |\Psi_{f,m}(N-1)\rangle \quad (3.7)$$

The index  $m$  iterates through the possible (N-1)-particle excited states with energy  $E_m(N-1)$ . To get a more intuitive idea of its meaning, if one were to omit the interchangeability of the particles (which is a grave sin in strongly correlated physics),  $m$  iterates over which of the N identical electrons has been removed. For the probability of the photoemission, it is now necessary to sum over these excited states

$$w_{f,i} = \frac{2\pi}{\hbar} |\langle \Phi_f | \mathbf{H}_{int} | \Phi_i \rangle|^2 \sum_m |c_m|^2 \delta(E_{kin} + E_m(N-1) - E_i - \hbar\omega) \quad (3.8)$$

where  $E_{kin}$  is the kinetic energy of the photoelectron and  $c_m$  is the overlap integral from the (N-1)-electron remaining wavefunctions.

$$c_m = \langle \Psi_m(N-1) | \Psi_i(N-1) \rangle \quad (3.9)$$

The sum over the excited states in equation (3.8) is called the **one electron removal spectral function**  $A$ .

$$A = \sum_m |c_m|^2 \delta(E_{kin} + E_m(N-1) - E_i - \hbar\omega) \quad (3.10)$$

For each excitation energy  $E_m(N-1)$ , there is a kinetic energy for which  $A$  becomes non-zero. This implies the occurrence of sets of peaks in the photoemission spectrum, with a main peak for the remaining wave function in the ground state and satellites for its excited states. The overlap integral in the spectral function contains the information about the electron correlations: if the system is non-correlated (independent electrons), the coefficient  $c_m$  will be nonzero only for  $m=i$ , producing a single Dirac peak in the spectral function at the energy of the initial state, while for a correlated-electron system, the excited states are not anymore eigenstates of the (N-1)-particle Hamiltonian, and the overlap integral becomes nonzero for various values of  $m$ , producing a broadened/shifted peak in the spectral function.

In the theoretical description of many-body systems, the spectral function is the imaginary part of the one-particle Green's function [26]. When treating the

particle interactions with the environment perturbatively, they can be introduced to the Green's function via the *self-energy*

$$\Sigma(\mathbf{k}, E) = \Sigma'(\mathbf{k}, E) + i\Gamma(\mathbf{k}, E) \quad (3.11)$$

The real component of the self-energy quantifies how the quasiparticle energy is renormalized due to interactions with its environment, and its imaginary component describes the inverse lifetime of the quasiparticle.

The spectral function is then

$$A(\mathbf{k}, E) = \frac{1}{\pi} \frac{\Gamma(\mathbf{k}, E)}{[E - E_B(\mathbf{k}) - \Sigma'(\mathbf{k}, E)]^2 + [\Gamma(\mathbf{k}, E)]^2} \quad (3.12)$$

For small self-energies, this gives a Lorentzian peak centred around the renormalised energy with a width of  $\Gamma$ . In other words, the quasiparticle lifetime is encoded in the width of the photoemission peaks.

### Travelling to the Sample Surface

In the second step, we assume the photo-excited electron being in a Bloch state of the unoccupied part of the bulk band structure and propagating to the sample surface. For usable spectroscopic information about the initial state, the electron must not undergo inelastic scattering. The inelastic mean free path  $\lambda$  is typically in the order of 1 nm to 10 nm, and strongly depending on the material, kinetic energy, sample purity and many other parameters. A rough, material-independent estimation is given by the empirical *universal curve* [27], a function of the electron's kinetic energy:

$$\lambda = \frac{143 \text{ nm}}{E_{kin}^2 / 1 \text{ eV}^2} + 0.054 \text{ nm eV}^{-0.5} * \sqrt{E_{kin}} \quad (3.13)$$

Note that  $\lambda$  is typically significantly shorter than the photon penetration depth. That is why the probing depth of photoelectron spectroscopy is determined by the inelastic mean free path and is only a few tens of nanometres thick. It is thus considered a surface sensitive technique. However, the estimation from the universal curve already shows one thing: the probing depth actually depends on the kinetic energy of the electrons. This can be used in core-level spectroscopy to distinguish surface phenomena - when measuring spectra with different excitation energies, their relative intensity changes.

### Leaving the Sample

When the electron leaves the sample in the third step, the work function is deducted from the kinetic energy. This can be regarded in terms of a mirror charge, that is created when the electron is removed from the sample, and the work function is the required energy to separate the electron from it. The momentum loss linked to the kinetic energy used for overcoming the work function is deducted from the component perpendicular to the sample surface, and the momentum in

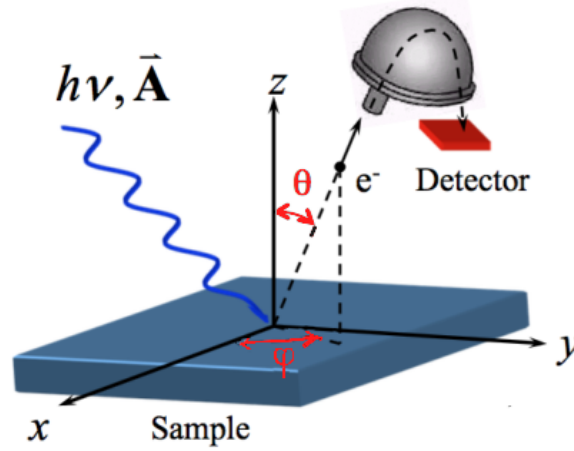


Figure 3.2: Schematic illustration of angle resolved photoelectron spectroscopy with the involved angles in the sample's system of reference.

the direction parallel to the surface remains unchanged. Such a conservation of momentum is indeed required by translational symmetry along the sample surface.

### Beyond the Three-Step Model

It is worth noting that the three step model is a powerful and extremely useful simplification. A more rigorous treatment is provided by the one-step model, but the three-step model is already sufficient to understand most of the results of standard photoemission experiments.

## 3.2. Angle Resolution

In addition to resolving the binding energy of the electronic states, we want to measure their crystal momentum. As we will see now, with a few assumptions, this can be deduced from the emission angle of the electrons.

### 3.2.1. Conservation of Momentum

In angle resolved photoelectron spectroscopy (ARPES), the photoelectron intensity is not only measured as a function of kinetic energy, but also of the angle of emission. This allows deducing the momentum component of the emitted electron parallel to the sample surface by

$$p_{\parallel} = \hbar k_{\parallel} = \sqrt{2m_e E_{kin}} \sin(\theta_e) \quad (3.14)$$

where  $m_e$  is the free electron's mass and  $\theta_e$  the angle away from normal emission. (See Fig. 3.2).

Considering that neither the second nor third of the aforementioned three steps of the photoelectric process changes the momentum parallel to the sample surface,

this directly gives the surface-parallel component of the electron wavevector of the excitation *final* state. And since the momentum of photons in the UV and soft X-rays is negligible compared to the typical size of a Brillouin zone (hence compared to typical electron momenta), the momentum of the electron's excited final state is in excellent approximation equal to the wavevector of the initial state. This is called the *vertical transition* approximation. These approximations can be used to map the dispersion of initial electron states in reciprocal space.

If the initial wavevector component perpendicular to the surface is of interest, an additional effect needs to be taken into account: the confining potential of the solid needs to be overcome. This energy difference is called the *inner potential*  $V_0$  and is subtracted from the electron's kinetic energy (see Fig. 3.1). In order to calculate the corresponding change in wavevector, we need to assume a dispersion relation in the state immediately before leaving the sample. For the quadratic dispersion of a nearly-free electron, this gives

$$\hbar k_{\perp} = \sqrt{2m_e (E_{kin} \cos^2(\theta_e) + V_0)} \quad (3.15)$$

$V_0$  is a sample-dependent parameter and we will later see how it can be determined experimentally.

Now, we can make momentum conservation explicit in (3.8):

$$w_{f,i} = \frac{2\pi}{\hbar} |\langle \Phi_f | \mathbf{H}_{int} | \Phi_i \rangle|^2 \sum_m |c_m|^2 \delta(E_{kin} + E_m(N-1) - E_i - \hbar\omega) \cdot \delta(k_f - k_i - G) \delta(k_{\parallel} - k_{f\parallel} - G_{\parallel}) \quad (3.16)$$

Here, the first momentum-dependent  $\delta$ -function describes the conservation of momentum of the photo-excitation inside the solid, and the second one the conservation of momentum parallel to the sample surface upon leaving the solid. The  $G$  are reciprocal lattice vectors. The one-electron matrix element  $|M_{f,i}|^2 = |\langle \Phi_f | \mathbf{H}_{int} | \Phi_i \rangle|^2$  directly affects the photoemission intensity through the probability of photon absorption. It contains the *dipole selection rules* of the photoemission process. Recalling from Eq. (3.4) that  $\mathbf{H}_{int} \propto \mathbf{A} \cdot \mathbf{p}$ , we can further simplify this for nearly constant  $\mathbf{A}$  by using the commutation relation  $2\hbar\mathbf{p} = -i[\mathbf{r}, H_0]$  with the position operator  $\mathbf{r}$  and the Hamiltonian of the one-electron system  $H_0$  to

$$|M_{f,i}|^2 \propto |\langle \Phi_f | \epsilon \cdot \hat{\mathbf{r}} | \Phi_i \rangle|^2 \quad (3.17)$$

where  $\epsilon$  is the unit vector along the polarization direction of the vector potential  $\mathbf{A}$ .

Since the scalar product  $\langle \Phi_f | \epsilon \cdot \hat{\mathbf{r}} | \Phi_i \rangle$  is implicitly integrated over space, the matrix element is only nonzero for integrands that are even with respect to specific mirror planes defined by the orientation of the crystal lattice and the experiment geometry. In the case of the detector being in such a mirror plane, the final state

needs to be even with respect to that plane, as an odd function is necessarily zero in that plane. Accordingly, for such a symmetry, the product  $|\epsilon \cdot \hat{\mathbf{r}}|\Phi_i\rangle$  needs to be even, as well. The parity of  $\epsilon$  is determined by the light polarisation, and that of  $|\Phi_i\rangle$  by the orbital character of the band. The extinction of photoemission for specifically polarized light can therefore be used to determine the orbital character of a band.

### 3.3. ARPES in Practice

While previously, we took a detailed look at the photoemission process itself, an experimentalist might be at first interested in it as a simple photon-in-electron-out technique, and the parameters they can control - much like when they take a coffee in the breakroom, they are interested in a capsule-in-coffee out operation of that machine, instead of the intricacies of the brewing process.<sup>1</sup> We will thus take a look at the minimum technical requirements for an ARPES setup, and the control parameters.

#### 3.3.1. General Constraints to the Experiment

The most basic requirement to the setup is already the source of most experimental difficulties: For the electrons to move freely outside of the sample on its way to the detector, ultra high vacuum (UHV) conditions are required. Good experimental conditions are normally below  $10^{-9}$  mbar. In addition, since electrons are leaving the sample in the process, the sample needs to be grounded in order not to accumulate a positive charge. Therefore, PES cannot be used on completely insulating samples, which will be presented as one of the big obstacles to obtaining the results shown in chapter 4. Samples with conductance limited to the surface need grounding contacts on the same surface the PES is conducted on, and good grounding contacts are an important thing to consider for all samples.

The electrons leaving the sample unimpeded also implies that the sample surface is clean within the vacuum, so one can not simply put a random stone found in nature into a PES chamber.

If one wants to observe band dispersions, the electrons must not be emitted from crystals with varying orientations, but from a surface with a well defined lattice direction on - ideally - a single crystal. This requires single-crystal samples of a minimum size defined by the setup. When using a single-crystal, such a well-oriented and pure surface can be obtained by breaking the crystal at low temperature in the ultra-high vacuum. Some crystals can be easily cleaved along a single lattice plane, and in UHV conditions, there are almost no impurities that can accumulate on the surface. Alternatively, one can try experiments on single crystals

---

<sup>1</sup>Of course, a true experimentalist is also ALWAYS interested in the photoemission process. For instance, the effects of wavefunction symmetries, matrix elements, or correlations in the spectra can only be understood if one pays attention to the photoemission process.

or single-crystalline thin films that are difficult or impossible to cleave. While this can yield a polychristalline sample from different growth nucleation sites, these domains are all well oriented. If such a non-cleaving sample is transported *ex situ*, it needs to be cleaned within the vacuum before the experiment. Techniques for this used for samples presented later include annealing at high temperature to evaporate surface contamination (especially water, this can also sometimes 'heal' damaged surfaces) and sputtering with Argon ions to shoot impurities off the surface (while Argon is at least too noble to chemically bond to the sample surface).

Lastly, commonly available photoelectron analysers have a slit-shaped aperture that allows to measure electrons emitted within a wide angle-range along a unidirectional angle, while only measuring a single angle-datapoint in the perpendicular direction (see Fig. 3.4). The real angle of emission, on the other hand, is a solid angle. The second component of the emission angle has to come from the orientation of the sample surface with respect to the analyser aperture, and in order to control it as an experimental parameter, the sample needs to be rotated (or the analyser as a whole rotated around the sample, which *can* be done, but is an extreme effort when constructing a setup). The sample thus needs to be rotated and moved around in the vacuum with high precision.

A basic setup therefore consists of

1. a monochromatic light source
2. a UHV chamber
3. a grounded sampleholder within that chamber mounted on a manipulator with as many controllable degrees of freedom as possible
4. an analyser for the electrons

Further down, a more detailed look will be taken on the light sources and the analysers specifically.

### 3.3.2. Reciprocal Space in 3 Dimensions and Fermi Surface Measurements

To understand what parameters of the electronic structure can actually be probed by ARPES, we first look at the energies. Eq. 3.1 shows that by controlling the photon energy and selecting the kinetic energy at which we measure electrons, we can completely determine the binding energy to probe. Similarly, the angle of emission and kinetic energy combined give us all three components of the momentum vector outside of the sample - and as seen in 3.2 thereby the components of the crystal momentum in the initial state. This means that ARPES allows to probe a 4-dimensional parameter set of reciprocal space and binding energy, which is the reason why ARPES is so powerful in solid-state physics. When showing the results, this set, however, is often reduced to allow for an intuitive representation in an image. Commonly used ones include

1. *Dispersion maps*: The horizontal and vertical axis represent one component of the crystal momentum (while the 2 other components are fixed) and binding energy, respectively. Photoemission intensity is encoded in color.
2. *Constant energy maps*: The horizontal and vertical axis represent two components of the crystal momentum (while the third component and binding energy are fixed) and intensity is encoded in color. If the binding energy is fixed to the Fermi level, this is called a *Fermi map*.
3. *Momentum distribution curves (MDCs)*: Intensity is mapped on one axis as a function of a momentum-component while all other parameters are fixed.
4. *Energy distribution curves (EDCs)*: Like MDCs, intensity is mapped on one axis, but this time as a function of binding energy at a fixed momentum.

All these representations will be used throughout this thesis.

### 3.3.3. Light Sources

As seen before, for any kind of photoelectron spectroscopy it is necessary to at least *know* the photon energy, but better to *control* it. In the category of fixed wavelength sources, the required energy ranges make monochromated X-ray tubes ideal for core-level spectroscopy, while Helium and Xenon lamps with monochromators are usable for ARPES. In the case of ARPES, UV lasers can provide high-intensity sources as well, but these are often found at the very low end of usable photon energies. This is important because the difference between the photon energy and the binding energy plus work function needs to be positive!).

When the photon energy needs to be tuned freely, Synchrotrons are the dominating sources. Their high spectral brilliance and wide range of available energies make them almost ideal for the job, and all data presented here has been obtained using synchrotron light from SOLEIL in Saint-Aubin, France, KEK-PF in Tsukuba, Japan or BESSY II in Berlin, Germany.

### 3.3.4. Hemispherical Analysers

A typical photoelectron analyser consists of two concentric hemispheres with a radial electric field in between, by which electrons are diverted onto a circular trajectory (see Fig. 3.3). Those electrons with a specific kinetic energy called pass energy travel with the same mean radius as the two hemispheres, and can thus pass the analyser, while electrons with energies slightly larger (smaller) than the pass energy will pass the analyser at positions slightly larger (smaller) than its mean radius, hence allowing to map the distribution of kinetic energies in a narrow energy range around the pass energy to a radial distribution. Before the actual analyser, electron lenses map electrons moving at different angles to parallel movement with different displacements along the slit. Instead of simply tuning the radial field to have the desired kinetic energy pass the analyser, a deceleration voltage in the electron lens then transforms the desired kinetic energy to the pass energy. This

approach has the advantage of maintaining a constant energy resolution in the meV range (given only by the pass energy and the mean radius of the analyzer) for all the range of measured kinetic energies.

On the other end of the hemispheres, a microchannel plate (MCP) is used to multiply these electrons before a fluorescent screen on which events are detected by a CCD camera.

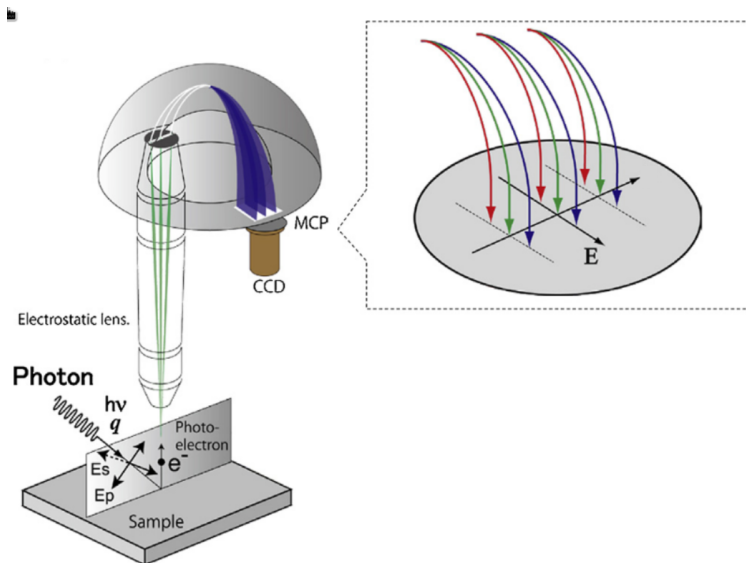


Figure 3.3: A hemispherical electron analyser as used in most PES and ARPES experiments. The radial electric field in the half-sphere separates the electrons by kinetic energy. The emission angle is mapped in the direction perpendicular. Adapted from [28]

ARPES analysers often come with the capability of measuring simultaneously along an angle  $\eta$  by having an aperture formed like a slit, while in the perpendicular direction, the angle is fixed. A more recent development in ARPES-analysers is able to deflect the electrons in the direction perpendicular to the aperture by an electric field, instead of rotating the sample surface. Such *deflector analysers* allow the angle of emission to be controlled completely independently of the sample position, while rotating the sample affects the surface position when that surface (more precisely, the focal point of the analyser, which must be on the surface) is off the axis of rotation. This is particularly advantageous for cleaved samples, which tend to have small usable surface sections positioned randomly when breaking the crystal, and no way to know the optimal position except trial-and-error.

### 3.3.5. Geometry and Systems of Reference

In order to determine the crystal momentum from the emission angles, the geometry of the experiment needs to be clear. Linear light polarization is denoted

horizontal if the electric field is parallel to the laboratory floor, and vertical if perpendicular. The orientation of the aperture slit of the analyser is similarly denoted. In the case of a horizontal slit and a perfectly vertical sample surface, the entire experiment happens in a clearly defined plane, and signal extinction by symmetry selection rules becomes maximised. A vertical slit on the other hand offers a less strictly defined symmetry, making the setup more versatile.

In the following, the angle of emission parallel to the aperture slit will be called  $\eta$ , and the one perpendicular will be called  $\theta$  (see Fig. 3.4). Be aware that this  $\theta$  is different from the unidirectional angle of emission  $\theta_e$  used in section 3.2. An experimentalist will know and control these angles in the laboratory's system of reference, but the true angle of emission is measured in the system of reference of the sample surface, with the conversion from these experimental control angles to true emission angles being done in post-experimental data analysis. For a full description of the conversion process, refer to [29, 30]

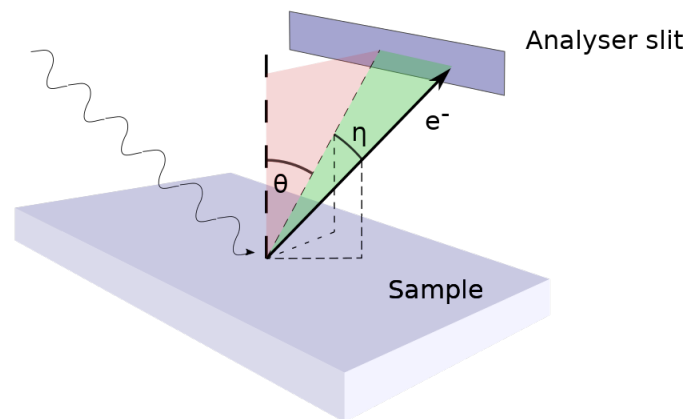


Figure 3.4: Illustration of the angles used to resolve the momenta in ARPES.

## 4 - The Metal-to-Insulator Transition of $V_2O_3$

Of the transition metal oxides, several Vanadium oxides show strong correlations:  $VO_2$ [31],  $V_2O_3$  and  $V_3O_5$ [32] have metal-to-insulator transitions and complex phase diagrams. They all share partially filled Vanadium 3d orbitals in various oxidation states, with a close valence band of Oxygen 2p character. In a naive picture, the partial filling of the 3d orbitals should result in a metallic system, raising the question of the microscopic origin of the experimentally observed metal-to-insulator transitions. Large parts of this chapter corresponds to material published recently in [33].

### 4.1. Previous Work

#### 4.1.1. Crystal Structure

In ambient conditions,  $V_2O_3$  crystallizes in a corundum structure with 4 Vanadium- and 6 Oxygen atoms per primitive unit cell. This primitive unit cell is rhombohedral with lattice vectors  $a = b = c = 5.467 \text{ \AA}$  and angles between these vectors of  $\alpha = \beta = \gamma = 53.74^\circ$  (see Fig. 4.1). The structure is also often represented by a non-primitive hexagonal cell with the volume of three primitive cells. When describing directions in this hexagonal (conventional) basis, four Miller indices  $(h_H, k_H, i_H = -h_H - k_H, l_H)$  are often used. A crystal vector given in conventional basis can be converted to the primitive (rhombohedral) basis  $(h_R, k_R, l_R)$  by

$$h_R = \frac{1}{3}(-k_H + i_H + l_H) \quad (4.1)$$

$$k_R = \frac{1}{3}(h_H - i_H + l_H) \quad (4.2)$$

$$l_R = \frac{1}{3}(-h_H + k_H + l_H) \quad (4.3)$$

The Brillouin zone that determines the physics in reciprocal space is - of course - the one corresponding to the primitive cell, which is why that basis will be used whenever discussing dispersions and results obtained by ARPES. On the other hand, our samples are epitaxially grown thin films, and the sample's surface orientation will be specified using hexagonal coordinates, as commonly done in the thin-film literature. The unit cells and Brillouin zone are shown in Fig. 4.1.

#### 4.1.2. Phase Diagram

Fig. 4.2 shows the phase diagram of  $V_2O_3$ . At room temperature the compound is paramagnetic, and when cooled down, it develops antiferromagnetic ordering accompanied by a structural change best described as a tilting of the

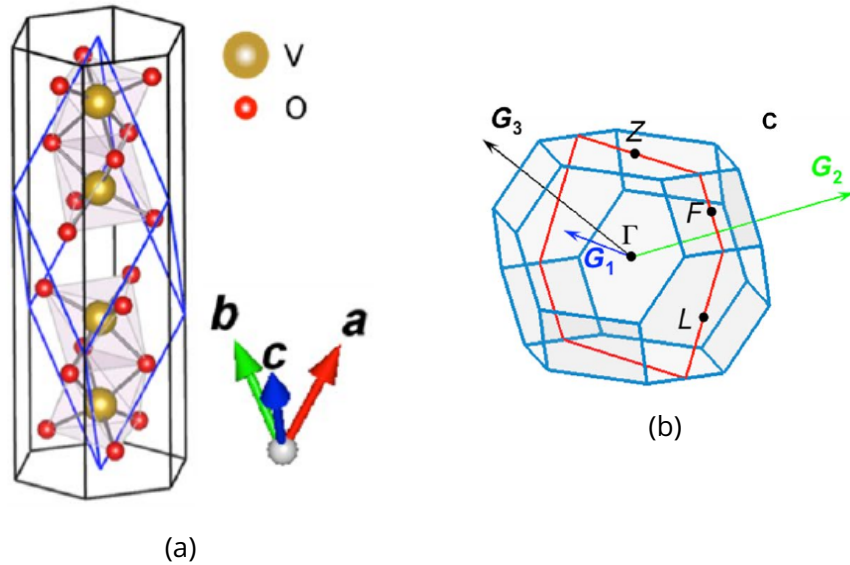


Figure 4.1: The crystal structure of  $V_2O_3$  in ambient conditions. (a): The primitive unit cell (blue) is rhombohedral with 4 Vanadium- and 6 Oxygen atoms. The conventional unit cell (black) is hexagonal with the volume of three primitive cells. (b): The first Brillouin zone with base vectors and high symmetry points. The plane marked in red is parallel to the  $(11\bar{2}0)$  surface of our samples and cutting through the  $\Gamma$ -point.

conventional cell along one of the hexagonal in-plane axes, as drawn inside the phase diagram in Fig. 4.2. The lattice symmetry changes accordingly from the Corundum-structure to a monoclinic one. This is accompanied by a sharp rise in resistivity of more than six orders of magnitude, forming a triple phase transition. This triple transition is of first order, and its transition temperature can be lowered by applying pressure to the system, up to its suppression at a quantum-critical point. At negative pressures, the high-temperature phase gets replaced by that of a Paramagnetic insulator with the same structure.

#### 4.1.3. Focus on the Triple-Transition

The phase diagram shows two phases available at ambient pressure (dashed line): The high-temperature paramagnetic metal phase with corundum structure (red) and the low-temperature antiferromagnetic insulator with monoclinic structure (blue). However, as obvious from the description of these phases, three distinct phenomenological transitions are observed: A magnetic one (Paramagnetic to Antiferromagnetic), a structural one (Corundum to Monoclinic, see Fig. 4.3 and 4.4) and an electronic one (Metal to Insulator, see Fig. 4.5). This begs the question whether there is a causal link between these three transitions. The structural transition represents a distortion in the lattice caused by a change in interactions

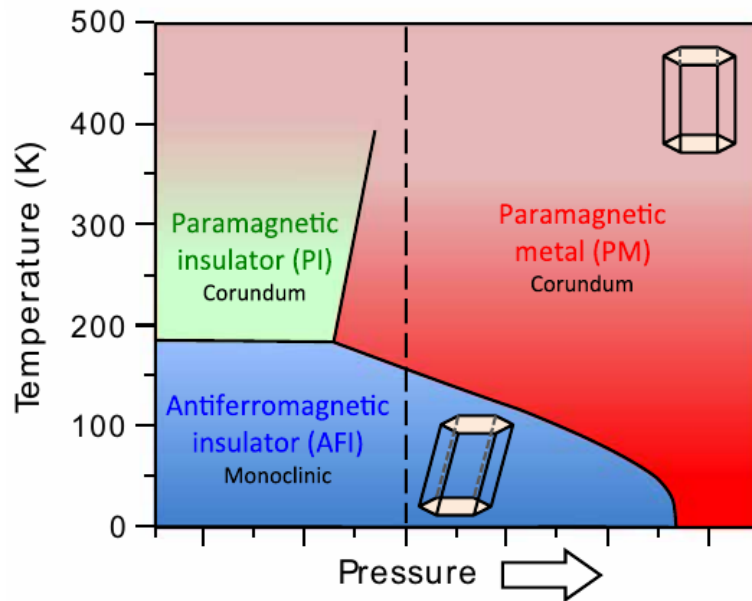


Figure 4.2: Phase diagram of  $V_2O_3$ . The horizontal axis marks hydrostatic pressure, the vertical axis the temperature. At ambient conditions, the system is a paramagnetic metal in a corundum structure (red area), and at low temperatures, it becomes an antiferromagnetic insulator with monoclinic structure (blue). At higher pressures, the transition temperature of these overlapping structural, magnetic and electronic transitions can be controlled by pressure until the low-temperature phase is suppressed at a quantum-critical point. At negative pressures, a third phase (green) of a paramagnetic insulator with Corundum structure occurs. It is not known if the electronic transition is completely separated from the structural and magnetic ones in this leftmost region of the phase diagram.

between the atoms. This could be either cause or effect of the onset of antiferromagnetism. Antiferromagnetism in turn causes a folding of the Brillouin zone by the ordering vector, and by Bloch's theorem, this folding can open a gap. In  $V_2O_3$ , it has been an open question whether such a folding-induced gap opens, making the onset of antiferromagnetism indirectly responsible for the Metal-to-Insulator transition. Note however that, as an order of magnitude, an AFM transition at  $T_N = 200$  K would have a BCS gap of the order of  $2k_B T_N = 33$  meV, which is 20 times smaller than the actual gap that opens in  $V_2O_3$ . Thus, AFM folding alone cannot explain the huge gap in a conventional picture.

The phase transition being of first order implies the formation of phase domains across the transition. Such domains, of micrometer to submicrometer size,

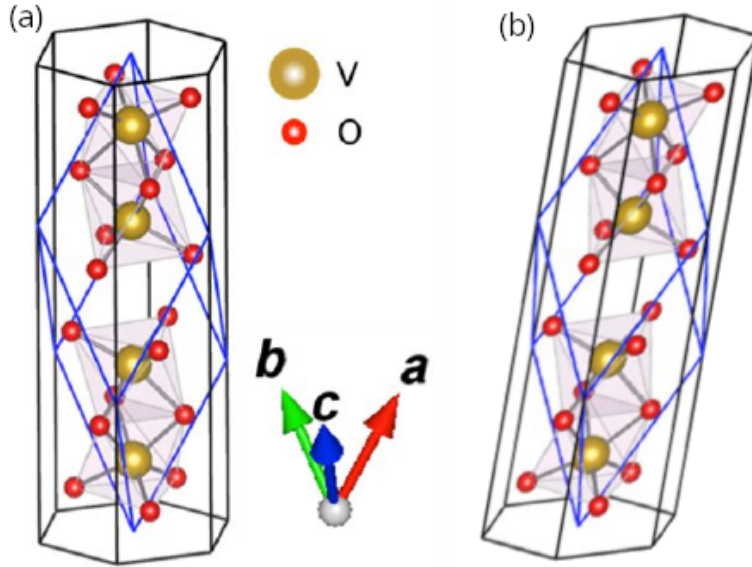


Figure 4.3: Crystal structure of  $V_2O_3$ . (a) Unit cell in the Corundum phase. The conventional hexagonal cell is shown in black, the primitive cell is drawn in blue. (b) Visualisation of the change to the monoclinic phase to the structure. The cell gets sheared along the antiferromagnetic ordering vector, within the plane of hexagons in (a).

have been directly imaged in real-space in  $VO_2$  and  $V_2O_3$  by near-field infrared microscopy [34, 37] (shown in Fig. 4.6), photoemission microscopy [38], and muon spin relaxation [39]. Previous photoemission experiments studied the momentum-integrated density of states of  $V_2O_3$ , identifying a quasiparticle (QP) peak at the Fermi level ( $E_F$ ) in the metallic phase [36] that disappears in the insulating state [40] and a broad feature at a binding energy  $E - E_F \approx -1.1$  eV [41, 42], assigned to the lower Mott-Hubbard (MH) band [36, 40] (see Fig. 4.8). The coexistence of the QP peak and the MH band is the hallmark of the correlated state, as predicted by dynamical mean-field theory some 30 years ago [43]. More recently, angle-resolved photoemission spectroscopy (ARPES) experiments in the metallic phase of  $V_2O_3$  single crystals [35] showed the existence of an electron-like QP band around the zone center ( $\Gamma$  point), dispersing down to about  $-400$  meV over Fermi momenta  $2k_F \approx 1 \text{ \AA}^{-1}$  along the  $\Gamma$ -Z direction, and suggested the presence of a nondispersive component of spectral weight in the metallic QP energy region (see Fig. 4.7).

The main physical issue at stake is at the core of the strong correlations problem, namely, how electrons transmute from itinerant, wave-like objects in the metallic phase to localized particles in the insulating one.

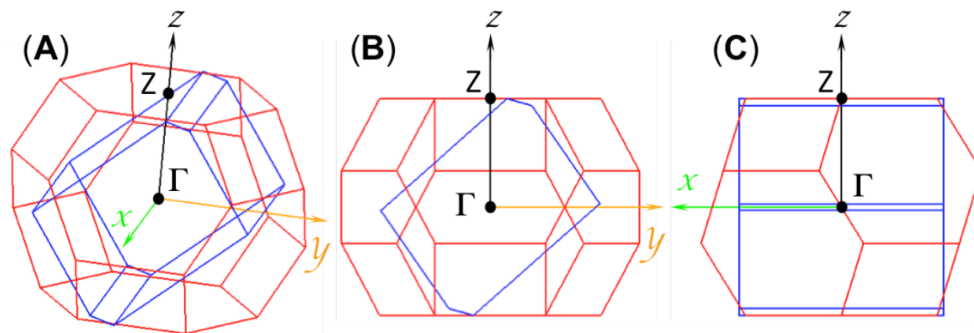


Figure 4.4: Rhombohedral and monoclinic Brillouin zones of  $V_2O_3$ . (A) Comparison between the rhombohedral (red) and monoclinic (blue) Brillouin zones of  $V_2O_3$ , corresponding respectively to the metallic and insulating phases. The xyz axes are also shown. (B, C) Same as (A) viewed from the x-side and y-side, respectively.

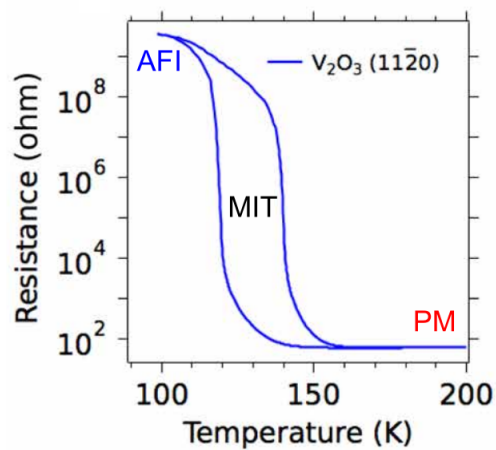


Figure 4.5: Resistance measured (2-point measurements) on a pristine  $V_2O_3/Al_2O_3$  ( $11\bar{2}0$ ) thin film. Across the MIT, the resistance changes by more than seven orders of magnitude, and the transition shows a clear hysteresis, characteristic of first-order phase transitions.

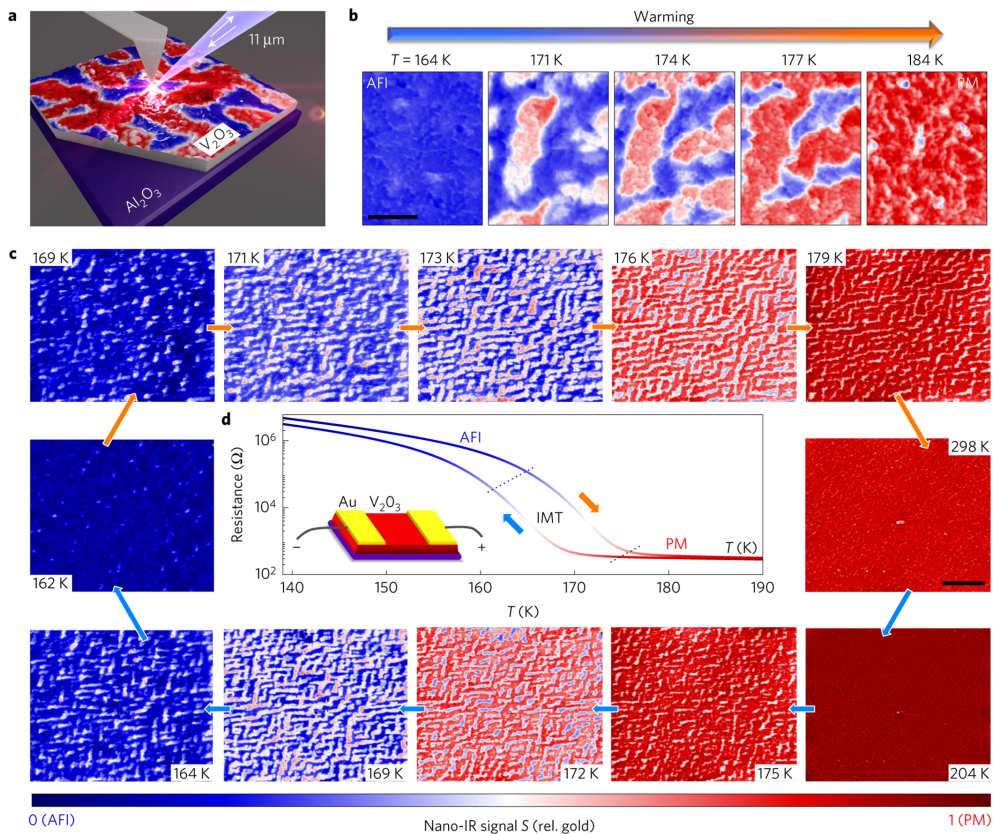


Figure 4.6: Near-field infrared microscopy measurements by McLeod *et al.* from 2017, showing the evolution of domains across the transition. A strong infrared signal (red domains) corresponds to high metallicity, and the hysteretic behaviour across the transition is visible. The scale bars in (b) corresponds to  $1 \mu\text{m}$  and that in (c) to  $5 \mu\text{m}$ . Figure taken from [34].

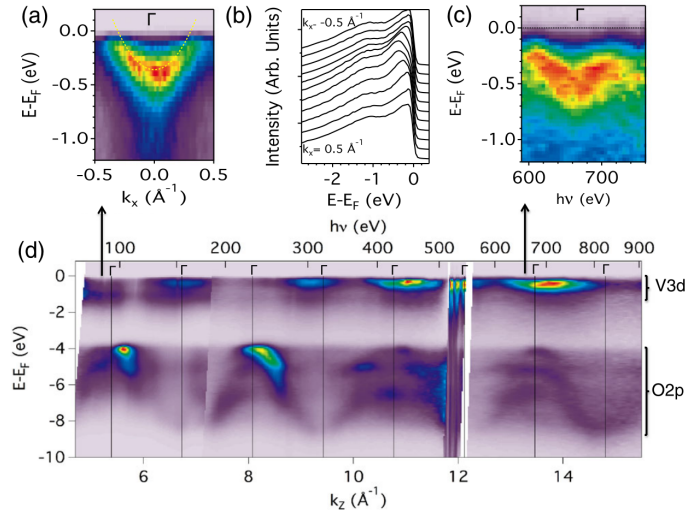


Figure 4.7: ARPES measurements by Lo Vecchio *et al.* from 2016. They identified an electron-like pocket around the  $\Gamma$ -point, as seen in the magnified energy-momentum maps in (a) and (c) as well as the EDC-stack corresponding to (a) shown in (b). The entire E-k-dispersion shown in (d) shows the dispersive quasiparticle band at the Fermi level, to which this pocket belongs, the lower Mott-Hubbard band around  $E_F - 1.5 \text{ eV}$ , and the O  $2p$  band from  $E_F - 4 \text{ eV}$  down. Figure taken from [35].

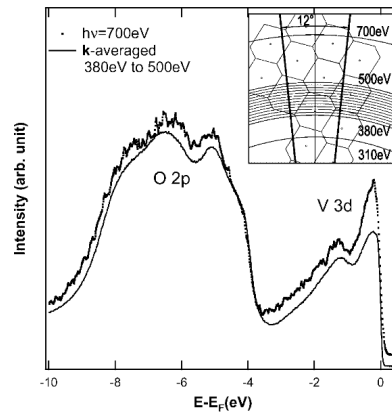


Figure 4.8: Photoelectron spectroscopy measurements on  $\text{V}_2\text{O}_3$  by Mo *et al.* from 2003. In the V  $3d$  region down close to  $E_F$ , the QP peak and the MH band are visible. The inset shows the cuts through the reciprocal lattice of  $\text{V}_2\text{O}_3$  for the photon energies they used for their work, with the dotted spectrum being measured at  $h\nu = 700 \text{ eV}$  while the continuous line is averaged over a range of  $380 \text{ eV}$  to  $500 \text{ eV}$ . Figure taken from [36].

## 4.2. Methods

However, several technical challenges have hindered the realization of momentum-dependent photoemission studies of the MIT in  $V_2O_3$ . For instance,  $V_2O_3$  crystals are extremely hard to cleave to expose a clean crystalline surface. Moreover, they become highly insulating below  $T_{MIT}$ , thus strongly charging upon electron emission, and break apart into pieces due to the structural transition. As will be shown now, these obstacles could be overcome by using thin films.

### 4.2.1. Thin Films

Recent developments in thin film growth techniques have enabled the synthesis of high-quality crystalline thin films of  $V_2O_3$  grown on  $Al_2O_3$  substrates.[\[44–46\]](#)

Because of the anchoring imposed by the latter, the crystal integrity of the films is not affected by stress due to the structural transition. This allowed us to measure the effects of the MIT on the momentum-resolved spectral function of the system.

The 100-nm-thick epitaxial  $V_2O_3$  thin films were deposited on  $(11\bar{2}0)$ - or  $(01\bar{1}2)$ -oriented  $Al_2O_3$  substrates by radio frequency magnetron sputtering, as described in [\[46\]](#). An approximately 8-mtorr ultrahigh purity Argon ( $>99.999\%$ ) and the growth temperature of  $700^\circ\text{C}$  were used during the sputtering process. The thin-film structural properties were measured using a Rigaku SmartLab x-ray diffraction system. Resistance versus temperature measurements were done using a TTPX Lakeshore cryogenic probe station equipped with a Keithley 6221 current source and a Keithley 2182A nanovoltmeter. This process was done at the Department of Physics and Center for Advanced Nanoscience, University of California San Diego, La Jolla, CA 92093, USA.

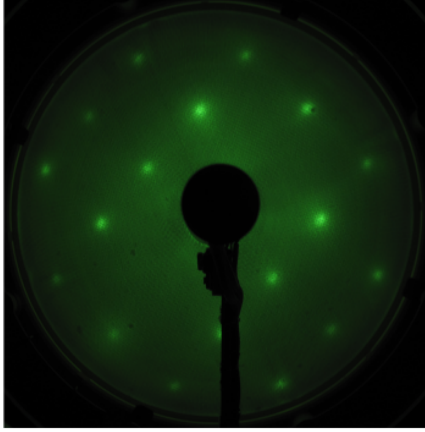
### 4.2.2. Annealing and Preparation

The surface of the  $V_2O_3$  films was cleaned *in situ* using protocols previously developed by our group for the investigation of two-dimensional (2D) electron gases in oxides [\[47–51\]](#). These include an annealing up to approximately  $500^\circ\text{C}$ , with the heating speed depending on the development of the *in situ* pressure and verification of the surface by low-energy electron diffraction (LEED). The cleaned surfaces showed well-defined LEED patterns shown in Fig. 4.9.

The cleaning process slightly lowers the onset temperature of the MIT and decreases the change in resistance between the insulating and metallic states, possibly due to the formation of Oxygen vacancies [\[47, 48, 52, 53\]](#). It is therefore reasonable to ask whether the UHV annealing modified the bulk composition or stoichiometry of the material, and this question will be focused on in 4.3.5.

Fig. 4.10 presents the X-ray diffraction (XRD) and electrical resistance characterizations of our  $V_2O_3 / Al_2O_3$   $(01\bar{1}2)$  and  $V_2O_3 / Al_2O_3$   $(11\bar{2}0)$  thin films before (blue or green curves) and after (red or yellow curves) the annealing in UHV required for ARPES experiments. Note that XRD is a bulk-sensitive mea-

(A)  $V_2O_3 / Al_2O_3 (01\bar{1}2)$



(B)  $V_2O_3 / Al_2O_3 (11\bar{2}0)$

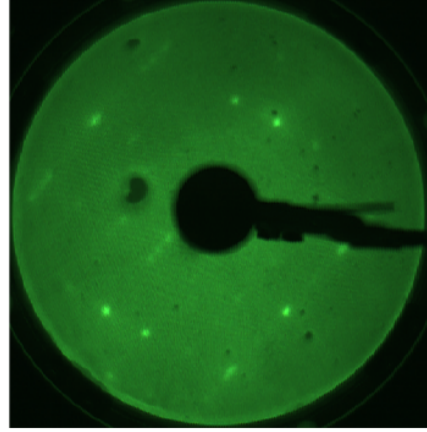


Figure 4.9: (A, B) LEED images of  $V_2O_3/Al_2O_3 (01\bar{1}2)$  and  $V_2O_3/Al_2O_3 (11\bar{2}0)$  films, respectively, obtained after *in-situ* annealing, right before ARPES measurements.

surement probing the entire thickness of the  $V_2O_3$  film, while temperature dependent electrical transport properties are very sensitive to changes in surface oxygen stoichiometry. Accordingly, no significant changes in crystal structure (main peaks of the XRD diagrams), hence in the bulk stoichiometry of the film, are observed. On the other hand, the onset of the resistive MIT on cooling is shifted down in temperature from about 160 K to approximately 140 K in the  $V_2O_3 / Al_2O_3 (01\bar{1}2)$  film, and from about 140 K to approximately 130 K in the  $V_2O_3 / Al_2O_3 (11\bar{2}0)$  film, while the change in resistance between the insulating and metallic phases is reduced by about three orders of magnitude in both films. We ascribe the observed changes after UHV annealing to the creation of oxygen vacancies, a phenomenon well known and reported in many other transition metal oxides [47, 49–51], including other correlated-electron vanadium oxides such as  $SrVO_3$  [48]. Indeed, in many of these oxides oxygen vacancies act as electron donors [47–51]. The important fact, however, is that the MIT and its hysteresis cycle are preserved, as indeed attested by the ARPES data, the latter being in very good agreement with the resistivity hysteresis cycle after UHV annealing. Such slight metallization of the sample is beneficial for the ARPES measurements, as it allows following the MIT without excessive charging down to the insulating state.

The previous is confirmed by infrared spectroscopy measurements, Fig. 4.11. These show that, in the metallic phase, the low-energy (far infrared) reflectivity, related to the concentration of free carriers in the sample, is slightly lower in a pristine  $V_2O_3 / Al_2O_3 (01\bar{1}2)$  sample compared to a sample of the same batch that was annealed then measured by ARPES. Note that, in the insulating phase, the reflectivity of both samples strongly decreases at energies below about 800 meV to

900 meV, showing thus that the optical gap in our thin films is similar to the one measured in single crystals, and is not appreciably affected by the UHV annealing. The only appreciable effect of UHV annealing, in phase with our characterizations from resistivity measurements, is that the temperature-dependent change in reflectivity at, e.g., 370 meV (inside the energy gap), is shifted down by about 15 K in the annealed sample.

In 4.3.5, the information about possible changes in the stoichiometry that can be obtained from photoelectron spectroscopy will be highlighted.

#### **4.2.3. Temperature Cycles at KEK and Cassiopee**

The first order nature of the phase transition makes measuring the temperature dependent electronic structure additionally challenging. To accurately capture the electronic hysteresis behavior across the MIT, the samples were loaded into the ARPES manipulator at 200 K. Once thermalized, we performed a slow stepwise cooling cycle, setting the parameters in the temperature controller so as to avoid overshooting the set-point temperature (hence avoiding spurious hysteresis cycles) and then letting the system thoroughly thermalize at that temperature for over 30 min before measuring. After reaching the lowest measurement temperature, we performed an analogous heating cycle, measuring at the same temperatures as during the cooling cycle.

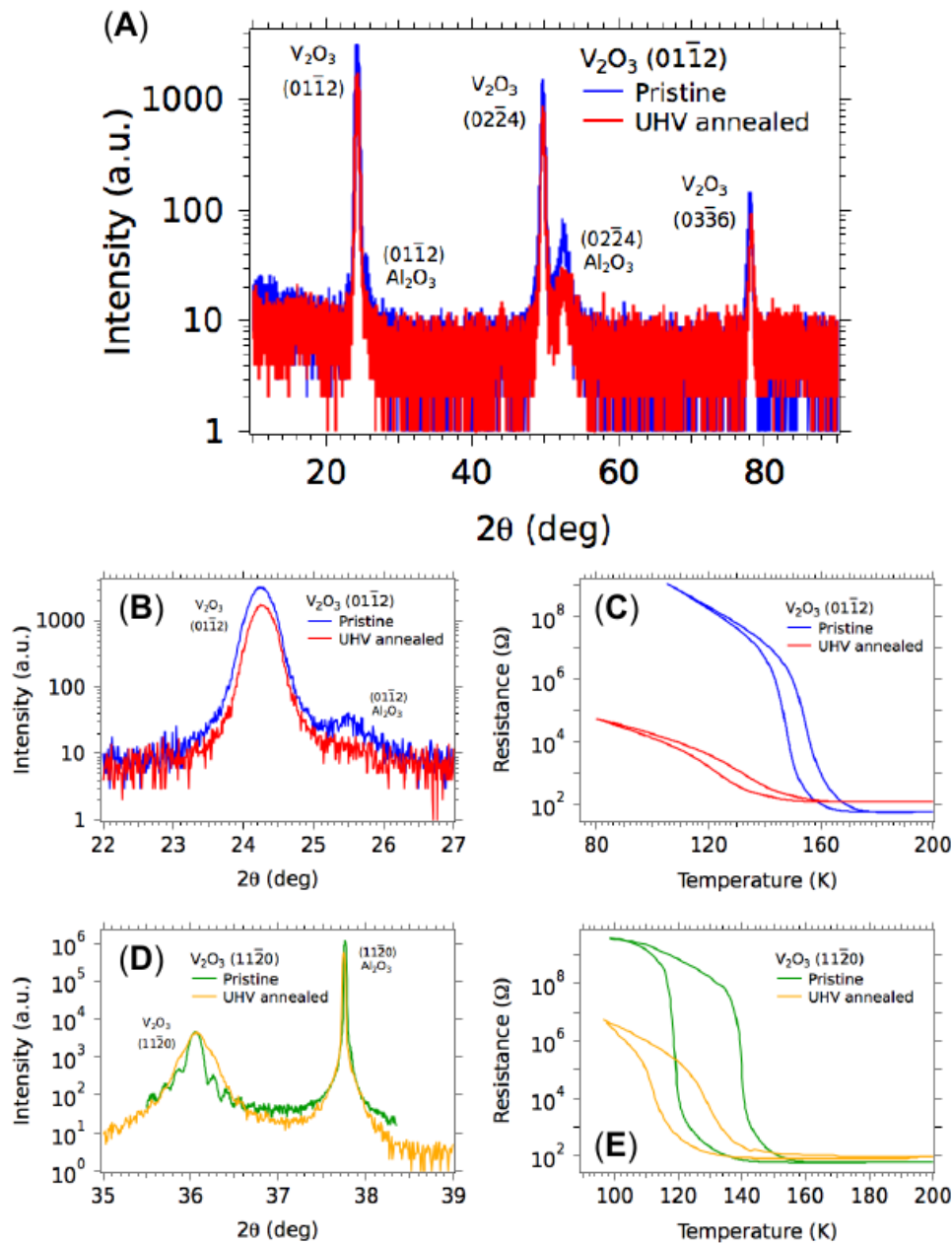


Figure 4.10: X-ray and resistance characterizations of the  $V_2O_3$  films. (A, B) X-ray diffraction characterization, and (C) resistance measurements on a  $V_2O_3/Al_2O_3$  (011 $\bar{2}$ ) thin film used in some of our ARPES experiments (see Fig. 4.18 below), before (blue) and after (red) the in-situ annealing in UHV. Panel (B) is a zoom over the  $V_2O_3$  and  $Al_2O_3$  (011 $\bar{2}$ ) peaks. (D, E) Analogous measurements to (B, C) on the  $V_2O_3/Al_2O_3$  (1120) thin films used in our ARPES experiments, before (green) and after (yellow) the in-situ annealing in UHV.

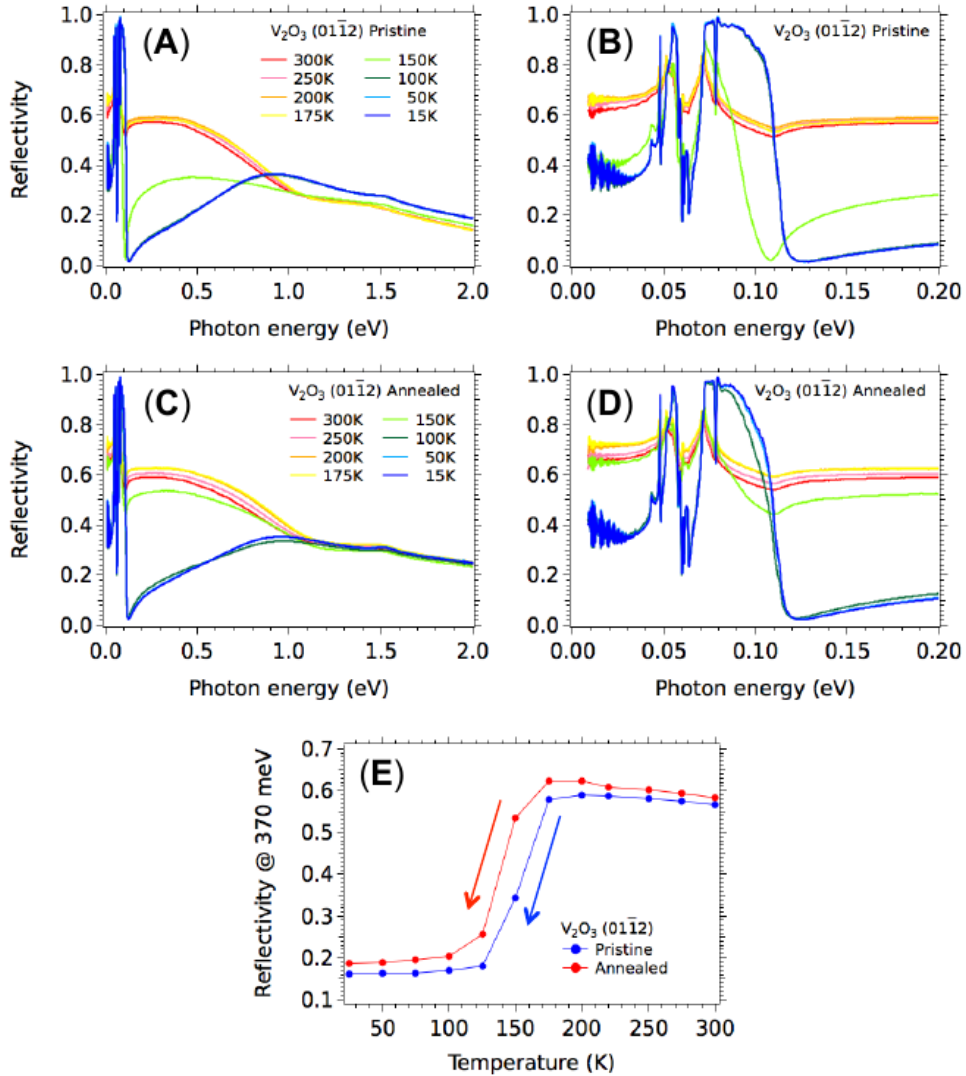


Figure 4.11: (A) Infrared reflectivity measurements for various temperatures (cooling cycle) in a pristine  $V_2O_3/Al_2O_3$  ( $0\ 1\ \bar{1}\ 2$ ) thin film. (B) Zoom of the previous data over the low-energy excitations. (C, D) Similar to (A, B) on a sample of the same batch that was annealed in UHV prior to ARPES measurements. (E) Reflectivity at 370 meV as a function of temperature for both samples. All these data show that the MIT is still present in the annealed sample studied by ARPES, and the onset of the transition has just shifted down in temperature by about 15 K.

### 4.3. Results

#### 4.3.1. Reproducibility of Results in the Paramagnetic Metal Phase

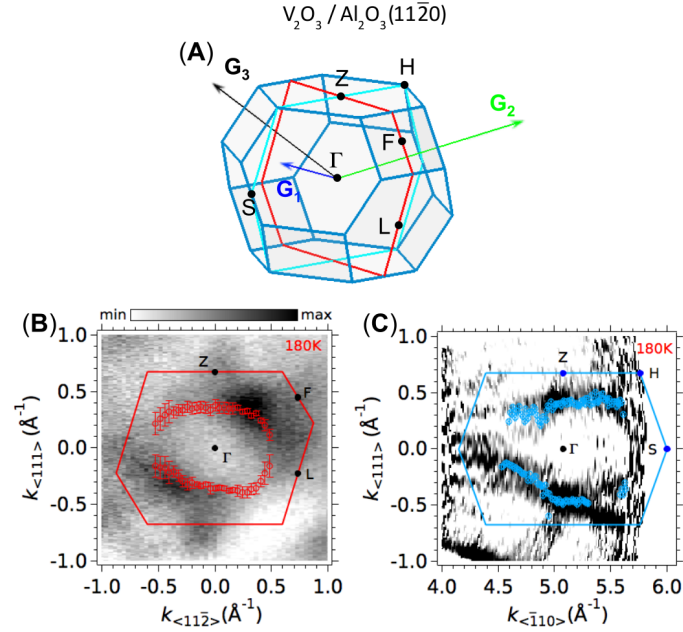


Figure 4.12: In-plane and out-of-plane Fermi surfaces in the metallic state of  $V_2O_3$ . (A) Rhombohedral 3D Brillouin zone of  $V_2O_3$ , showing the primitive vectors of the reciprocal lattice, together with a  $(\bar{1}10)$  plane (red) and a  $(11\bar{2})$  plane (light blue). These planes are, respectively, parallel and perpendicular to the surface of the studied  $V_2O_3/Al_2O_3$   $(11\bar{2}0)$  films. (B) Same in-plane Fermi surface map (metallic state at 180 K) of a  $V_2O_3/Al_2O_3$   $(11\bar{2}0)$ . Red open markers show the experimental Fermi momenta with their respective error bars. Data were measured at 86 eV. (C) Out-of-plane Fermi-surface map (2D curvature) of the same sample. Blue open markers show the experimental Fermi momenta with their respective error bars. Data were acquired by varying the photon energy between 55 eV and 120 eV in steps of 0.5 eV using linear horizontal polarized light.

To help with the orientation in reciprocal space, Figure 4.1 shows the 3D rhombohedral Brillouin zone of  $V_2O_3$  in its metallic phase, together with the 2D plane through  $\Gamma$  parallel to the surface of our films.

Figure 4.12(B) shows the Fermi surface map in the  $(\bar{1}10)$  - plane of a  $V_2O_3/Al_2O_3$   $(11\bar{2}0)$  thin film measured in the metallic state at  $T = 180$  K. One observes a large Fermi sheet around the center of the Brillouin zone ( $\Gamma$ -point), the experimental Fermi momenta are marked in red. Photon energy-dependent ARPES data presented in 4.12(C) shows that the Fermi surface disperses in the momentum

direction perpendicular to the sample surface, demonstrating that the measured states are intrinsic to the bulk 3D electronic structure of the material.

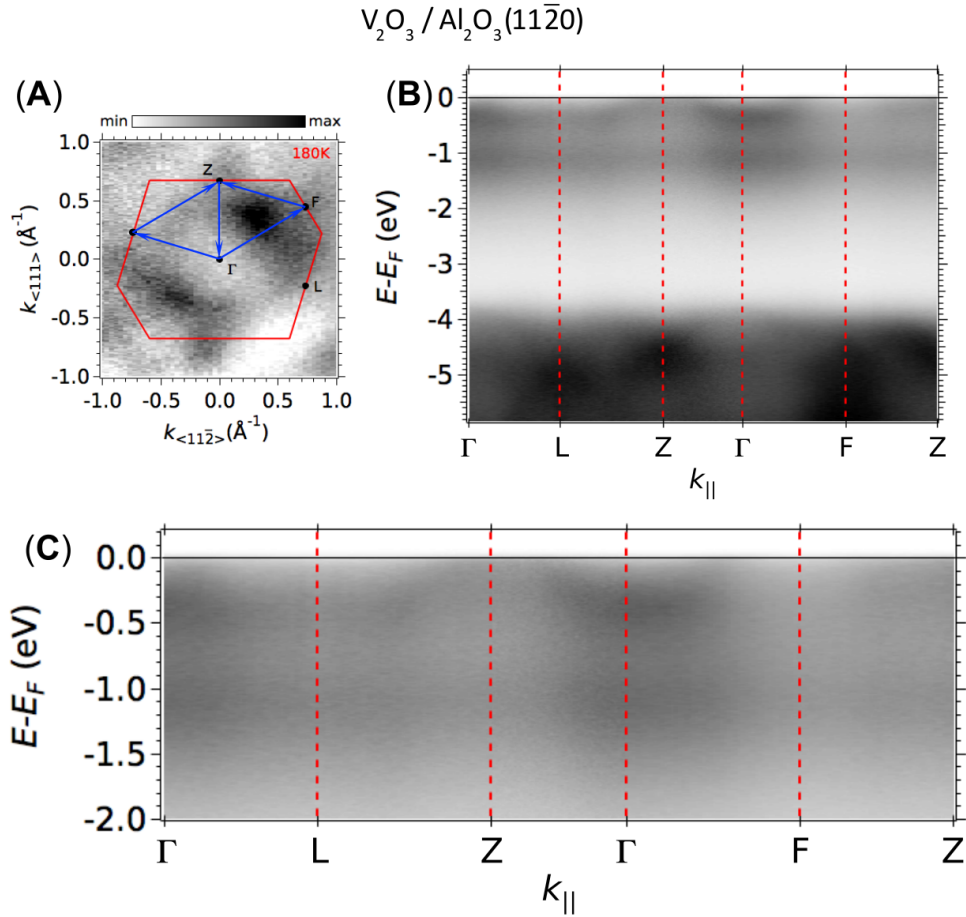


Figure 4.13: Raw ARPES energy-momentum maps in the metallic state of  $V_2O_3$ . (A) Same in-plane Fermi-surface map as shown in 4.12(B) indicating the path in reciprocal space for the raw ARPES energy-momentum maps in the metallic state (180 K) presented in panels (B, C). Data in (B) include the VB-top, MH/OV, QP and QLS bands. Panel (C) is a zoom of (B) over the MH/OV, QP and QLS features.

Figure 4.13(A) shows the  $\Gamma$ -L-Z- $\Gamma$ -F-Z path in reciprocal space, and Figs. 4.13(B, C) show the ARPES energy-momentum maps in the metallic phase along such a path. One observes that the QP state has an electron-like dispersion along  $\Gamma$ Z and  $\Gamma$ F, while along  $\Gamma$ L the state appears broad and, within resolution, non dispersive - such that this Fermi surface sheet would be open around the L points. The state shows a hole-like dispersion along LZ, such that around Z one has a hole-like Fermi pocket. The QLS can be observed as a weak, broad, non-dispersive part of spectral weight near  $E_F$  at all momenta, and is more visible around Z and

along ZFZ.

Figure 4.14 (A) presents the corresponding energy-momentum ARPES map along  $k_{(111)}$ , corresponding to the  $\Gamma$ -Z direction in the rhombohedral metallic phase. The most evident features are an electron-like QP band crossing the Fermi level ( $E_F = 0$ ) and dispersing down to about  $-400$  meV [35, 40], together with a nondispersive state around an energy  $E = -1.1$  eV, assigned to the lower MH band [40], and the valence band (VB) of oxygen p states below about  $E = -4$  eV. All these features are in excellent agreement with previous photoemission and ARPES measurements in the metallic state of single crystals [35, 40]. The clear dispersion of the QP and VBs is, moreover, an experimental proof of the crystalline quality of the thin-film surface. Note also that the MH band has most of its spectral weight concentrated at momenta around  $\Gamma$ , below the bottom of the QP band, similar to what has been seen previously in other correlated electron metals [48, 54]. Part of the nondispersive spectral weight present at the same energy range as the MH band, also observed in previous ARPES works on  $V_2O_3$  [35], might arise from localized states associated to the creation of OVs during the annealing process and/or ultraviolet (UV) irradiation during experiments. Such vacancy states are commonly found at about the same binding energy, namely,  $E - E_F \approx -1$  eV to  $-1.5$  eV, in virtually all transition metal oxides [47, 49, 50, 52, 53], including the correlated metal  $SrVO_3$ , where they superpose with the MH band [47].

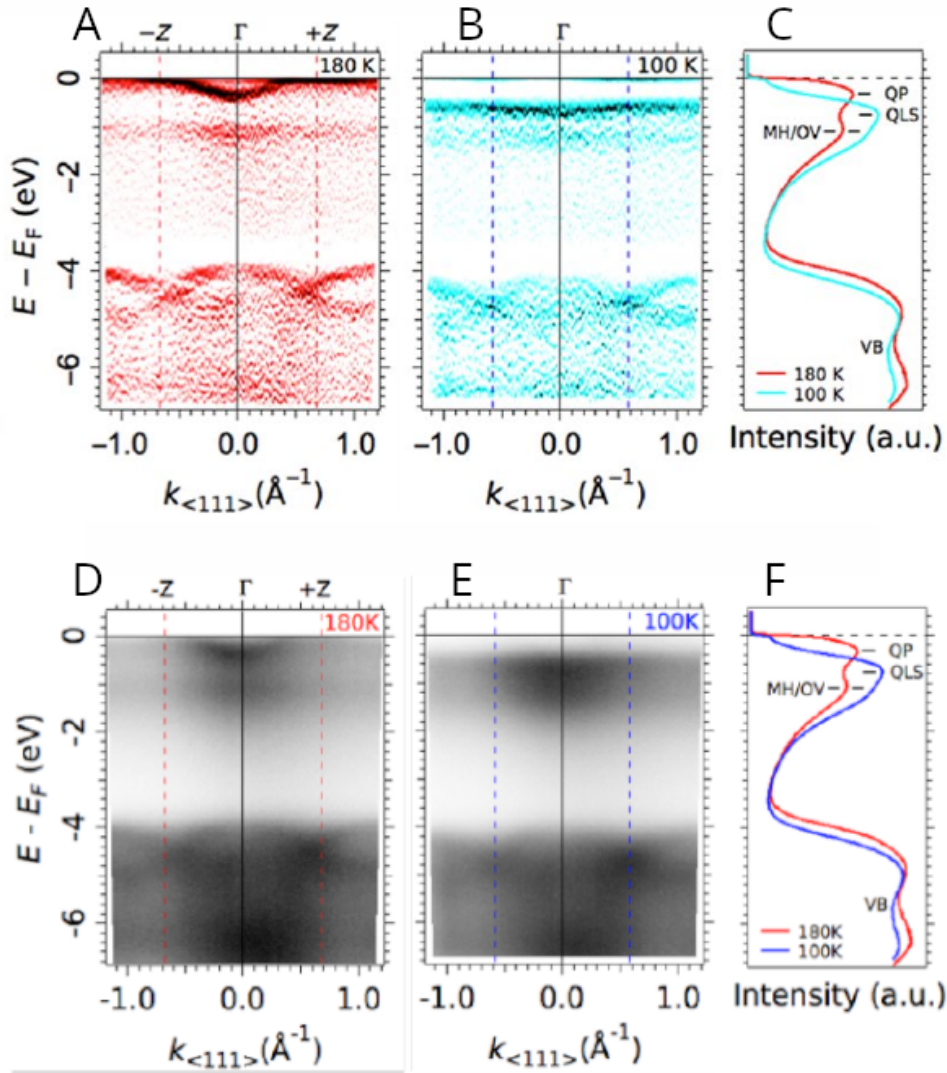


Figure 4.14: Energy-momentum maps (top: 2D curvature, bottom: raw data) along  $k_{\langle 111 \rangle}$  in the metallic (180 K) and insulating (100 K) states, respectively, showing four bands: an electron-like QP band at the Fermi level, visible at 180 K; a weakly dispersive QLS at  $E - E_F \approx -700$  meV, best observed at 100 K; a broad and weakly dispersing MH/OV band around  $E - E_F \approx -1.1$  eV, seen at both temperatures; and the VB of oxygen p states extending from  $E - E_F \approx -4$  eV downward, also present at all temperatures. The rhombohedral Brillouin zone edges ( $\pm Z$  points) at 180 K and the monoclinic zone edges at 100 K are indicated by red and blue dashed lines, respectively. (C,F) Momentum-integrated raw ARPES - intensities from (A,D) and (B,E), showing the QP, QLS, MH/OV, and VB states. All data were measured at a photon energy of 86 eV, corresponding to a bulk  $\Gamma$  point in the  $\langle 110 \rangle$  direction, using linear horizontal polarized light.

### 4.3.2. Spectral Weight Transfer

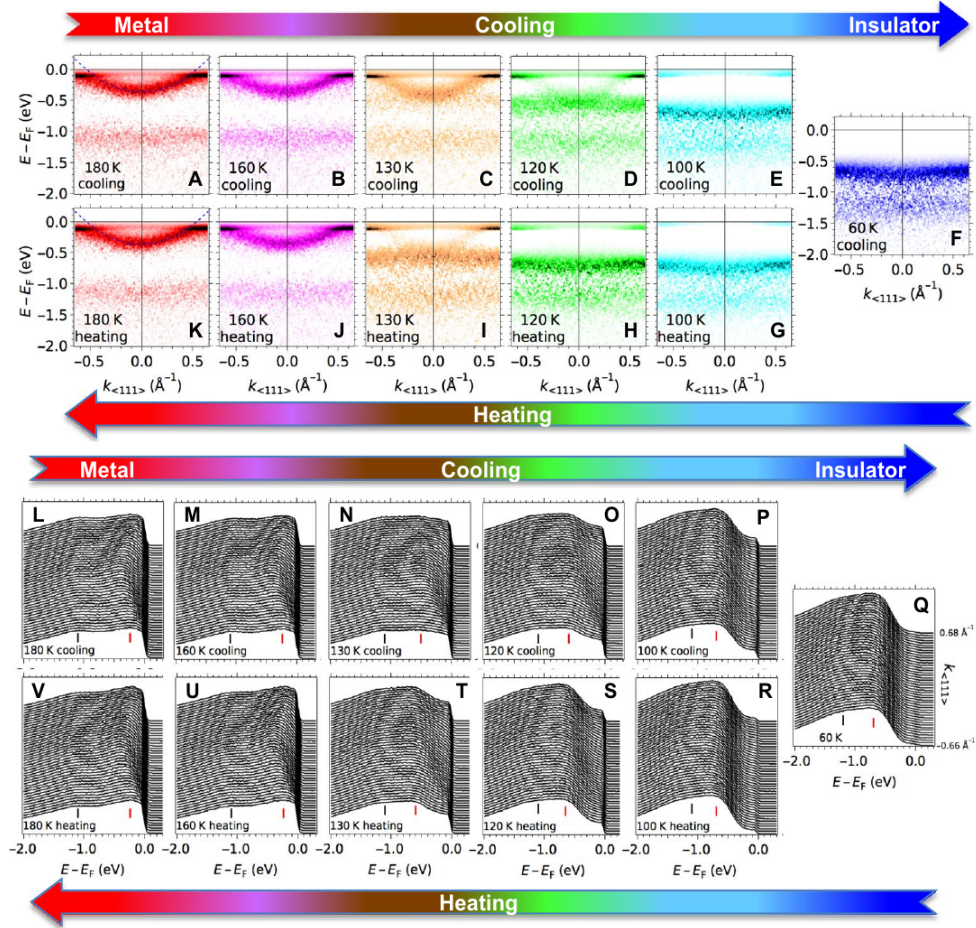


Figure 4.15: Reconstruction and hysteresis of the electronic structure across the MIT. (A to F) Evolution of the ARPES energy-momentum spectra near  $E_F$  (2D curvature of intensity maps) when cooling from 180 K (metallic state) to 60 K (insulating state) in a  $V_2O_3$  ( $1\ 1\ \bar{2}\ 0$ ) thin film. The sharp pileup of intensity at  $E_F$  is a spurious effect of the 2D curvature analysis on the Fermi-Dirac cutoff. (G to K) Corresponding spectra when heating back to 180 K. The blue dashed parabolas in (A) and (K) represent a quasi-free electron band of effective mass  $m^* \approx 3.5m_e$ , assigned to the QP band. (L to V) Raw data associated to (A) to (K). Red and black markers indicate the positions of the QLS and MH/OV bands, respectively.

Thanks to our thin films that preserve their crystal integrity upon cooling, we can now measure the momentum-resolved spectra in the insulating phase. Figure 4.14(B) shows the energy-momentum ARPES map along  $k_{\langle 111 \rangle}$  at  $T = 100$  K, in the insulating state of the  $V_2O_3/Al_2O_3$  ( $1\ 1\ \bar{2}\ 0$ ) thin film. While the VB and the

MH/OV bands remain essentially unchanged, the states near  $E_F$  show a dramatic reconstruction: instead of the strongly dispersive QP state, one observes now a weakly dispersing, previously unreported, quasi-localized state (QLS), at  $E - E_F \approx -700$  meV, different from the MH/OV band. The energy of this QLS gives thus a lower bound to the Mott gap. This agrees well with the gap of about 750 to 800 meV observed in previous optical conductivity studies on  $V_2O_3$  single crystals [55, 56]. It also agrees with our own infrared measurements on the same thin films used for our ARPES experiments, which show a strong decrease in reflectivity below about 800 meV to 900 meV in the insulating phase (fig. 4.11). Note that optical measurements yield the true energy gap between the highest fully occupied state, hence the QLS, and the first unoccupied state above  $E_F$ , not accessible to ARPES.

The QP, QLS, MH/OV, and VB states can also be seen in the momentum-integrated ARPES intensities (4.14(C)). As we will see next, the QP and QLS states are a priori of different nature: The QLS is also present in the metallic phase at energies near  $E_F$ , where it coexists with the QP state — as hinted by previous ARPES work on the metallic phase of  $V_2O_3$  single crystals [43]. However, as the system becomes insulating, the QLS shifts down in energy and increases in intensity, while the QP state gradually loses its spectral weight. Figure 4.15 shows the detailed evolution of the near- $E_F$  electronic structure, when the temperature is first gradually lowered from the metallic (180 K) to the insulating (60 K) state, panels A to F of Fig. 4.15 (curvature of intensity maps) and panels L to Q of Fig. 4.15 (raw data), and then increased back to 180 K (Fig. 4.15 G to K and R to V). In the metallic state at  $T \gtrsim 160$  K (Fig. 4.15, A, B, L, and M), the QP band can be described by a free electron-like parabola of effective mass  $m^* \approx 3.5m_e$  ( $m_e$  is the free electron mass), with its band bottom at  $E_b \approx -400$  meV. The QLS, of weak intensity, can be better seen in the raw data around the Z points (near the edges of the energy-momentum maps, see also Fig. 4.16), beyond the Fermi momenta of the QP band. Its position, at  $E - E_F \gtrsim -240$  meV, is indicated by the red markers in panels L and M of Fig. 4.14. The MH/OV state at  $E - E_F \approx -1.1$  eV is also visible—black markers in panels L and M of Fig. 4.14. As the sample is cooled down and enters the transition regime at 130 K and 120 K (Fig. 4.14, C and D, and N and O), the spectral weight of the QP band decreases, without any noticeable change in its effective mass (i.e., in its energy-momentum dispersion). Simultaneously, the QLS shifts down to an energy  $E \lesssim -400$  meV, becoming more intense as temperature is further lowered. In the insulating state at  $T \lesssim 100$  K (Fig. 4.15, E and F, and P and Q), the QP band has vanished. One observes only the weakly but clearly dispersing QLS at  $E - E_F \approx -700$  meV, which now shows a shallow band minimum at  $\Gamma$  and maxima at the monoclinic Brillouin zone edges (see also Fig. 4.14 B) and the MH/OV band at  $E - E_F \approx -1.1$  eV.

Upon heating up from the insulating state at 60 K back to the metallic state at 180 K (Fig. 4.15, F to K and Q to V), the spectral weight of the QLS decreases,

rapidly shifting up in energy between 130 K and 160 K, while the dispersive QP band reappears. A clear hysteresis in the thermal evolution of the electronic states of the system is present, best seen in the transition regime around 120 K and 130 K [compare Fig. 4.15 (C and D) to Fig. 4.15 (I and H) and Fig. 4.15 (N and O) to Fig. 4.15 (T and S)]. Thus, in the cooling cycle, the QLS becomes more apparent (with respect the QP band) below 120 K, a temperature at which the QP band is still visible, while in the heating cycle, the QLS is clearly visible until 130 K, a temperature at which the QP band only starts to reemerge. The energy shift of the QLS also shows differences between the cooling and heating cycles, best seen when comparing the data at 130 K and 120 K.

To better see the behaviour of the QLS, Fig. 4.16 (A, B) compare the energy distribution curves (EDCs) at the  $\Gamma$  (zone center) and  $\pm Z$  (rhombohedral zone edges) points over, respectively, a cooling and heating cycle across the MIT. Fig. 4.16(C, D) show the temperature evolution (cooling and heating) of the EDCs only at the  $+Z$  point. The data correspond to the spectra shown in Fig. 4.15, including additional temperatures. At 180 K, the broad peak of the QLS around  $E - E_F \approx -240$  meV can be clearly observed at the zone edges. Note that thermal plus resolution broadening of the Fermi-Dirac cutoff occur on a smaller energy scale, of about 20 meV around  $E_F$ , so the peak at  $E - E_F \approx -240$  meV corresponds to an intrinsic spectral feature. As temperature decreases, the peak remains at about the same position down to 140 K, then starts to rapidly shift down in energy until reaching an energy of  $E - E_F \approx -700$  meV at a temperature of 100 K, below which the peak does not evolve further. Upon heating, the QLS peak at the zone edges stays at  $E - E_F \approx -700$  meV until about 120 K. Above this temperature the peak shifts rapidly up in energy until reaching its original high-temperature position at around 150 K.

On the other hand, the EDCs at  $\Gamma$  show an intense peak at  $E - E_F \approx -400$  meV at 180 K. Its asymmetric line-shape, broader at energies above the peak towards  $E_F$ , corresponds to the superposition of the dispersive QP peak and the QLS. As temperature decreases and goes below 140 K, the spectral weight of this peak starts to rapidly decrease at energies above the peak, while the peak itself appears to shift down in energy until reaching  $E - E_F \approx -800$  meV at 100 K, below which the peak does not change appreciably. From the momentum-resolved data, Fig. 4.16, we know that the band minimum and effective mass of the QP state do not change with temperature. Only its intensity decreases upon entering the insulating state. Thus, the thermal evolution of the EDC at  $\Gamma$  actually corresponds to the superposition of two effects: the weight of the QP peak (fixed in energy) becomes weaker upon cooling into the insulating phase, while the peak of the QLS simultaneously shifts down in energy until reaching an energy lower than, but close to, the bottom of the original QP state. Upon heating, the behavior of the EDCs at  $\Gamma$  is reversed, however showing a hysteresis: only at temperatures above 120 K the peak starts to shift up in energy and gain spectral weight at ener-

gies higher than its position, until reaching its final energy position and lineshape at or above 150 K. The energy of the MH/OV state at  $E - E_F \approx -1.1$  eV remains temperature-independent within our resolution.

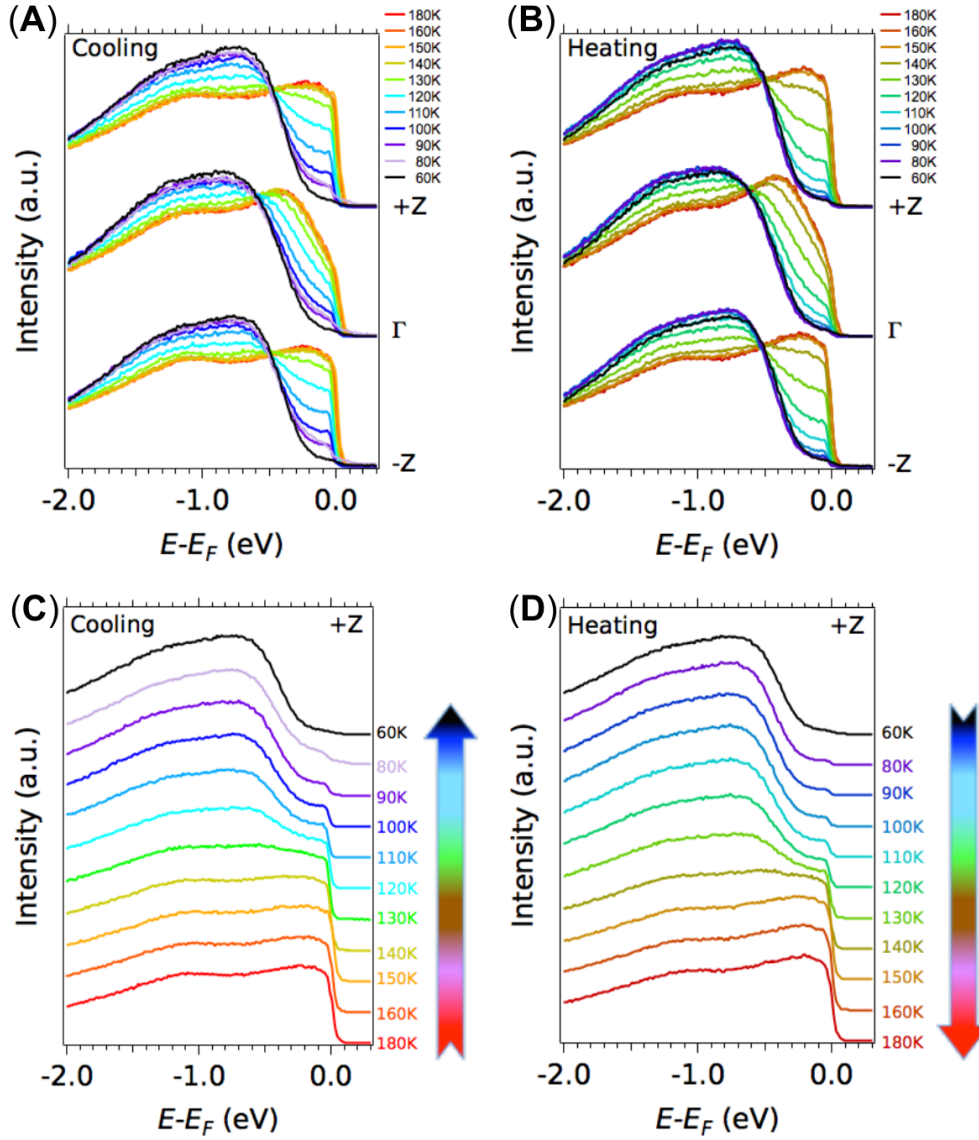


Figure 4.16: Temperature evolution of the spectra at  $\Gamma$  and  $\pm Z$ . (A, B) Energy distribution curves (EDCs) at  $\Gamma$  and  $\pm Z$  (integrated over  $0.03 \text{ \AA}^{-1}$  around each point) over, respectively, a cooling and a heating cycle across the MIT. (C, D) Thermal evolution (cooling and heating) of the EDCs only at the  $+Z$  point. All data in this figure correspond to the spectra shown in Fig. 4.15, including additional temperatures, for a  $\text{V}_2\text{O}_3/\text{Al}_2\text{O}_3$  ( $11\bar{2}0$ ) thin film. Spectra at the same temperature on opposite thermal cycles are shown in slightly different color hues, for clarity.

### 4.3.3. Correlation Between Resistivity Changes and Spectral Weight Transfer

The observation of a hysteresis in the ARPES spectra is related to the previously mentioned formation of phase domains in the sample, an intrinsic characteristic of first-order phase transitions. The size of these domains in  $V_2O_3$  is up to a few  $\mu\text{m}$ .

As the UV spot used in our experiments has a mean diameter larger than about  $30\ \mu\text{m}$ , the ARPES signal is a superposition of electrons emitted from both metallic and insulating phases. We then approximate the observed ARPES intensity  $I(E, k, T)$  at a temperature  $T$  as a superposition of the intensity measured in the pure metallic phase ( $T = 180\ \text{K}$ ) at each energy  $E$  and wave vector  $k$  and the intensity measured in the pure insulating phase ( $T = 60\ \text{K}$ ) at the same energy and momentum. In doing so, we are assuming that, as suggested from Fig. 4.14, the energy shift of the QLS proceeds rather abruptly with temperature. We also neglect thermal broadening as our energy resolution (of about  $15\ \text{meV}$ ) is already comparable to  $k_B T$  at  $180\ \text{K}$ . Thus, we write

$$I(E, k, T) = a(T) \times I(E, k, 180\ \text{K}) + b(T) \times I(E, k, 60\ \text{K}) \quad (4.4)$$

Using linear regression, we could therefore determine the phase fractions  $a(T) \geq 0$  and  $b(T) \geq 0$  that best fit the measured spectra for all energy and momenta, i.e., over a set of around  $4 \cdot 10^5$  points of  $I(E, k)$ , at each temperature. Figure 4.17 A shows the so-calculated fraction of insulating and metallic domains,  $b/(a + b)$  and  $a/(a + b)$ , as a function of temperature. For comparison, the resistance obtained on the same sample after ARPES measurements (Fig. 4.17 B) is also shown.

A similar behaviour could be found in Fig. 4.18 for a film with  $(01\bar{1}2)$  orientation.

The agreement in the hysteresis between the electrical resistance and the ARPES data (onset of the transition on cooling at around  $140\ \text{K}$  to  $150\ \text{K}$ , mid-point at around  $120\ \text{K}$ , and thermal amplitude of the hysteresis of about  $15\ \text{K}$  to  $20\ \text{K}$ ) indicates that the observed changes in the spectral function are directly linked to the MIT.

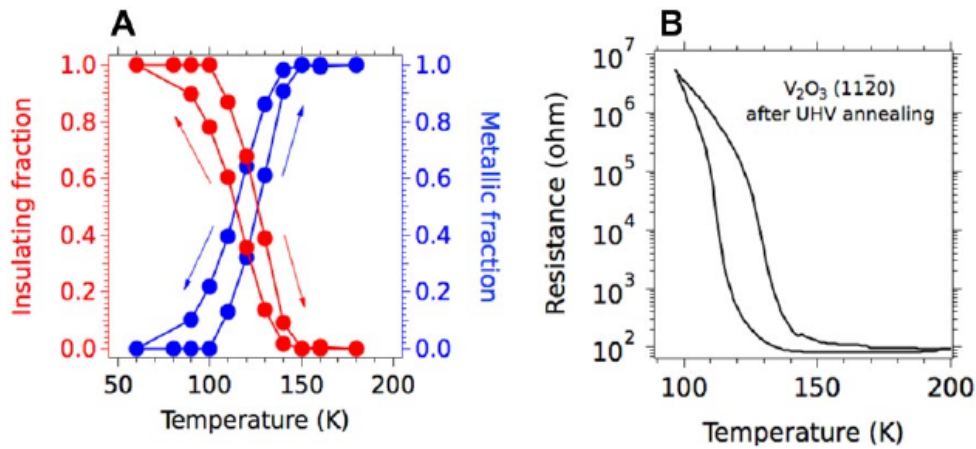


Figure 4.17: Fraction of metallic and insulating electronic domains from ARPES. (A) Representation of the fraction of insulating and metallic domains contributing to the ARPES intensity in a  $V_2O_3/Al_2O_3$  ( $1\ 1\ \bar{2}\ 0$ ) thin film. Error bars in the fits (Eq. (4.4)) are smaller than the size of the symbols. (B) Resistance as a function of temperature measured in the same sample after UHV annealing and photoemission experiments. The shift in transition temperature and the decrease of the resistivity in the insulating phase with respect to the pristine sample (Fig. 4.5) are ascribed to the slight doping with OVs induced by annealing in UHV (see 4.2.2).

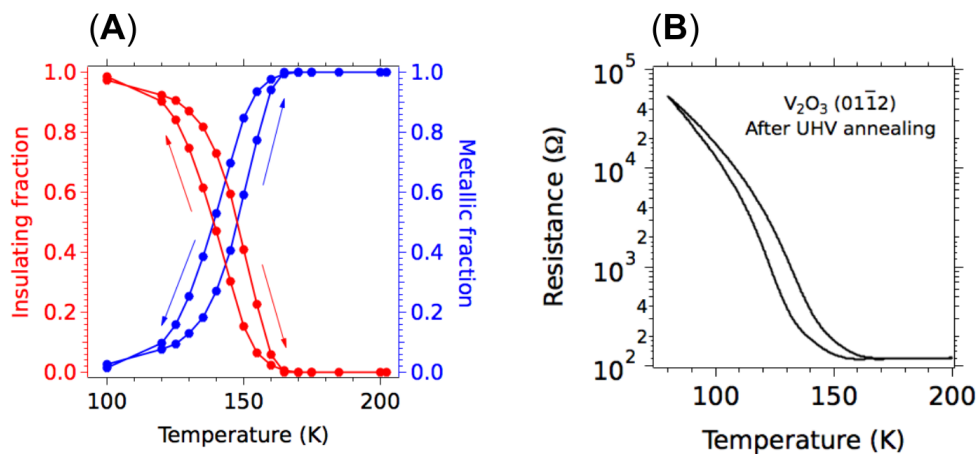


Figure 4.18: Fraction of metallic and insulating electronic domains from ARPES. (A) Representation of the fraction of insulating and metallic domains contributing to the ARPES intensity in a  $V_2O_3/Al_2O_3$  ( $0\ 1\ \bar{1}\ \bar{2}$ ) film. Error bars in the fits (Eq. (4.4)) are smaller than the size of the symbols. (B) Resistance as a function of temperature measured in the same sample after UHV annealing and photoemission experiments.

#### 4.3.4. The Spectral Weight Transfer and Lack of Symmetry Changes

Our temperature-dependent studies were performed along  $k_{\langle 111 \rangle}$ , a direction orthogonal to the antiferromagnetic wave vector in the insulating state. [57, 58] Hence, the band dispersions along this direction should not be directly affected by antiferromagnetic band folding. In line with this expectation, our ARPES data do not show any folding of the dispersive QP state. Instead, the spectral weight of the QP state vanishes as the system goes from metallic to insulating, without any measurable change in its dispersion, while the QLS shifts down in energy and increases in spectral weight. One possibility is that the energy shift of the QLS, which remains essentially non-dispersing along all high-symmetry directions explored in this work (Fig. 4.14 and Fig. 4.13), is associated to its nesting along momenta parallel to the antiferromagnetic wave vector. On the other hand, note that in the insulating state, the magnetic moments are ordered ferromagnetically along  $k_{\langle 111 \rangle}$ . [57] This, of course, can affect the band structure, although in a way different from antiferromagnetic folding. Future theoretical studies should address further how the specific magnetic ordering of  $V_2O_3$  affects its different orbital states.

More generally, our ARPES measurements show that, across the MIT, the essential redistribution of spectral weight in the occupied part of the electronic spectrum occurs between the QP and QLS bands, over an energy range of about 700 meV below  $E_F$ . On the other hand, recent optical measurements show that, while a large suppression of optical conductivity occurs over an energy range of about 1 eV [59–61], a substantial spectral weight transfer extends up to and beyond at least 3 eV [59, 60]. Thus, together, ARPES and optics data indicate that the unoccupied part of the electronic spectrum is also undergoing a major reconstruction, over a large energy range of several eV, across the MIT.

Our observations of spectral weight redistribution among the QP and QLS are consistent with x-ray absorption spectroscopy measurements, which found that the metallic and insulating phases have different orbital occupancies among two states present in both phases. [62, 63] Our findings are also in line with multiorbital first-principles calculations for  $V_2O_3$ . [64–66] In the metallic phase, the dispersive QP band seen in the ARPES spectra and crossing the Fermi level is identified in the calculations as a band of  $a_{1g}$  dominant character, while the remaining spectral weight stems essentially from the  $e_g^\pi$  orbitals. In particular, the latter would be mainly responsible for the spectral weight of the broad QLS around  $E_F$ , as well as the Hubbard band feature around  $E = -1.1$  eV. In the insulating phase, the dispersive  $a_{1g}$  band would be emptied, and only the double peak structure (at energies  $-0.7$  eV and  $-1.1$  eV) of the Hubbard band formed by the now half-filled  $e_g^\pi$  states would survive. [64, 65, 67] Our data provide thus a direct, momentum-resolved illustration of the multiorbital nature of the Mott transition in  $V_2O_3$ .

#### 4.3.5. Lack of Oxidation State Changes

As mentioned in 4.2.2, it is reasonable to ask whether the UHV annealing modified the bulk composition or stoichiometry of the material. As shown, in Figures 4.10 and 4.11, such a cleaning process slightly lowers the MIT onset temperature and decreases the resistance change between the insulating and metallic states, possibly due to the formation of oxygen vacancies. However, it does not affect the bulk structure or stoichiometry of the film nor the overall physical changes across the transition. Such a slight metallization of the sample is actually beneficial for the ARPES measurements, as it allows following the MIT down to the insulating state without excessive charging. Most importantly, as shown in Fig. 4.17, the temperature onset and width of the MIT hysteresis cycle observed by ARPES are in excellent quantitative agreement with those measured by resistivity on the very same samples right after the ARPES measurements.

To further prove that the surface treatment didn't change the near-surface stoichiometry of the samples, we have performed additional XPS measurements on films annealed in UHV following the same protocol as the one used for the ARPES measurements. Fig. 4.19 compares our results to published XPS reference spectra for different vanadium oxides. Our data correspond well to  $V_2O_3$ . Specifically, we observe the  $V-2p_{1/2}$  and  $V-2p_{3/2}$  peaks at binding energies of  $(-523.54 \pm 0.05)$  eV and  $(-515.95 \pm 0.05)$  eV, respectively, and the  $O-1s$  peak at an energy of  $(-530.70 \pm 0.02)$  eV. The separation between the  $O-1s$  and  $V-2p_{3/2}$  peaks in our data, namely 14.75 eV, is in excellent agreement with the one of the reference spectra, reported as 14.5 eV and 14.85 eV [68, 70, 71]. Moreover, the shoulder close to 513 eV seen in our data is also identified in previous reference spectra as a signature of the metallic correlated state of  $V_2O_3$  [69]. The side feature of the  $O-1s$  peak at  $(532.68 \pm 0.05)$  eV has been assigned to residual carbon contamination on the oxide surface [68], but its presence does not invalidate the conclusion that the surface obtained after UHV annealing still has the  $V_2O_3$  stoichiometry.

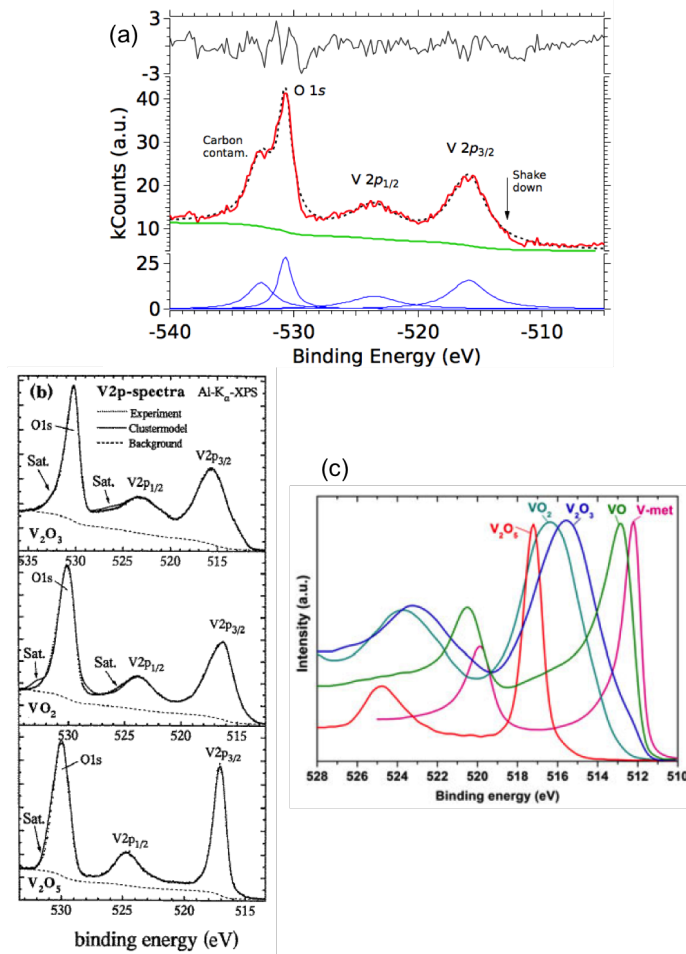


Figure 4.19: (A) XPS spectrum of one of our  $V_2O_3/Al_2O_3$  thin films (middle panel, red curve) after annealing in UHV during 5 min at  $650^\circ C$  and performing ARPES measurements. The  $O-1s$ ,  $V-2p_{1/2}$  and  $V-2p_{3/2}$  peaks are shown. The side feature of the  $O-1s$  peak at  $(532.68 \pm 0.05) eV$  has been assigned to residual carbon contamination on the oxide surface [68]. The spectrum was fitted using four Lorentzians (blue curves) with a Shirley background (green curve). The fit residuals are shown in the top panel (black curve). The shoulder close to  $-513 eV$  seen in our data is a signature of the metallic correlated state of  $V_2O_3$  [69]. (B) Reference XPS spectra of different stoichiometric vanadium oxides [68]. The overall shape and separation between the  $O-1s$  and  $V-2p_{3/2}$  peaks in our data, namely  $14.75 eV$ , is in excellent agreement with the ones of the reference spectra for  $V_2O_3$ . (c) Zoom over the  $V-2p$  doublet for metallic vanadium and for different vanadium oxides, showing the characteristic energy shift of the peaks depending on the compound [70]. The energies of the  $V-2p$  peaks in our XPS spectrum correspond to the ones of  $V_2O_3$ .

## 5 - Driving the Hidden Order Transition in URu<sub>2</sub>Si<sub>2</sub> by P-doping

Uranium ruthenium silicide URu<sub>2</sub>Si<sub>2</sub>, a heavy Fermion compound, undergoes a phase transition at  $T_{HO} = 17.5$  K whose order parameter is still unknown over three decades after its discovery [72, 73]. A wide variety of experimental techniques have been employed in order to detect the ordering below this temperature, but its nature remains elusive. For this reason, the phase is commonly referred to as *hidden order* (HO) phase.

### 5.1. Previous Work

#### 5.1.1. Basic Information about URu<sub>2</sub>Si<sub>2</sub>

At room temperature, the compound crystallizes as a paramagnetic metal with a body-centred tetragonal (BCT) structure with crystal parameters  $a = b = 4.15868$  Å and  $c = 9.57253$  Å,  $\alpha = \beta = \gamma = 90^\circ$ . The existence of the hidden order phase transition is shown by experimental evidence like specific heat measurements (see Fig. 5.3), which clearly indicate a second order phase transition, but the corresponding order parameter defining the phase below  $T_{HO}$  remains a mystery [75].

The Brillouin zone corresponding to the BCT unit cell is shown in Fig. 5.2 in red. In the HO phase, alternating Uranium planes are inequivalent [76], resulting in a smaller simple tetragonal (ST) BZ shown in black lines in 5.2. Note that this changes the symmetry around the X-point from 2-fold to 4-fold, as observed in [74].

At the (001) surface, the projection of neighbouring  $\Gamma$  points in all phases results in a two-dimensional surface BZ with the same square shape of the ST BZ in that plane. Because ARPES experiments with UV light at the photon energy of 50.5 eV used in our experiments dominantly probe the surface region, throughout 5.3 we will employ the square BZ border corresponding to the surface and the ST bulk BZ.

A second temperature-induced transition happens below 1.5 K, where the bulk becomes superconducting, and it has been shown that the temperature for both transitions can be lowered by doping the silicon sites with phosphorous, down to complete suppression of the hidden order phase at  $x \approx 0.03$  and the emergence of an antiferromagnetic phase at  $x \gtrsim 0.27$ . [77, 78] The phase diagram for temperature and doping is shown in Fig. 5.4

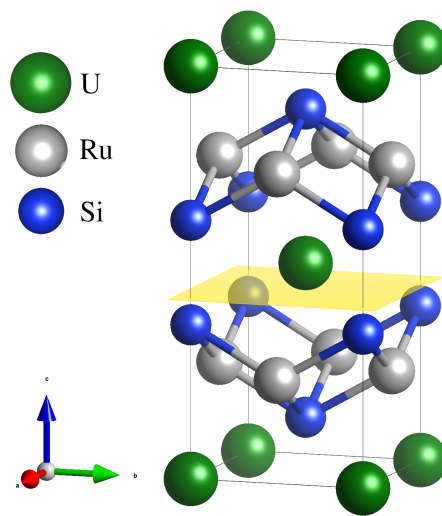


Figure 5.1: Crystal structure of URu<sub>2</sub>Si<sub>2</sub>. The symmetry is BCT with parameters  $a = b = 4.15868 \text{ \AA}$ ;  $c = 9.57253 \text{ \AA}$  and  $\alpha = \beta = \gamma = 90^\circ$ . An easy cleaving plane exists between the Uranium atoms and the Silicon planes, perpendicular to the  $c$ -axis. The Silicon-terminated cleavage plane is marked in yellow. The first Uranium plane below that cleavage (bottom of this graph) will be called the near-surface layer (U<sub>1</sub>), with progressively bulk-like layers (U<sub>2</sub>, U<sub>3</sub>) below.

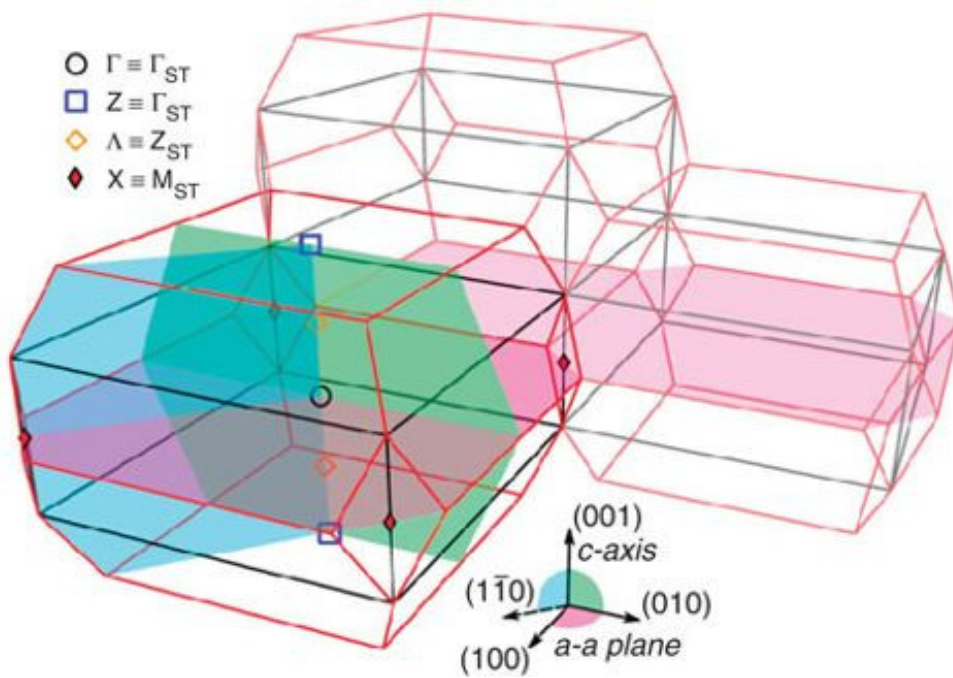


Figure 5.2: Reciprocal space symmetry of  $URu_2Si_2$ . The Brillouin zone corresponding to the crystal structure is drawn in red, and the Brillouin zone corresponding to the simple tetragonal lattice in the HO state, as observed by Bareille *et al.* in [74], is also drawn in black. Adapted from [74].

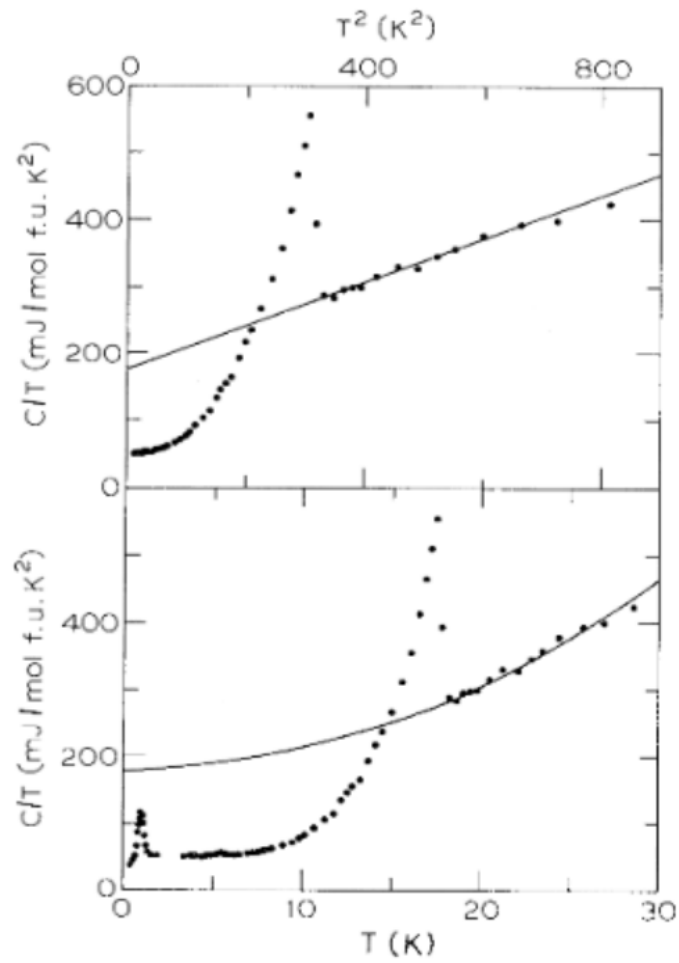


Figure 5.3: Specific heat  $C/T$  of  $\text{URu}_2\text{Si}_2$  as measured by Palstra *et al.* [72]. The divergence around  $T_{HO}$  is clearly visible and indicates a second order phase transition.

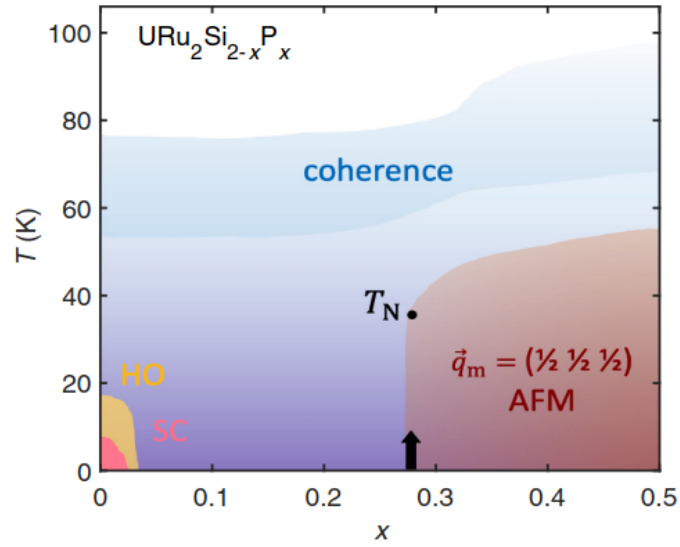


Figure 5.4: Phase diagram of  $\text{URu}_2\text{Si}_{2-x}\text{P}_x$ . The hidden order phase is marked in yellow and can be suppressed by doping with P in the Si sites. At  $x \approx 0.03$ , the hidden order phase is completely suppressed, giving rise to a quantum critical point. Enclosed by the HO phase and marked in red is the superconducting phase, and with strong doping of  $x \gtrsim 0.27$ , an antiferromagnetic phase starts to emerge (opaque red). Figure taken from [79].

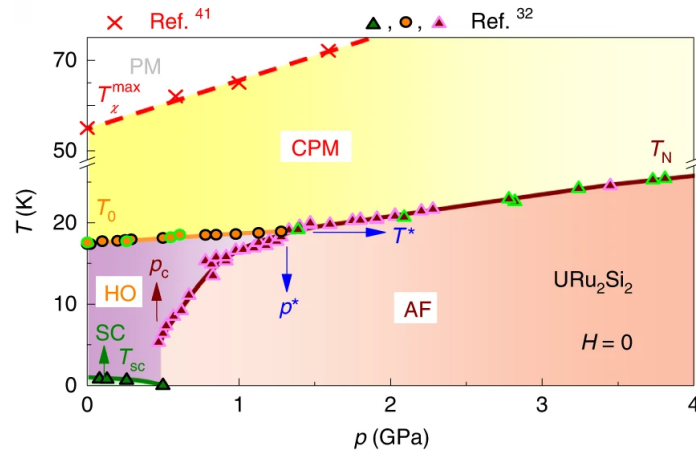


Figure 5.5: Phase diagram of  $\text{URu}_2\text{Si}_2$  as a function of pressure and temperature. The Hidden Order phase is marked in purple, the superconducting phase in green. If the HO phase is suppressed by pressure instead of P-doping, the system directly becomes antiferromagnetic (red), without passing through the paramagnetic phase (yellow, at higher temperatures). Figure taken from [80].

### 5.1.2. The Electronic Structure in the Paramagnetic and Hidden Order Phases

In the attempt to understand the nature of the HO transition, the electronic structure of  $\text{URu}_2\text{Si}_2$  has been studied extensively in recent years. ARPES experiments have been performed on the pure compound both above [81–83] and below [74, 84]  $T_{HO}$ . The results presented in 5.3 are centred around  $\Gamma$  and X, and this overview will focus on these points accordingly. A detailed review of ARPES on  $\text{URu}_2\text{Si}_2$  has recently been published in [76].

Throughout the Brillouin zone, a heavy band of U- $5f$  character disperses just below the Fermi level. At the  $\Gamma$ -point, an M-shaped band formed by interacting heavy and light states forms two Fermi-surface contours (see Fig. 5.6). Around this central shape, four petal-like contours along (100) and (010) are present in the hidden order state, corresponding to electron-like pockets. An assessment of the electronic structure by density functional theory calculations is not trivially possible, as it would require the unknown ordering to be specified. By assuming the ordering to be similar to the neighbouring AFM phase (see pressure-dependent phase diagram in Fig. 5.5), Elgazzar *et al.* [85] could perform such calculations. In these, significant changes of the Fermi surface of this electron pocket were predicted for the transition (see Fig. 5.7). In the paramagnetic phase, the surrounding Fermi surface contour would be diamond-shaped, while in the HO phase, gapping would reduce this contour to petals along the (100) and (010) axis. This could be directly observed by ARPES [74] for the transition in pure  $\text{URu}_2\text{Si}_2$  - see Fig. 5.6. The distinctive behaviour of this feature across the temperature-induced transition gives rise to the question whether a similar change happens across the doping-induced transition that will be detailed in 5.1.3.

In a previous ARPES study of the compound in the HO phase, a heavy quasi-particle band was found to cross the Fermi level as the system cools down to HO. The experimental results also suggest a hybridization of this heavy band with the conduction band [84]. A later experimental study found spectroscopic fingerprints of changes in symmetry of the Fermi surface following symmetry changes of the electronic Brillouin zone from body centered tetragonal (BCT) in the paramagnetic phase, to simple tetragonal in the HO-phase [74]. Note that the crystal itself keeps its BCT structure across the transition, meaning that the change in symmetry must be *purely electronic*. [86] These two Brillouin zones are illustrated in Fig. 5.2.

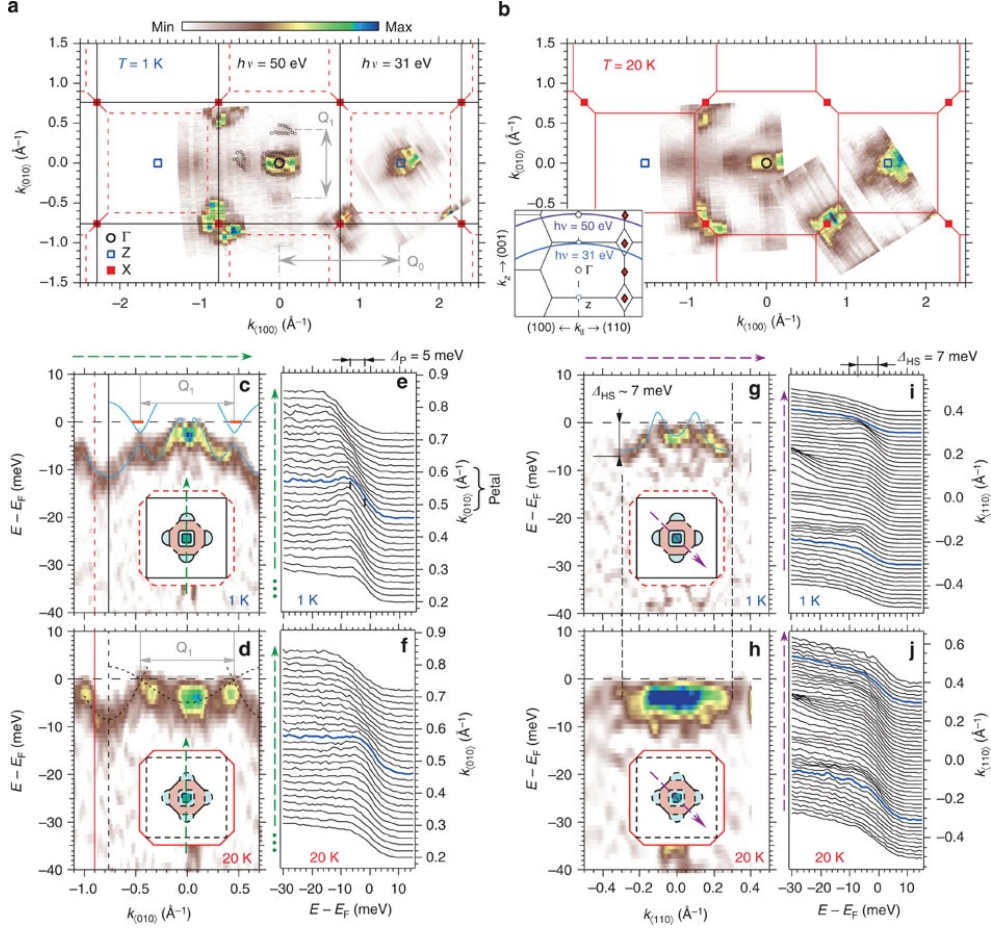


Figure 5.6: The electronic structure across the temperature-induced hidden order transition around  $\Gamma$  as measured by Bareille *et al.* The Fermi surface in the HO phase (a) and paramagnetic phase (b) in the center of the Brillouin zone is formed by an M-shaped band formed by interacting heavy and light states, visible in the energy-momentum maps along (010) (c,g) and (110) (d,i) (all second derivatives). (e,f,i,j) show the raw EDCs corresponding to these dispersions. In the vicinity of the  $\Gamma$ -point, a heavy quasiparticle band forms an additional Fermi surface contour that in the Hidden Order state is shaped like 4 petals along (100) and (010), as visible in (a) In the high-temperature phase in (b), these petals are linked, forming a diamond-shape. Figure taken from [74].

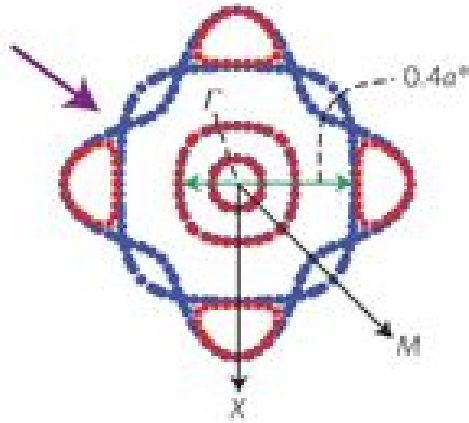


Figure 5.7: DFT calculations of the electronic structure of  $\text{URu}_2\text{Si}_2$  by Elgazzar *et al.* [85] predict a change in the Fermi surface around the  $\Gamma$ -point, transitioning from a diamond-shaped structure in the PM phase (blue) to petals along the main axis in the HO phase (red).

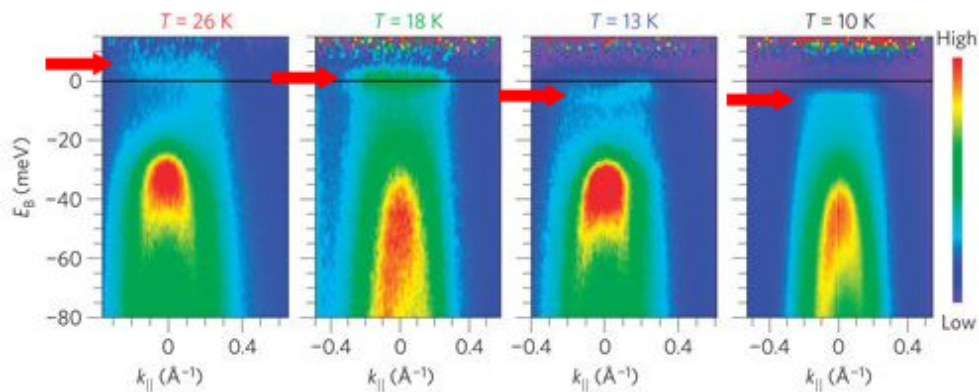


Figure 5.8: ARPES spectra around the  $\Gamma$ -point of  $\text{URu}_2\text{Si}_2$  measured by Santander-Syro *et al.* in [84] (figure adapted). As the temperature decreases through  $T_{HO}$ , a heavy quasi-particle band (marked by red arrows) appears and crosses the Fermi energy from above.

### 5.1.3. Phosphorous Doping

A. Gallagher *et al.* found that the transition to the hidden order phase can be controlled by doping the silicon site with phosphorous ( $\text{URu}_2\text{Si}_{2-x}\text{P}_x$ ), and that at  $x \approx 0.035$  doping, the HO was suppressed completely, while an antiferromagnetic phase emerges at  $x \approx 0.26$  [77, 78]. The corresponding phase diagram is shown in 5.4, with the paramagnetic state in blue and the hidden order phase is shown in yellow towards the origin of the diagram. Phosphorous, being situated directly next to Silicon in the periodic table, has an additional valence electron when compared to the Silicon it is used to dope, so this doping directly introduces electrons into the band structure. However, the dominant effect of this doping has been found to mimic that of hydrostatic pressure by lattice compression [79, 87, 88]. Some models suggest that high pressure could weaken the Ru  $4d$  and U  $5f$  interactions, preventing the screening of magnetic coupling, which could explain the emergence of the AFM phase by pressure [80]. It is therefore of interest whether Phosphorous doping decreases such interactions in a similar manner.

The observation that doping with phosphorous changes  $T_{HO}$  down to the annihilation of the HO state is another example of a quantum phase transition in a heavy-fermion compound. It is also very important for spectroscopic studies and lies at the center of this thesis work, because one can compare the paramagnetic phase and the HO phase at the same experimental temperature. Especially, a comparison of the changes in the Fermi surface induced by P-doping with those predicted [85] or observed [74] in the pure compound can help understanding the nature of the HO state.

## 5.2. Our Experiments

### 5.2.1. Our Samples

Monocrystalline samples of pure and phosphorous-doped  $\text{URu}_2\text{Si}_{2-x}\text{P}_x$  were produced by the group of Ryan Baumbach, Florida State University and Tallahassee MagLab, using a modified Bridgman Technique described in [89]. The phosphorus concentrations of the doped samples were determined by energy-dispersive x-ray spectroscopy (EDX) to be  $x = 0.07$  and  $x = 0.27$ . Crystal orientation was determined by Laue diffractometry after transport to Europe, allowing also the verification of the crystal integrity.

### 5.2.2. Experimental Methods

At the UE112-PGM-2b-1<sup>3</sup> endstation of BESSY II the samples were cleaved *in-situ* at a (001)-oriented surface. Fig. 5.9 (b) shows the Si  $2p$  corelevel spectrum for our lightly doped sample. When compared to the reference spectra in Fig. 5.9 (a), they show this cleavage to be Si-terminated. Additionally, the strong presence of a dispersive hole-like state at the X-point that will be presented in 5.3.2 indicates Silicon-terminated surface [76]. We could successfully obtain clean

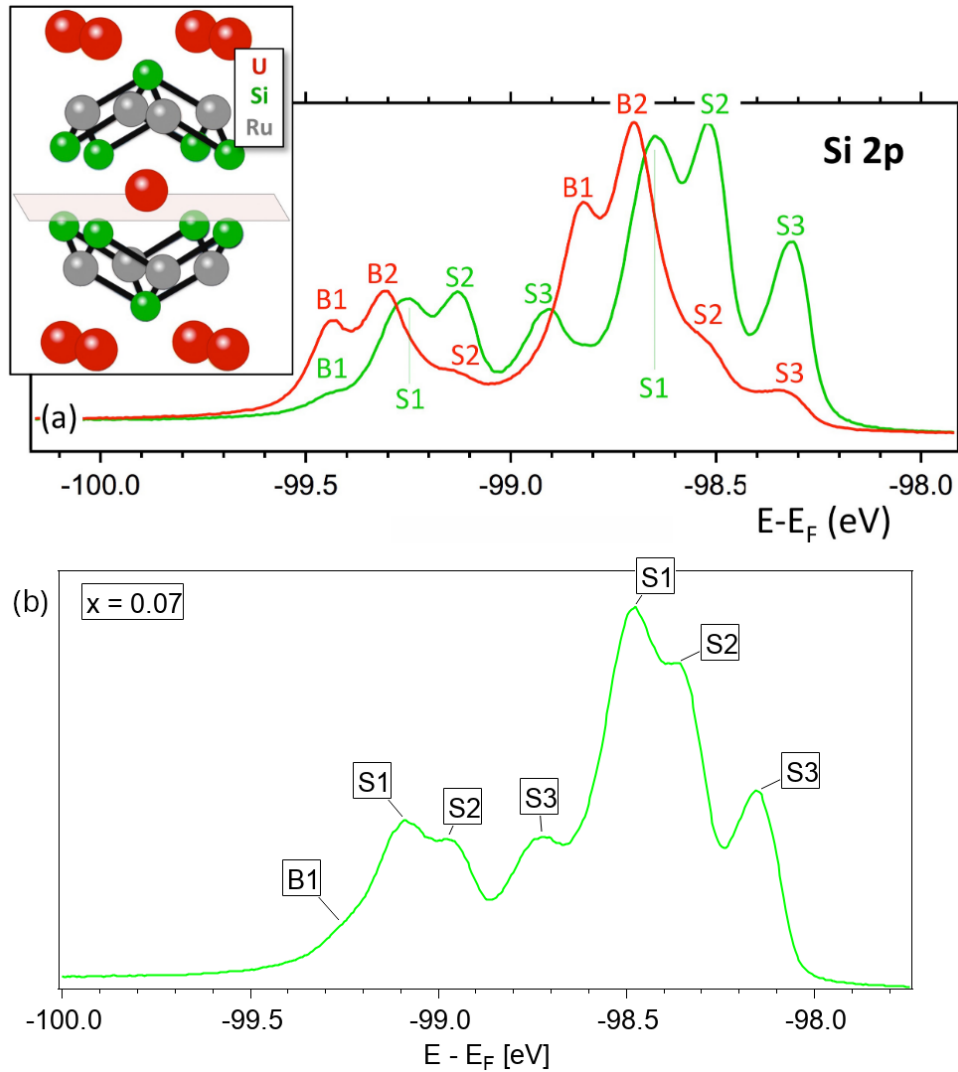


Figure 5.9: (a) Reference spectrum of the Si  $2p$  corelevel spectrum for Si (green) and U (red) terminated surfaces from [90]. (b) Si  $2p$  corelevels for our doped sample ( $x = 0.07$ ). The strong similarity with the Si-terminated spectrum from (a) suggests the same termination on our sample. All spectra were measured with nominal photon energies of 151.5 eV, corresponding to the third harmonics of the monochromator set up for 50.5 eV. The mismatch of  $\sim 200$  meV between the Si-terminated spectrum in (a) and the spectrum in (b) could be explained by a difference in monochromator alignment of  $\sim 100$  meV.

crystalline surfaces showing dispersive states in ARPES experiments with a resolution in energy of 3 meV to 7 meV. For both doped and undoped samples, the sample temperature was consistently around 1.4 K, significantly below the hidden

order transition for the pure compound. Accordingly, changes in the electronic structure between the samples should be reduced to those created by the doping. If not noted otherwise, the photon energy for these measurements was 50.5 eV, corresponding to a bulk  $\Gamma$ -point at normal emission, as seen in the inset in Fig. 5.6 (b), where a similar sample orientation was used.

### 5.3. Results

#### 5.3.1. Fermi Surface Changes around Gamma

Figure 5.10 shows the Fermi surfaces of the pure compound (a) and a phosphorous-doped sample, both at a temperature of 1.4 K, corresponding thus to the HO and PM states, respectively. Note that while the pure compound at this temperature is already in the superconducting state, the corresponding gap that would open on top of the HO state is at least an order of magnitude smaller than our experimental resolution, and any possible changes associated with superconductivity cannot be seen in the present analysis. In the lightly doped sample in Fig. 5.10 (b) and (d), 0.07 Silicon atoms per primitive unit cell, or 3.5 %, are replaced by Phosphorous. In Fig. 5.10(a), centered around the  $\Gamma$ -point, there is a strong, square contour with  $k_F \approx 0.2 \text{ \AA}^{-1}$ , and a weak, more circular inner contour. This is consistent with previous findings in the HO phase, where these contours have been identified as formed by the light-hole conduction band and to an M-shaped band that forms as a result of the interaction between heavy and light states [74, 90].

At  $k_F \approx 0.3 \text{ \AA}^{-1}$  to  $0.5 \text{ \AA}^{-1}$ , there are four petal-like structures along the (100) and (010) directions. This feature has been identified to a change in shape from a diamond-shaped to a petal-like structure when cooling down across the hidden order phase transition, and the gapping of the diamond being a feature of the HO phase [74]. The changes for the doping-induced transition shown in Figure 5.10 (a), (b) and (c) are remarkably similar, with strong differences in intensity along the (110)-direction between the HO and PM phases at the same temperature. The Fermi-momenta of the petals as they become diamond corners do not change noticeably within our resolution, but such a shift would be expected if the effective doping with electrons were strong enough to significantly shift the Fermi level. Observed differences originate therefore from changes in the spectral function itself.

The nature of this state becomes more apparent in the energy-momentum-dispersion along (110) for the lightly doped compound in the paramagnetic state shown in Fig. 5.10(d). A heavy electron-like quasi-particle is emerging through the Fermi level around  $\pm 0.4 \text{ \AA}^{-1}$  from the  $\Gamma$ -point. The dispersion measured for the doping-induced paramagnetic state in Fig. 5.10(d) (curvature) indicates a heavy electron band along (110) with  $k_F = \pm 0.4 \text{ \AA}^{-1}$  and the band minimum at  $-9 \text{ meV}$ . This state has previously been observed in the paramagnetic phase of undoped samples above  $T_{HO}$  along (010), but could not be resolved along (110)

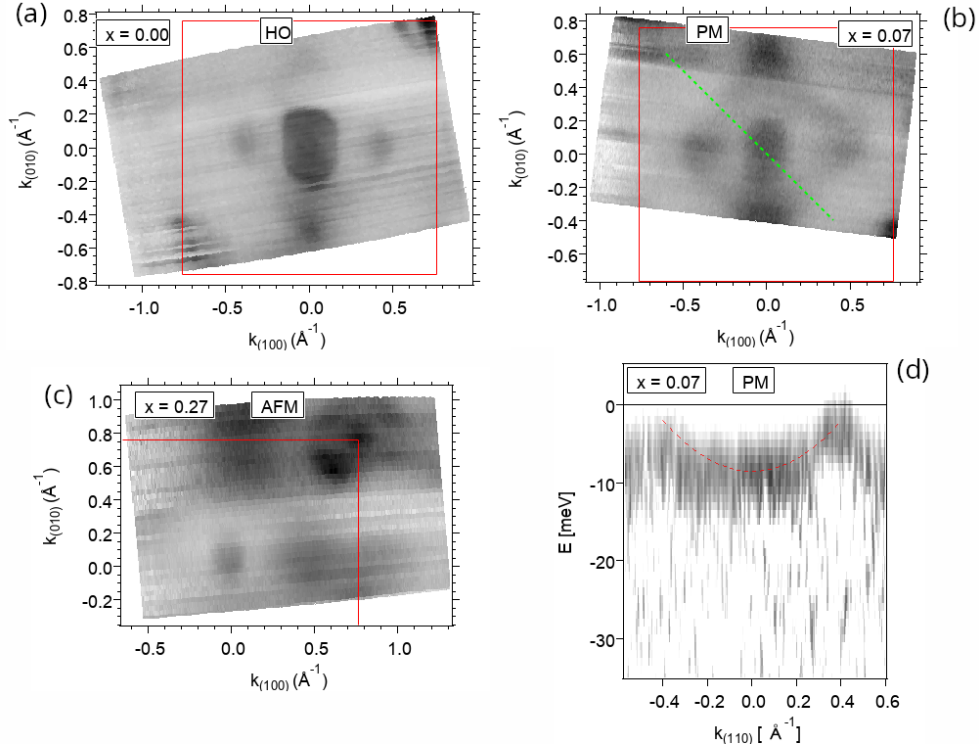


Figure 5.10: (a-c) In-plane Fermi-surface map of a pure  $\text{URu}_2\text{Si}_2$  single crystal (a) in the hidden order state ( $T = 1.4\text{K}$ ), as well as the  $x = 0.07$  phosphorous-doped specimen (b) in the paramagnetic phase and the  $x = 0.27$  doped sample (c) in the antiferromagnetic state at the same temperature. Pronounced differences in intensity along  $(110)$  around the  $\Gamma$ -point are in accordance with previous observations of a temperature-induced phase transition in the pure compound. The ST Brillouin zone is drawn in red for orientation. In the hidden order state (a), the Fermi surface forms four petals around  $\Gamma$ , while in the paramagnetic state (b), these petals are linked, forming a diamond structure. In (c) the petals seem to widen and be separate again. (d) Energy-momentum dispersion (second derivative) along  $(110)$  through the  $\Gamma$ -point as marked by a dashed green line in (b). A heavy quasiparticle band with U-5-f character is dispersing close to the Fermi level and crossing above it at  $\pm 0.3\text{Å}^{-1}$ , creating the diamond-like Fermi surface.

(see Fig. 5.6 (c,d)) [74, 90]. Note that in the hidden order regime, this is replaced by a M-shaped dispersion, with a gap of  $5\text{meV}$  at these Fermi momenta.

When crossing the second quantum phase transition by using a strongly doped sample with  $x = 0.27$ , we arrive in the antiferromagnetic regime. The corresponding Fermi surface is shown in Fig. 5.10 (c). It has a circular contour at the center at  $\Gamma$ , and in the surroundings, a petal-shaped structure along  $(100)$  and  $(010)$

re-emerges again. Notably, along  $(110)$  and  $(1\bar{1}0)$ , the Fermi surface is gapped again, similar to the HO state. In recent ARPES measurements in the AFM phase driven by Fe-doping [90], the same behaviour has been observed, with the petals being linked to the M-shaped interaction band. The close similarity between the HO and AFM phase can be explained by their proximity in the pressure-controlled phase diagram in Fig. 5.5.

### 5.3.2. Hybridisation Changes around X

We now shift our focus to changes around the X-point. Figure 5.11 shows energy-momentum dispersions taken for both the pure and the doped compound at 1.4 K. A heavy electron-like (the almost horizontal line at the Fermi energy) and a strongly dispersive hole-like state (marked by the red parabolas in Fig. 5.11(a-c)) are clearly visible. The latter has previously been suggested as a surface state of the Si-terminated cleaving plane, while the former is of U5f character and has been found to contain a strong surface-state-like behaviour at momenta enclosed by the light hole band (LHB), with a bulk-like component extending out of that range [76]. In the pure compound, a  $\Pi$ -shaped band and the slightly dispersing wings of a heavy electron band (HEB) are visible, indicating Kondo hybridization between a light hole-like band and the HEB. When looking at the doped compound in the paramagnetic phase in Fig. 5.11 (b), the hybridization is visibly suppressed with the light hole band crossing the accordingly flattened HEB 7 meV below the Fermi level. As described later, the experimental Fermi surface contours are in excellent agreement with the absence of hybridization in the doped compound. In previous works Boariu *et al.* have claimed such a hybridisation being unaffected by the temperature-induced HO-transition, with a hybridization gap of 11 meV, independent of temperature [91], while Zhang *et al.* claimed the hybridisation to be lessened at higher temperatures, based on the weaker enhancement of the f-state described below. This indicates that the suppression of the hybridisation is not intrinsically linked to the phase transition.

To quantitatively analyse changes in the light hole band, we extracted its dispersion by fitting each MDC with two Lorentzian peaks. For the resulting values of energy and momentum, a parabolic dispersion was fitted to the energies far below the hybridisation regime. These dispersions are shown in 5.11 (a-c) by dashed lines. From these dispersions, the light hole band shows a strong, continuous change in the energy of its maximum and in the effective mass in the range far away from the hybridising regime. When fitting the band in the range below  $E_F - 400$  meV, the effective mass changes can be calculated from the fit parameters. It is found to decrease from  $m_{eff} \approx -0.8 m_e$  in the pure compound to  $m_{eff} \approx -0.5 m_e$  in the slightly doped sample. A similar analysis in the strongly doped compound below  $E_F - 600$  meV finds an even lighter band with  $m_{eff} \approx -0.2 m_e$ . In the third, strongly doped case, the whole band top sinks to  $-46.3(52)$  meV **below** the Fermi level. Note that this simple model does not correspond to the true shape of the light band,[76] and we employ it purely for the sake of qualitatively comparing

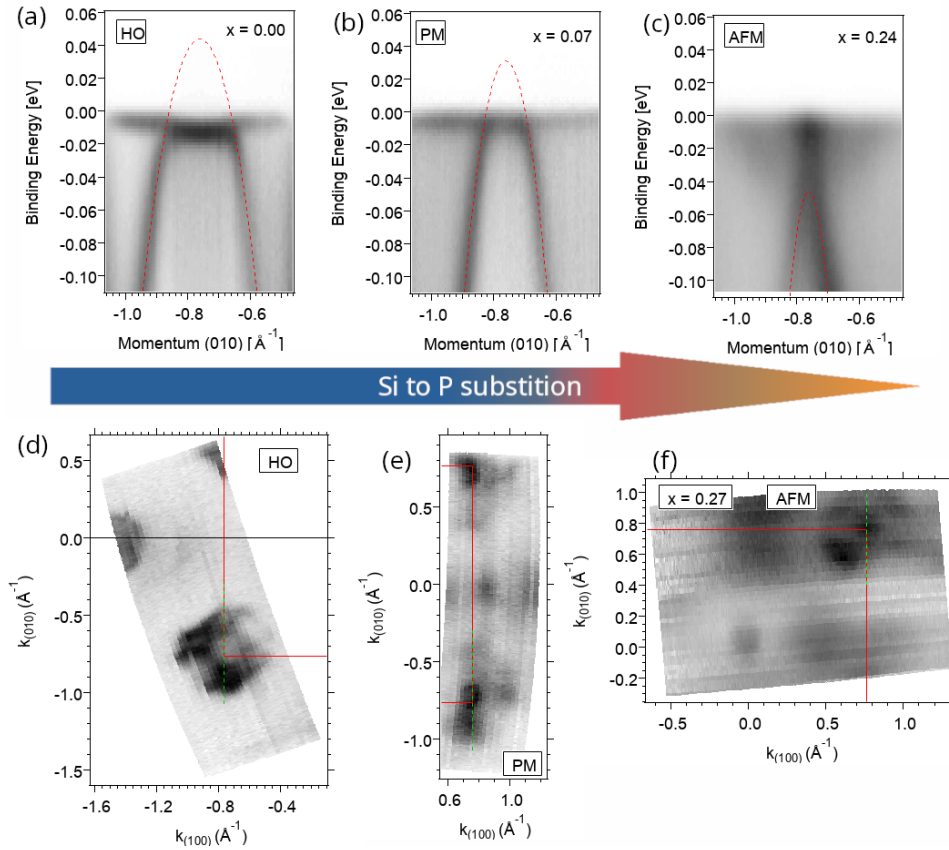


Figure 5.11: The changes around the X-point in the first Brillouin zone (border marked in red) through the doping-induced HO-transition. The dispersions along (010) through X are shown in (a) to (c) and are marked as green lines in the corresponding Fermi surface maps in (d) to (f). In the energy-momentum maps, a strongly dispersing hole-like band, likely from a surface state, and a heavy electron band are evolving with the doping. With increased doping, the light hole band shifts down in energy, and hybridization with the heavy band gets visibly suppressed. Note that the spectral weight of the heavy band in (a) is enhanced in the region enclosed by the LHB by the hybridization. In the Fermi surface in the hidden order state (d), at least two contours are resolved around X, made up of buckles with a gap at the center. Neither of these has a circular shape as would be expected for non-interacting bands. Such a circular shape is present for the doped sample out of the hidden order phase in (e) and (f).

the effective mass. At the same time, the changes in hybridisation happen clearly across the doping-induced hidden order transition.

These changes are reflected in the Fermi surface of the compounds in Fig. 5.11

(d) to (f): In the pure compound, there are outer contours formed by the heavy band around the X-point. The hybridization lowers the band in a circular region right at the X-point, and the resulting gap is visible in the Fermi surface map as a lack of intensity. As the HO phase and the hybridization are suppressed in panel (e) and (f), the circular contour of the light hole band appears at the X-point, closing the gap. The Fermi surface of the heavy band undergoes a reconstruction from an outer circle with buckles along (110) in the HO state to a what appears to be a fourfold symmetry in the paramagnetic and AFM phase. However, the bulk Brillouin zone in the paramagnetic phase is body-centred tetragonal, rendering the symmetry at the X-point twofold. This discrepancy could either be a result of the square surface projection of the BCT BZ, giving credit to the argument that the f-states have a surface component, or simply a lack of detail in our data to resolve the symmetry difference. When comparing Fig. 5.11(e) with the symmetry changes reported in [74], the petals around X connecting pairwise would be expected. Both the dispersions and changes in the Fermi surface contours suggest the hybridization in unique to the hidden order phase.

As the substitution of Silicon with Phosphorous effectively adds 0.07 electrons per unit cell to the system in the weakly doped sample, the Fermi level is expected to rise slightly with respect to the entire spectral function. However, such a small shift cannot explain the strong changes in the hole band maximum, and it would also affect the binding energy of the heavy electron band. As the light hole band is shifting in energy compared to the HEB, we are thus observing a change in the spectral function itself. Since the observed change does not occur across the temperature-induced phase transition, it is an effect caused purely by the doping. Such an observation, however, is not contradictory with the previous designation of the band as a surface state, as the substitution of Silicon by Phosphorous can strongly affect the Silicon-terminated cleaving plane. The change in the band maximum could directly affect the interaction between the hole band and the HEB, and thus determine the strength of their hybridisation.

However, the characterisation of the LHB as a surface state raises the question of how the observed changes are affected to a bulk property like the doping and relevant to the bulk transitions. The identification as a surface state of the LHB is based on two arguments: Firstly, it is not predicted by DFT calculations, but it does appear in slab calculations for Si-terminated surfaces [76, 92]. Secondly, the state has only been observed experimentally on Si-terminated surfaces [76, 92] and lastly, it is strongly affected by ageing in UHV, alkali-metal deposition and H dosing (which fills the Si dangling bonds) [76]. A surface state around  $\Gamma$  has been reported to be affected similarly by ageing [90].

According to Zhang *et al.*, this hole-like band interacts with the bulk f-band [92]. Due to resulting hybridization, the f-spectral weight is redistributed, being significantly enhanced in the interior of the hole-like band. This is in agreement with the prediction of an Anderson lattice model [83]. As a result, a weakly

dispersive electron-like band forms, and this interaction becomes less evident at higher temperatures, in the PM phase of the pure compound [92].

Even though our data in Fig. 5.11 (a) shows the enhancement of the f-band, its spectral weight is still clearly present outside of the interaction region, different from what has been reported before, and the spectral weight of the f-state is much more homogeneous without hybridisation in Fig. 5.11 (b). More importantly, by comparing the different phases at the same temperature, we can rule out the effect of temperature changes on the interaction. The fact that this hybridization change can be caused by temperature and doping, both bulk properties, indicates it being linked to a bulk process.

In conclusion, we experimentally observe the fingerprints of two quantum phase transitions ( $\text{HO} \leftrightarrow \text{PM} \leftrightarrow \text{AFM}$ ) in the electronic band structure of URS. The bandstructure fingerprints are the change of a diamond FS contour to a FS contour consisting of four petals, and clear signs of hybridization between a highly dispersing metallic band and a heavy f-band.

## 6 - Perspectives

### 6.1. Vanadates

#### 6.1.1. Further Experiments on the Phase Transitions of $V_2O_3$

In chapter 4, the modelling of the ARPES data at intermediate temperatures as a superposition of the spectra from the metallic and insulating domains could well reproduce the hysteresis in resistivity. To see in detail how the observed spectral weight transfer occurs locally, an investigation of the electronic structure of single domains by nanoARPES is needed. The domain size of several micrometers can indeed be resolved by nanoARPES, and a corresponding proposal for the ANTARES beamline at the French national synchrotron facility Cassiopee has been accepted.

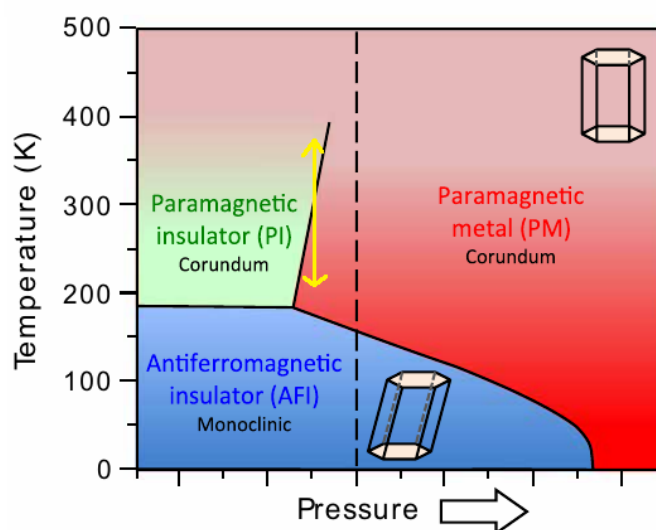


Figure 6.1: In the phase diagram of  $V_2O_3$ , a pure metal-to-insulator transition, unmixed with structural and magnetic changes, should occur along the arrow in bright yellow.

It also remains an open question how precisely the structural, magnetic and electronic transitions are intertwined. We now know that a gap opens in the dispersion along momenta perpendicular to the AFM vector, meaning that AFM alone is not the whole responsible for the gap, but we don't know yet how AFM affects the in-plane Fermi surface. We are currently trying to study (0001)-oriented films, where the antiferromagnetic coupling is in plane, in an attempt investigate this further.

In the phase diagram, at negative pressures there exists a phase border between the paramagnetic metal and paramagnetic insulator states, both with a Corundum

crystal structure. Theoretically, at this border, purely the electronic metal-to-insulator transition should occur, marked as a bright yellow arrow in Fig.6.1. However, in order to study this transition by UHV techniques such as ARPES, pressure would have to be applied chemically, by doping. Until now, the production of doped thin-films has proven difficult, which prevents the imaging of the electronic structure across this transition thus far.

### **6.1.2. The Metal-to-Insulator Transitions of other Vanadates**

As previously mentioned, several compounds in the group of Vanadates exhibit MITs. In Vanadium Dioxide ( $\text{VO}_2$ ), the MIT occurs around 300 K, with a resistivity change of three orders of magnitude. Indeed, recent studies employing similar thin film approach could shed light on this system. [31, 93] These studies, however, are hindered by the photoexciting UV radiation's effect on the films, which dopes the surface and makes the system metallic, destroying the insulating phase. We are confident that this obstacle can be overcome in the near future.

## **6.2. The Hidden Order**

Our data shows the signature of two quantum phase transitions in  $\text{URu}_2\text{Si}_2$ . In the future, we can use the phosphorous doping to continue studying the hidden order transition in detail, leveraging the advantages of low temperatures on experimental resolution. In parallel, an experimental investigation of the effects of the quantum critical point extending to finite temperatures could further our understanding of quantum criticality.

## 7 - Conclusion

To summarize, in the course of this thesis, phase transitions in strongly correlated systems were studied experimentally. By using angle-resolved photoelectron spectroscopy, the electronic structure in reciprocal space could be measured.

In the first presented study, the temperature-induced metal-to-insulator transition in  $V_2O_3$  was investigated on thin films on a substrate of  $Al_2O_3$ . The results show dispersive  $a_{1g}$  quasiparticle and Mott-Hubbard bands in the metallic state, and we observe unique spectral signatures accompanying the transition: The opening of a gap at the Fermi level associated to a decrease in spectral weight of the quasiparticle band, without any change in its effective mass, while the Mott-Hubbard-band remains unaffected by the MIT. The spectral weight is transferred from the conduction band to a non-dispersive  $e_g^\pi$  band, as the latter moves down in binding energy. Furthermore, a clear thermal hysteresis in the gap and the quasiparticle's spectral weight is observed, which is interpreted in terms of the evolution of ratios of metallic/insulating microscopic domains, and that precisely capture the hysteresis in resistivity measured in the same samples.

The second study focuses on the enigmatic Hidden Order transition of  $URu_2Si_2$  driven by phosphorus doping. The signature of the temperature-induced transition in the Fermi-surface contours around the Brillouin zone centre from a diamond to four petals could be observed for the doping-induced transition. When undergoing a second transition to antiferromagnetic state at strong doping, the contours reverted to the shape of the Hidden Order, as is expected due to the proximity of the AFM and HO phases in the pressure controlled phase diagram. A second signature of the transition is found in the suppression of hybridisation between a heavy f-band and a highly dispersive hole-band with surface character.



## 8 - Acknowledgements

The work on this thesis would not have been possible without the direct help, support, and guidance of several people.

First, I would like to thank the doctoral school Physique en Île-de-France for the funding of the work on the thesis, and to the Institut des Sciences Moléculaires d'Orsay and its director, Thomas Pino, for hosting me during that time.

I would like to express my greatest gratitude to Andrés Felipe Santander Syro, who personally and professionally has been the single best thesis supervisor I could wish for, and has been guiding me, answering questions and generally putting up with me. Thank You for the support, the patience, the advice, the cake, the understanding of physics, the experience of beamtimes, QUERCY, and so much more!

All good science is a team effort, and the other current and past members of the SCES group at ISMO have been a great team. Thanks go to Franck Fortuna, Emmanouil Frantzeskakis, Ji Dai, Pedro Henrique Rezende Gonçalves, Amitayush Jha-Thakur and Emma David.

I wish to show my gratitude to Silke Biermann at École Polytechnique, who has been hugely supportive ever since I came to France in my master studies, and has been on the thesis monitoring committee together with Elizabeth Boer-Duchemin, whom I would also like to thank.

Many people from ISMO deserve thanks, including Andrew Maine for his support, Phillipe Roncin, a fellow enthusiastic cyclist, and Céline Dablemont for letting us use the chemistry room (I hope we did not make too much mess). It has also been really nice to share the office with Daniela Torres Díaz - thanks for all the coffee capsules whenever I ran out again - but also Pedro, Amitayush and Emma as well as Martin and Olga in CSNSM before I joined ISMO.

Additionally, I would like to acknowledge several collaborators: Min-Han Lee and the group of Ivan Schuller at the Department of Physics and Center for Advanced Nanoscience, UCSD for the best thin films I have ever worked with, and the team of Ryan E. Baumbach at National High Magnetic Field Laboratory, FSU for the URu<sub>2</sub>Si<sub>2</sub> crystals.

For the hard work on the synchrotrons, I am grateful to Rosa Luca Bouwmeester, and the active help of Patrick Le Fèvre, François Bertran and Julien Rault at CAS-SIOPEE, Emile Rienks at BESSY II, Hiroshi Kumigashira and Ryu Yukawa at KEK Photon Factory has been a huge boon.

My gratitude extends to Rolf Möller and Marie d'Angelo for their work as rapporteurs and to the examinateurs: Odile Stéphan, Rolf Möller, Marie d'Angelo, Roser Valenti and Elena Bascones. When the time had come, the members of the jury raised many interesting points with their questions.

I would also like to thank some friends for all the fun times we had: Giordano,

Linda, Jonas, Victor, Leo, Noémie, Philipp, David, Philipp, Lukas, Jiechu and others for being there when I needed distractions, and my family when I needed support.

Lastly, grazie mille to Alice, who made my life during the thesis an amazing and fun adventure, and got me up and going so many mornings!

## 9 - Annex

### 9.1. Software for Modelling Brillouin Zone Symmetries in Igor Pro

The interpretation of ARPES data of systems with a complex lattice symmetry is often challenging. During synchrotron beamtimes, it is necessary to quickly identify the in-plane orientation and the shape of cuts through both the first and higher Brillouin zones in different sample orientations. This is especially hard when literature shows only conventional, non-primitive unit cells like in  $V_2O_3$ , and an example for such a non-obvious cut is given in Fig. 9.1. This has motivated me to write the BZ\_mapper module of the Igor4Arpes (I4A) tools - the set of tools developed and used by our group for the treatment and analysis of ARPES data.

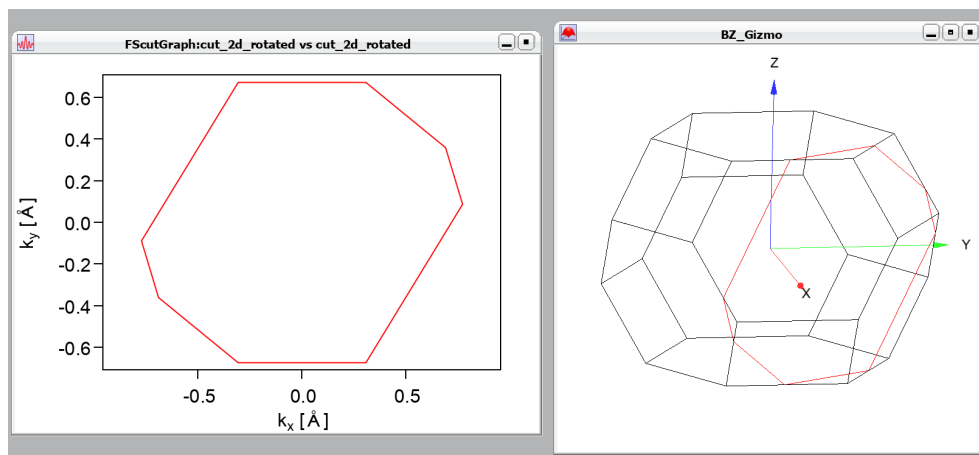


Figure 9.1: An example of a 2D cut with complex symmetry, the  $(11\bar{2}0)$  cut of  $V_2O_3$  at an out-of-plane wave-vector that does not cross the  $\Gamma$  point at normal emission. In this region of the Brillouin zone, the shape and symmetry of the cut across the Brillouin zone changes drastically with small changes in in the out-of-plane direction.

This annex has been written in preparation of a documentation for experienced ARPES users when the tool is made available.

#### Requirements

The BZ\_mapper module is loaded with the standard I4A toolset, or by including the corresponding user interface file directly:

```
#include "I4A_BZcutterControl"
```

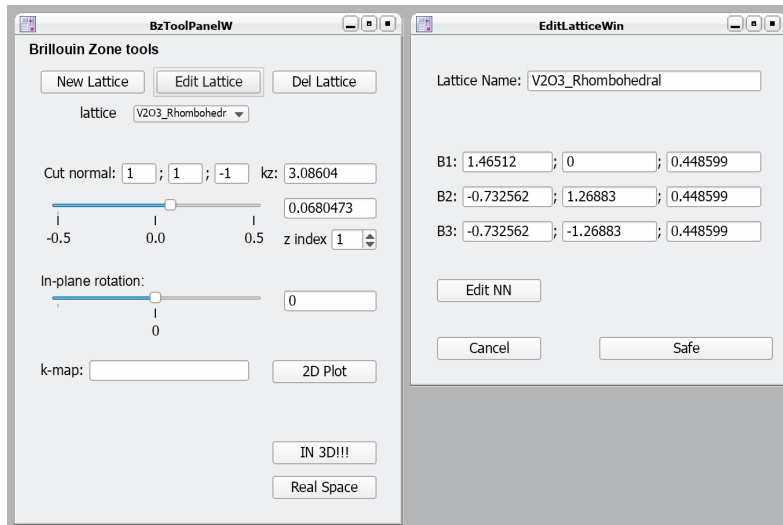


Figure 9.2: Window for creating reciprocal space lattice data

It requires Igor Pro version 8 or higher (previous versions are not natively capable to deal with the quaternions used to represented the rotations in 3-dimensional space).

### Usage

**Creating a Lattice:** For the calculations in reciprocal space, the reciprocal lattice vectors need to be defined in euclidean coordinates. This creates the datastructure of the lattice. When clicking the "New Lattice" button in the main window, a new window opens (see Fig. 9.2) where the primitive base of the reciprocal lattice can be defined. Each line, labelled B1, B2 an B3, represents the three components of a base vector.

Additionally, functions to calculate the reciprocal base from the primitive crystal base in real space, and for importing crystal lattices from cif files, are already implemented in the backend and will be added to the GUI in the near future.

The Button "Edit NN" opens another subwindow, where the neighbouring  $\Gamma$  points that should be considered as nearest neighbours can be selected. **This is not required for the calculations to be correct.** In any 3-dimensional lattice, there are 26  $\Gamma$  points that are potentially nearest neighbours to the  $\vec{0}$ : In terms of the reciprocal base vectors  $\vec{b}_i$ , they take the form

$$\alpha \cdot \vec{b}_1 + \beta \cdot \vec{b}_2 + \gamma \cdot \vec{b}_3 \quad (9.1)$$

, where  $\alpha$ ,  $\beta$  and  $\gamma$  each can take the values  $-1$ ,  $0$  or  $1$ , giving  $3^3 = 27$  possible combinations. Considering that the case  $\alpha = \beta = \gamma = 0$  is not a nearest neighbour, this leaves 26 possible combinations. By default, the procedure iterates over these 26 possible combinations. It then checks if  $\frac{1}{2}\vec{\Gamma}$  is within the first BZ. However,

when calculating cut symmetries up to the 5th BZ, this can take some time, and it might be sped up deselecting the not-nearest neighbours.

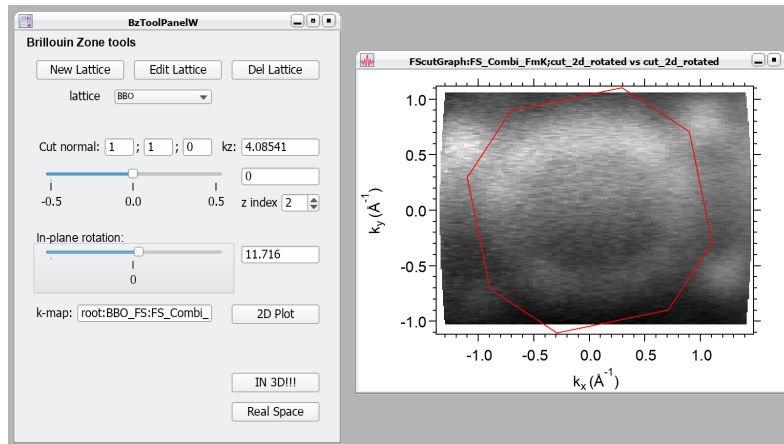


Figure 9.3: Plotting the first BZ border into a 2D FS map. When comparing the symmetry, the angle is not quite correct. The user can then rapidly change the angle of the BZ border to make it correspond to the symmetries of the measured 2D map.

In the main window, select the lattice to work on from the lattice pop up menu, then the crystal direction perpendicular to the cut you want to image in the fields labelled "cut normal". The displacement of the cut along the cut normal direction can be controlled in two ways: The field labelled  $k_z$  specifies the total  $k$  along this direction. Below, there is a slider for the relative displacement within the Brillouin zone from  $-0.5$  to  $0.5$ , with the "z index" denoting the index of the BZ along  $k_z$ . Whenever the total  $k_z$ , the relative displacement or the index of the BZ are changed, the other quantities are calculated accordingly.

Below the  $k_z$  controls is the slider for the in-plane rotation. By pasting the Igor-internal path of a momentum-resolved 2D Fermi map into the k-map field and clicking "2D Plot", the BZ borders in the cut planes can be drawn on the map, and by adjusting the in-plane rotation angle, one can quickly recognize the orientation of the symmetry in the FS map (see Fig. 9.3).

Lastly, the buttons "IN 3D!!!" and "Real space" create Gizmo plots of the 3d Brillouin zone and Wigner-Seitz cell, respectively (see Fig. 9.4).

**Perspectives:** After adding the alternative ways of importing lattice structures to the GUI, it is planned to add the option to plot angle-resolved 2D FS-maps on spherical surfaces, corresponding to the true reciprocal space coordinates of the shown Fermi surface. The calculation of the total  $k_z$ , including the out-of-plane BZ index, was added to supply the radius of this sphere. The Jupyter-based prototype written in Python and with few changes can be used independently of I4A.

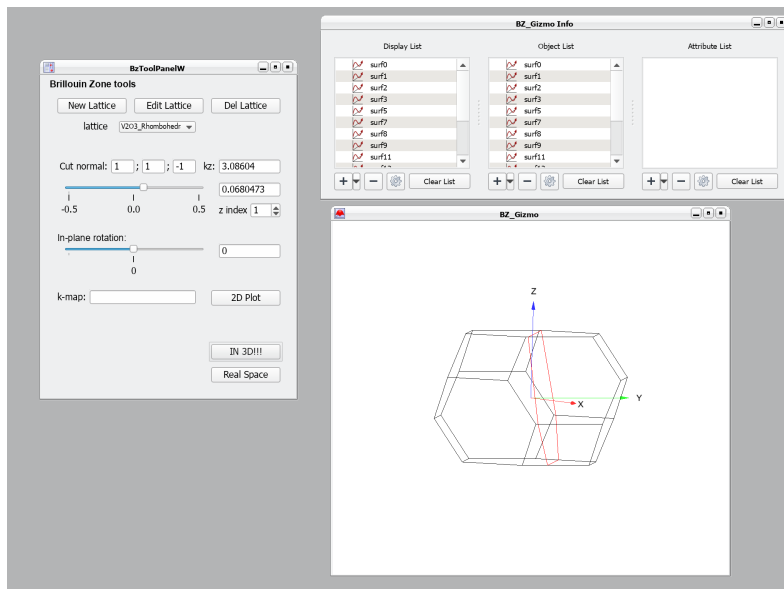


Figure 9.4: Plotting the 3-dimensional BZ and the configured cut in a Gizmo plot.

## Bibliography

- <sup>1</sup>P. W. Anderson, "More is different", *Science* **177**, 393–396 (1972).
- <sup>2</sup>K. Charles, Introduction to solid state physics, eng, 8th edition. (J. Wiley & sons, New York, 2005).
- <sup>3</sup>R. Gross and A. Marx, Festkörperphysik (De Gruyter, 2018).
- <sup>4</sup>N. W. Ashcroft, Solid state physics, eng (2002).
- <sup>5</sup>T. Rödel, "Two-dimensional electron systems in functional oxides studied by photoemission spectroscopy", Theses (Université Paris Saclay (COMUE), Sept. 2016).
- <sup>6</sup>P. A. Lee, N. Nagaosa, and X.-G. Wen, "Doping a mott insulator: physics of high-temperature superconductivity", *Rev. Mod. Phys.* **78**, 17–85 (2006).
- <sup>7</sup>M. Dzero, K. Sun, V. Galitski, and P. Coleman, "Topological kondo insulators", *Phys. Rev. Lett.* **104**, 106408 (2010).
- <sup>8</sup>J. Kondo, "Resistance minimum in dilute magnetic alloys", *Progress of Theoretical Physics* **32**, 37–49 (1964).
- <sup>9</sup>Weigt, Hybridization.png, (2011) <https://commons.wikimedia.org/w/index.php?curid=13301086>.
- <sup>10</sup>N. F. Mott, "The basis of the electron theory of metals, with special reference to the transition metals", *Proceedings of the Physical Society. Section A* **62**, 416–422 (1949).
- <sup>11</sup>M. Imada, A. Fujimori, and Y. Tokura, "Metal-insulator transitions", *Rev. Mod. Phys.* **70**, 1039–1263 (1998).
- <sup>12</sup>Matthieu marechal, Phase-diag2.png, (2008) <https://commons.wikimedia.org/wiki/File:Phase-diag2.svg>.
- <sup>13</sup>U. Nakaya, Snow crystals; natural and artificial, eng (Harvard Univ. Press, 1954).
- <sup>14</sup>K. G. Libbrecht, "The physics of snow crystals", *Reports on Progress in Physics* **68**, 855–895 (2005).
- <sup>15</sup>S. Sachdev and B. Keimer, "Quantum criticality", *Physics Today* **64**, 29–35 (2011).
- <sup>16</sup>P. Coleman and A. J. Schofield, "Quantum criticality", *Nature* **433** (2005).

- <sup>17</sup>H. v. Löhneysen, T. Pietrus, G. Portisch, H. G. Schlager, A. Schröder, M. Sieck, and T. Trappmann, "Non-fermi-liquid behavior in a heavy-fermion alloy at a magnetic instability", *Phys. Rev. Lett.* **72**, 3262–3265 (1994).
- <sup>18</sup>S. R. Julian, C. Pfleiderer, F. M. Grosche, N. D. Mathur, G. J. McMullan, A. J. Diver, I. R. Walker, and G. G. Lonzarich, "The normal states of magnetic d and f transition metals", *Journal of Physics: Condensed Matter* **8**, 9675 (1996).
- <sup>19</sup>S. A. Grigera, R. S. Perry, A. J. Schofield, M. Chiao, S. R. Julian, G. G. Lonzarich, S. I. Ikeda, Y. Maeno, A. J. Millis, and A. P. Mackenzie, "Magnetic field-tuned quantum criticality in the metallic ruthenate  $\text{Sr}_3\text{Ru}_2\text{O}_7$ ", *Science* **294**, 329–332 (2001).
- <sup>20</sup>A. Schröder, G. Aeppli, R. Coldea, M. Adams, O. Stockert, H. v. Löhneysen, E. Bucher, R. Ramazashvili, and P. Coleman, "Onset of antiferromagnetism in heavy-fermion metals", *Nature* **407** (2000).
- <sup>21</sup>G. R. Stewart, "Non-fermi-liquid behavior in *d*- and *f*-electron metals", *Rev. Mod. Phys.* **73**, 797–855 (2001).
- <sup>22</sup>H. Hertz, "Ueber einen einfluss des ultravioletten lichtes auf die elektrische entladung", *Annalen der Physik* **267**, 983–1000 (1887).
- <sup>23</sup>W. Hallwachs, "Ueber den einfluss des lichtes auf electrostatisch geladene körper", *Annalen der Physik* **269**, 301–312.
- <sup>24</sup>A. Einstein, "Ueber einen die erzeugung und verwandlung des lichtes betreffenden heuristischen gesichtspunkt", *Ann. Phys.* **322**, 132–148 (1905).
- <sup>25</sup>F. Reinert and S. Hüfner, "Photoemission spectroscopy—from early days to recent applications", *New Journal of Physics* **7**, 97–97 (2005).
- <sup>26</sup>C. P. 1958-, *Introduction to many-body physics*, eng (Cambridge University Press, Cambridge, 2015).
- <sup>27</sup>M. P. Seah and W. A. Dench, "Quantitative electron spectroscopy of surfaces: a standard data base for electron inelastic mean free paths in solids", *Surface and Interface Analysis* **1**, 2–11 (1979).
- <sup>28</sup>S. Suga and C. Tusche, "Photoelectron spectroscopy in a wide hv region from 6ev to 8kev with full momentum and spin resolution", *Journal of Electron Spectroscopy and Related Phenomena* **200**, Special Anniversary Issue: Volume 200, 119–142 (2015).
- <sup>29</sup>A. F. Santander-Syro, "Electronic structure of exotic states in correlated-fermion materials", habilitation (Université Paris Sud - Paris XI, Apr. 2013).

- <sup>30</sup>C. Bareille, "Effets d'une brisure de symétrie sur les structures électroniques d'URu<sub>2</sub>Si<sub>2</sub> et de KTaO<sub>3</sub>", Theses (Université Paris Sud - Paris XI, Dec. 2013).
- <sup>31</sup>Y. Muraoka, H. Nagao, Y. Yao, T. Wakita, K. Terashima, T. Yokoya, H. Kumigashira, and M. Oshima, "Fermi surface topology in a metallic phase of VO<sub>2</sub> thin films grown on TiO<sub>2</sub>(001) substrates", *Scientific Reports* **8**, 17906 (2018).
- <sup>32</sup>C. Adda, M.-H. Lee, Y. Kalcheim, P. Salev, R. Rocco, N. M. Vargas, N. Ghazikhanian, C.-P. Li, G. Albright, M. Rozenberg, and I. K. Schuller, "Direct observation of the electrically triggered insulator-metal transition in V<sub>3</sub>O<sub>5</sub> far below the transition temperature", *Phys. Rev. X* **12**, 011025 (2022).
- <sup>33</sup>M. Thees, M.-H. Lee, R. L. Bouwmeester, P. H. Rezende-Gonçalves, E. David, A. Zimmers, F. Fortuna, E. Frantzeskakis, N. M. Vargas, Y. Kalcheim, P. L. Fèvre, K. Horiba, H. Kumigashira, S. Biermann, J. Trastoy, M. J. Rozenberg, I. K. Schuller, and A. F. Santander-Syro, "Imaging the itinerant-to-localized transmutation of electrons across the metal-to-insulator transition in V<sub>2</sub>O<sub>3</sub>", *Science Advances* **7**, eabj1164 (2021).
- <sup>34</sup>A. S. McLeod, E. van Heumen, J. G. Ramirez, S. Wang, T. Saerbeck, S. Guenon, M. Goldflam, L. Andereg, P. Kelly, A. Mueller, M. K. Liu, I. K. Schuller, and D. N. Basov, "Nanotextured phase coexistence in the correlated insulator V<sub>2</sub>O<sub>3</sub>", *Nature Physics* **13**, 80–86 (2017).
- <sup>35</sup>I. Lo Vecchio, J. D. Denlinger, O. Krupin, B. J. Kim, P. A. Metcalf, S. Lupi, J. W. Allen, and A. Lanzara, "Fermi surface of metallic V<sub>2</sub>O<sub>3</sub> from angle-resolved photoemission: mid-level filling of  $e_g^\pi$  bands", *Phys. Rev. Lett.* **117**, 166401 (2016).
- <sup>36</sup>S.-K. Mo, J. D. Denlinger, H.-D. Kim, J.-H. Park, J. W. Allen, A. Sekiyama, A. Yamasaki, K. Kadono, S. Suga, Y. Saitoh, T. Muro, P. Metcalf, G. Keller, K. Held, V. Eyert, V. I. Anisimov, and D. Vollhardt, "Prominent quasiparticle peak in the photoemission spectrum of the metallic phase of V<sub>2</sub>O<sub>3</sub>", *Phys. Rev. Lett.* **90**, 186403 (2003).
- <sup>37</sup>M. M. Qazilbash, M. Brehm, B.-G. Chae, P.-C. Ho, G. O. Andreev, B.-J. Kim, S. J. Yun, A. V. Balatsky, M. B. Maple, F. Keilmann, H.-T. Kim, and D. N. Basov, "Mott transition in VO<sub>2</sub> revealed by infrared spectroscopy and nano-imaging", *Science* **318**, 1750–1753 (2007).

- <sup>38</sup>S. Lupi, L. Baldassarre, B. Mansart, A. Perucchi, A. Barinov, P. Dudin, E. Papalazarou, F. Rodolakis, J.-P. Rueff, J.-P. Itié, S. Ravy, D. Nicoletti, P. Postorino, P. Hansmann, N. Parragh, A. Toschi, T. Saha-Dasgupta, O. K. Andersen, G. Sangiovanni, K. Held, and M. Marsi, "A microscopic view on the mott transition in chromium-doped  $v_2o_3$ ", *Nature Communications* **1**, 105 (2010).
- <sup>39</sup>B. A. Frandsen, L. Liu, S. C. Cheung, Z. Guguchia, R. Khasanov, E. Morenzoni, T. J. S. Munsie, A. M. Hallas, M. N. Wilson, Y. Cai, G. M. Luke, B. Chen, W. Li, C. Jin, C. Ding, S. Guo, F. Ning, T. U. Ito, W. Higemoto, S. J. L. Billinge, S. Sakamoto, A. Fujimori, T. Murakami, H. Kageyama, J. A. Alonso, G. Kotliar, M. Imada, and Y. J. Uemura, "Volume-wise destruction of the antiferromagnetic mott insulating state through quantum tuning", *Nature Communications* **7**, 12519 (2016).
- <sup>40</sup>S.-K. Mo, H.-D. Kim, J. D. Denlinger, J. W. Allen, J.-H. Park, A. Sekiyama, A. Yamasaki, S. Suga, Y. Saitoh, T. Muro, and P. Metcalf, "Photoemission study of  $(V_{1-x}M_x)_2O_3$  ( $M = Cr, Ti$ )", *Phys. Rev. B* **74**, 165101 (2006).
- <sup>41</sup>S. Shin, S. Suga, M. Taniguchi, M. Fujisawa, H. Kanzaki, A. Fujimori, H. Daimon, Y. Ueda, K. Kosuge, and S. Kachi, "Vacuum-ultraviolet reflectance and photoemission study of the metal-insulator phase transitions in  $VO_2$ ,  $V_6O_{13}$ , and  $V_2O_3$ ", *Phys. Rev. B* **41**, 4993–5009 (1990).
- <sup>42</sup>K. E. Smith and V. E. Henrich, "Photoemission study of composition- and temperature-induced metal-insulator transitions in cr-doped  $V_2O_3$ ", *Phys. Rev. B* **50**, 1382–1390 (1994).
- <sup>43</sup>A. Georges and G. Kotliar, "Hubbard model in infinite dimensions", *Phys. Rev. B* **45**, 6479–6483 (1992).
- <sup>44</sup>I. Valmianski, J. G. Ramirez, C. Urban, X. Batlle, and I. K. Schuller, "Deviation from bulk in the pressure-temperature phase diagram of  $V_2O_3$  thin films", *Phys. Rev. B* **95**, 155132 (2017).
- <sup>45</sup>J. Trastoy, Y. Kalcheim, J. del Valle, I. Valmianski, and I. K. Schuller, "Enhanced metal-insulator transition in  $v_2o_3$  by thermal quenching after growth", *Journal of Materials Science* **53**, 9131–9137 (2018).
- <sup>46</sup>Y. Kalcheim, N. Butakov, N. M. Vargas, M.-H. Lee, J. del Valle, J. Trastoy, P. Salev, J. Schuller, and I. K. Schuller, "Robust coupling between structural and electronic transitions in a mott material", *Phys. Rev. Lett.* **122**, 057601 (2019).
- <sup>47</sup>T. C. Rödel, F. Fortuna, S. Sengupta, E. Frantzeskakis, P. L. Fèvre, F. Bertran, B. Mercey, S. Matzen, G. Agnus, T. Maroutian, P. Lecoeur, and A. F. Santander-Syro, "Universal fabrication of 2d electron systems in functional oxides", *Advanced Materials* **28**, 1976–1980 (2016).

- <sup>48</sup>S. Backes, T. C. Rödel, F. Fortuna, E. Frantzeskakis, P. Le Fèvre, F. Bertran, M. Kobayashi, R. Yukawa, T. Mitsuhashi, M. Kitamura, K. Horiba, H. Kumigashira, R. Saint-Martin, A. Fouchet, B. Berini, Y. Dumont, A. J. Kim, F. Lechermann, H. O. Jeschke, M. J. Rozenberg, R. Valentí, and A. F. Santander-Syro, "Hubbard band versus oxygen vacancy states in the correlated electron metal  $\text{SrVO}_3$ ", *Phys. Rev. B* **94**, 241110 (2016).
- <sup>49</sup>T. C. Rödel, M. Vivek, F. Fortuna, P. Le Fèvre, F. Bertran, R. Weht, J. Goniakowski, M. Gabay, and A. F. Santander-Syro, "Two-dimensional electron systems in  $\text{ATiO}_3$  perovskites ( $A = \text{Ca, Ba, Sr}$ ): control of orbital hybridization and energy order", *Phys. Rev. B* **96**, 041121 (2017).
- <sup>50</sup>P. Lömker, T. C. Rödel, T. Gerber, F. Fortuna, E. Frantzeskakis, P. Le Fèvre, F. ç. Bertran, M. Müller, and A. F. Santander-Syro, "Two-dimensional electron system at the magnetically tunable  $\text{EuO/SrTiO}_3$  interface", *Phys. Rev. Materials* **1**, 062001 (2017).
- <sup>51</sup>T. C. Rödel, J. Dai, F. Fortuna, E. Frantzeskakis, P. Le Fèvre, F. Bertran, M. Kobayashi, R. Yukawa, T. Mitsuhashi, M. Kitamura, K. Horiba, H. Kumigashira, and A. F. Santander-Syro, "High-density two-dimensional electron system induced by oxygen vacancies in  $\text{ZnO}$ ", *Phys. Rev. Materials* **2**, 051601 (2018).
- <sup>52</sup>A. F. Santander-Syro, O. Copie, T. Kondo, F. Fortuna, S. Pailhès, R. Weht, X. G. Qiu, F. Bertran, A. Nicolaou, A. Taleb-Ibrahimi, P. Le Fèvre, G. Herranz, M. Bibes, N. Reyren, Y. Apertet, P. Lecoeur, A. Barthélémy, and M. J. Rozenberg, "Two-dimensional electron gas with universal subbands at the surface of  $\text{SrTiO}_3$ ", *Nature* **469**, 189–193 (2011).
- <sup>53</sup>A. F. Santander-Syro, C. Bareille, F. Fortuna, O. Copie, M. Gabay, F. Bertran, A. Taleb-Ibrahimi, P. Le Fèvre, G. Herranz, N. Reyren, M. Bibes, A. Barthélémy, P. Lecoeur, J. Guevara, and M. J. Rozenberg, "Orbital symmetry reconstruction and strong mass renormalization in the two-dimensional electron gas at the surface of  $\text{KTaO}_3$ ", *Phys. Rev. B* **86**, 121107 (2012).
- <sup>54</sup>M. Takizawa, M. Minohara, H. Kumigashira, D. Toyota, M. Oshima, H. Wadati, T. Yoshida, A. Fujimori, M. Lippmaa, M. Kawasaki, H. Koinuma, G. Sordi, and M. Rozenberg, "Coherent and incoherent  $d$  band dispersions in  $\text{SrVO}_3$ ", *Phys. Rev. B* **80**, 235104 (2009).
- <sup>55</sup>M. J. Rozenberg, G. Kotliar, H. Kajueter, G. A. Thomas, D. H. Rapkine, J. M. Honig, and P. Metcalf, "Optical conductivity in mott-hubbard systems", *Phys. Rev. Lett.* **75**, 105–108 (1995).
- <sup>56</sup>M. J. Rozenberg, G. Kotliar, and H. Kajueter, "Transfer of spectral weight in spectroscopies of correlated electron systems", *Phys. Rev. B* **54**, 8452–8468 (1996).

- <sup>57</sup>R. M. Moon, "Antiferromagnetism in  $V_2O_3$ ", *Phys. Rev. Lett.* **25**, 527–529 (1970).
- <sup>58</sup>W. Bao, C. Broholm, G. Aeppli, P. Dai, J. M. Honig, and P. Metcalf, "Dramatic switching of magnetic exchange in a classic transition metal oxide: evidence for orbital ordering", *Phys. Rev. Lett.* **78**, 507–510 (1997).
- <sup>59</sup>M. M. Qazilbash, A. A. Schafgans, K. S. Burch, S. J. Yun, B. G. Chae, B. J. Kim, H. T. Kim, and D. N. Basov, "Electrodynamics of the vanadium oxides  $VO_2$  and  $V_2O_3$ ", *Phys. Rev. B* **77**, 115121 (2008).
- <sup>60</sup>M. K. Stewart, D. Brownstead, S. Wang, K. G. West, J. G. Ramirez, M. M. Qazilbash, N. B. Perkins, I. K. Schuller, and D. N. Basov, "Insulator-to-metal transition and correlated metallic state of  $v_2o_3$  investigated by optical spectroscopy", *Phys. Rev. B* **85**, 205113 (2012).
- <sup>61</sup>I. Lo Vecchio, L. Baldassarre, F. D'Apuzzo, O. Limaj, D. Nicoletti, A. Perucchi, L. Fan, P. Metcalf, M. Marsi, and S. Lupi, "Optical properties of  $V_2O_3$  in its whole phase diagram", *Phys. Rev. B* **91**, 155133 (2015).
- <sup>62</sup>J.-H. Park, L. H. Tjeng, A. Tanaka, J. W. Allen, C. T. Chen, P. Metcalf, J. M. Honig, F. M. F. de Groot, and G. A. Sawatzky, "Spin and orbital occupation and phase transitions in  $V_2O_3$ ", *Phys. Rev. B* **61**, 11506–11509 (2000).
- <sup>63</sup>F. Rodolakis, P. Hansmann, J.-P. Rueff, A. Toschi, M. W. Haverkort, G. Sangiovanni, A. Tanaka, T. Saha-Dasgupta, O. K. Andersen, K. Held, M. Sikora, I. Alliot, J.-P. Itié, F. Baudelet, P. Wzietek, P. Metcalf, and M. Marsi, "Inequivalent routes across the mott transition in  $V_2O_3$  explored by x-ray absorption", *Phys. Rev. Lett.* **104**, 047401 (2010).
- <sup>64</sup>J. Trastoy, A. Camjayi, J. del Valle, Y. Kalcheim, J.-P. Crocombette, D. A. Gilbert, J. A. Borchers, J. E. Villegas, D. Ravelosona, M. J. Rozenberg, and I. K. Schuller, "Magnetic field frustration of the metal-insulator transition in  $V_2O_3$ ", *Phys. Rev. B* **101**, 245109 (2020).
- <sup>65</sup>D. Grieger and M. Fabrizio, "Low-temperature magnetic ordering and structural distortions in vanadium sesquioxide  $V_2O_3$ ", *Phys. Rev. B* **92**, 075121 (2015).
- <sup>66</sup>F. Lechermann, N. Bernstein, I. I. Mazin, and R. Valentí, "Uncovering the mechanism of the impurity-selective mott transition in paramagnetic  $V_2O_3$ ", *Phys. Rev. Lett.* **121**, 106401 (2018).
- <sup>67</sup>A. I. Poteryaev, M. Ferrero, A. Georges, and O. Parcollet, "Effect of crystal-field splitting and interband hybridization on the metal-insulator transitions of strongly correlated systems", *Phys. Rev. B* **78**, 045115 (2008).

- <sup>68</sup>R. Zimmermann, R. Claessen, F. Reinert, P. Steiner, and S. Hüfner, "Strong hybridization in vanadium oxides: evidence from photoemission and absorption spectroscopy", *Journal of Physics: Condensed Matter* **10**, 5697–5716 (1998).
- <sup>69</sup>G. Panaccione, M. Altarelli, A. Fondacaro, A. Georges, S. Huotari, P. Lacovig, A. Lichtenstein, P. Metcalf, G. Monaco, F. Offi, L. Paolasini, A. Poteryaev, O. Tjernberg, and M. Sacchi, "Coherent peaks and minimal probing depth in photoemission spectroscopy of mott-hubbard systems", *Phys. Rev. Lett.* **97**, 116401 (2006).
- <sup>70</sup>E. Hryha, E. Rutqvist, and L. Nyborg, "Stoichiometric vanadium oxides studied by xps", *Surface and Interface Analysis* **44**, 1022–1025 (2012).
- <sup>71</sup>J. Mendialdua, R. Casanova, and Y. Barboux, "Xps studies of v2o5, v6o13, vo2 and v2o3", *Journal of Electron Spectroscopy and Related Phenomena* **71**, 249–261 (1995).
- <sup>72</sup>T. M. Palstra, A. A. Menovsky, J. v. d. Berg, A. J. Dirkmaat, P. H. Kes, G. J. Nieuwenhuys, and J. A. Mydosh, "Superconducting and magnetic transitions in the heavy-fermion system URu<sub>2</sub>Si<sub>2</sub>", *Phys. Rev. Lett.* **55**, 2727–2730 (1985).
- <sup>73</sup>J. A. Mydosh and P. M. Oppeneer, "Colloquium: hidden order, superconductivity, and magnetism: the unsolved case of URu<sub>2</sub>Si<sub>2</sub>", *Rev. Mod. Phys.* **83**, 1301–1322 (2011).
- <sup>74</sup>C. Bareille, F. L. Boariu, H. Schwab, P. Lejay, F. Reinert, and A. F. Santander-Syro, "Momentum-resolved hidden-order gap reveals symmetry breaking and origin of entropy loss in URu<sub>2</sub>Si<sub>2</sub>", *Nature Communications* **5**, Article, 4326 (2014).
- <sup>75</sup>V. Tripathi, P. Chandra, and P. Coleman, "Sleuthing hidden order", *Nature Physics* **3** (2007).
- <sup>76</sup>J. D. Denlinger, J.-S. Kang, L. Dudy, J. W. Allen, K. Kim, J.-H. Shim, K. Haule, J. L. Sarrao, N. P. Butch, and M. B. Maple, "Global perspectives of the bulk electronic structure of URu<sub>2</sub>Si<sub>2</sub> from angle-resolved photoemission", *Electronic Structure* **4**, 013001 (2022).
- <sup>77</sup>A. Gallagher, K.-W. Chen, C. M. Moir, S. K. Cary, F. Kametani, N. Kikugawa, D. Graf, T. E. Albrecht-Schmitt, S. C. Riggs, A. Shekhter, and R. E. Baumbach, "Unfolding the physics of URu<sub>2</sub>Si<sub>2</sub> through silicon to phosphorus substitution", *Nature Communications* **7**, Article, 10712 (2016).
- <sup>78</sup>A. Gallagher, K.-W. Chen, S. K. Cary, F. Kametani, D. Graf, T. E. Albrecht-Schmitt, A. Shekhter, and R. E. Baumbach, "Thermodynamic and electrical transport investigation of URu<sub>2</sub>Si<sub>2</sub>-xPx", *Journal of Physics: Condensed Matter* **29**, 024004 (2016).

- <sup>79</sup>M. C. Rahn, A. Gallagher, F. Orlandi, D. D. Khalyavin, C. Hoffmann, P. Manuel, R. Baumbach, and M. Janoschek, "Collinear antiferromagnetic order in  $\text{URu}_2\text{Si}_{2-x}\text{P}_x$  revealed by neutron diffraction", *Phys. Rev. B* **103**, 214403 (2021).
- <sup>80</sup>W. Knafo, S. Araki, G. Lapertot, D. Aoki, G. Knebel, and D. Braithwaite, "Destabilization of hidden order in  $\text{uruzsiz}$  under magnetic field and pressure", *Nature Physics* **16**, 942–948 (2020).
- <sup>81</sup>T. Ito, H. Kumigashira, T. Takahashi, Y. Haga, E. Yamamoto, T. Honma, H. Ohkuni, and Y. Onuki, "Band structure and fermi surface of  $\text{URu}_2\text{Si}_2$  studied by high-resolution angle-resolved photoemission spectroscopy", *Phys. Rev. B* **60**, 13390–13395 (1999).
- <sup>82</sup>I. Kawasaki, S.-i. Fujimori, Y. Takeda, T. Okane, A. Yasui, Y. Saitoh, H. Yamagami, Y. Haga, E. Yamamoto, and Y. Onuki, "Band structure and fermi surface of  $\text{URu}_2\text{Si}_2$  studied by soft x-ray angle-resolved photoemission spectroscopy", *Phys. Rev. B* **83**, 235121 (2011).
- <sup>83</sup>J. Denlinger, G.-H. Gweon, J. Allen, C. Olson, M. Maple, J. Sarrao, P. Armstrong, Z. Fisk, and H. Yamagami, "Comparative study of the electronic structure of  $\text{xruzsiz}$ : probing the anderson lattice", *Journal of Electron Spectroscopy and Related Phenomena* **117-118**, Strongly correlated systems, 347–369 (2001).
- <sup>84</sup>A. F. Santander-Syro, M. Klein, F. L. Boariu, A. Nuber, P. Lejay, and F. Reinert, "Fermi-surface instability at the 'hidden-order' transition of  $\text{URu}_2\text{Si}_2$ ", *Nature Physics* **5**, 637 (2009).
- <sup>85</sup>S. Elgazzar, J. Ruzs, M. Amft, P. M. Oppeneer, and J. A. Mydosh, "Hidden order in  $\text{uruzsiz}$  originates from fermi surface gapping induced by dynamic symmetry?breaking", *Nature Materials* **8**, Article, 337 (2009).
- <sup>86</sup>N. Kernavanois, P. de Réotier, A. Yaouanc, J.-P. Sanchez, K. Liß, and P. Lejay, "Investigation of the crystal structure of  $\text{uruzsiz}$  by high-resolution x-ray diffraction", *Physica B: Condensed Matter* **259-261**, 648–649 (1999).
- <sup>87</sup>K. R. Shirer, M. Lawson, T. Kissikov, B. T. Bush, A. Gallagher, K.-W. Chen, R. E. Baumbach, and N. J. Curro, "Nmr investigation of antiferromagnetism and coherence in  $\text{URu}_2\text{Si}_{2-x}\text{P}_x$ ", *Phys. Rev. B* **95**, 041107 (2017).
- <sup>88</sup>G. L. Chappell, A. Gallagher, D. E. Graf, P. Riseborough, and R. E. Baumbach, "Influence of hydrostatic pressure on hidden order, the kondo lattice, and magnetism in  $\text{URu}_2\text{Si}_{2-x}\text{P}_x$ ", *Phys. Rev. B* **102**, 245152 (2020).
- <sup>89</sup>A. Gallagher, W. L. Nelson, K. W. Chen, T. Besara, T. Siegrist, and R. E. Baumbach, "Single crystal growth of  $\text{uruzsiz}$  by the modified bridgman technique", *Crystals* **6**, 10.3390/cryst6100128 (2016).

- <sup>90</sup>E. Frantzeskakis, J. Dai, C. Bareille, T. C. Rödel, M. Güttler, S. Ran, N. Kanchanavatee, K. Huang, N. Pouse, C. T. Wolowiec, E. D. L. Rienks, P. Lejay, F. Fortuna, M. B. Maple, and A. F. Santander-Syro, "From hidden order to antiferromagnetism: electronic structure changes in fe-doped  $\text{URu}_2\text{Si}_2$ ", *Proceedings of the National Academy of Sciences* **118**, e2020750118 (2021).
- <sup>91</sup>F. L. Boariu, C. Bareille, H. Schwab, A. Nuber, P. Lejay, T. Durakiewicz, F. Reinert, and A. F. Santander-Syro, "Momentum-resolved evolution of the kondo lattice into "hidden order" in  $\text{URu}_2\text{Si}_2$ ", *Phys. Rev. Lett.* **110**, 156404 (2013).
- <sup>92</sup>W. Zhang, H. Y. Lu, D. H. Xie, W. Feng, S. Y. Tan, Y. Liu, X. G. Zhu, Y. Zhang, Q. Q. Hao, Y. B. Huang, X. C. Lai, and Q. Y. Chen, "Arpes/stm study of the surface terminations and  $5f$ -electron character in  $\text{URu}_2\text{Si}_2$ ", *Phys. Rev. B* **98**, 115121 (2018).
- <sup>93</sup>V. Jonsson, L. Piazza, M. Månsson, J. Weissenrieder, O. Tjernberg, S. Khartsev, Y. Sassa, D. G. Mazzone, N. Gauthier, M. Muntwiler, C. S. Ong, D. Lu şan, P. Thunström, and O. Eriksson, "Photoelectron dispersion in metallic and insulating  $\text{VO}_2$  thin films", *Phys. Rev. Research* **3**, 033286 (2021).



## List of Figures

2.1	The crystal field of octahedral ligands in some transition metal oxides lifts the degeneracy of the d orbitals. (a) Unit cell of $V_2O_3$ . Each Vanadium atom (yellow) is surrounded by an octahedron (blue) of Oxygen atoms (red). (b) The crystal field of octahedral ligands in some transition metal oxides like $V_2O_3$ lifts the degeneracy of the d orbitals and splits them into a doublet of d-orbitals pointing at the ligands forming the higher energy $e_g$ states, and the lower energy $t_g$ triplet pointing in between. Adapted from [5]. . . . .	10
2.2	Kondo's measurements for the resistivity (dots) of iron-doped gold wires and predicted logarithmic behaviour from his publication in 1964 [8]. The rise in resistivity at low temperatures is caused by conduction electrons interacting with the local magnetic moments of iron atoms. . . . .	12
2.3	The hybridization of a localized f-state (blue) and a nearly free state (orange) in k-space. The perturbation is strongest in the area of avoided crossing, where a narrow band-gap in the range of 10 meV opens between the hybridized states (green). Taken from [9]. . . . .	13
2.4	The Mott-metal-to-insulator transition. A partially filled d-band in the metallic phase (left) allows for conduction, but as repulsion increases, so does the energetic cost of electron proximity, and the band splits into 2 subbands (right): A fully filled lower Mott-band with one electron per lattice site, and a completely empty upper Mott-band representing a site with 2 electrons. Since electrons can only move into the unoccupied upper Mott-band, they become immobile without excitation. Figure taken from [11]. . . . .	14
2.5	Typical phase diagram for transitions between solid, liquid and gas phases in matter. The dashed line in green describes the special anomaly of water. Taken from [12]. . . . .	15
2.6	The crystal diagram of snow flakes as found by Nakaya [13]. Figure taken from [14] . . . . .	17
2.7	Schematic illustration of a quantum critical phase diagram with a transition from a normal (N) to an antiferromagnetic (A) region through the quantum critical point (D). For finite temperatures, the quantum critical region in orange expands in a V-shape. Figure adapted from [16]. . . . .	18

3.1	Energy levels involved in photoemission process. Electrons are excited to a final state at an energy $E_f$ that is $h\nu$ above their initial binding energy $E_B$ . When leaving the sample, the electron needs to overcome a potential barrier of the inner potential $V_0$ . Adapted from [25]	22
3.2	Schematic illustration of angle resolved photoelectron spectroscopy with the involved angles in the sample's system of reference.	26
3.3	A hemispherical electron analyser as used in most PES and ARPES experiments. The radial electric field in the half-sphere separates the electrons by kinetic energy. The emission angle is mapped in the direction perpendicular. Adapted from [28]	31
3.4	Illustration of the angles used to resolve the momenta in ARPES.	32
4.1	The crystal structure of $V_2O_3$ in ambient conditions. (a): The primitive unit cell (blue) is rhombohedral with 4 Vanadium- and 6 Oxygen atoms. The conventional unit cell (black) is hexagonal with the volume of three primitive cells. (b): The first Brillouin zone with base vectors and high symmetry points. The plane marked in red is parallel to the $(11\bar{2}0)$ surface of our samples and cutting through the $\Gamma$ -point.	34
4.2	Phase diagram of $V_2O_3$ . The horizontal axis marks hydrostatic pressure, the vertical axis the temperature. At ambient conditions, the system is a paramagnetic metal in a corundum structure (red area), and at low temperatures, it becomes an antiferromagnetic insulator with monoclinic structure (blue). At higher pressures, the transition temperature of these overlapping structural, magnetic and electronic transitions can be controlled by pressure until the low-temperature phase is suppressed at a quantum-critical point. At negative pressures, a third phase (green) of a paramagnetic insulator with Corundum structure occurs. It is not known if the electronic transition is completely separated from the structural and magnetic ones in this leftmost region of the phase diagram.	35
4.3	Crystal structure of $V_2O_3$ . (a) Unit cell in the Corundum phase. The conventional hexagonal cell is shown in black, the primitive cell is drawn in blue. (b) Visualisation of the change to the monoclinic phase to the structure. The cell gets sheared along the antiferromagnetic ordering vector, within the plane of hexagons in (a).	36
4.4	Rhombohedral and monoclinic Brillouin zones of $V_2O_3$ . (A) Comparison between the rhombohedral (red) and monoclinic (blue) Brillouin zones of $V_2O_3$ , corresponding respectively to the metallic and insulating phases. The xyz axes are also shown. (B, C) Same as (A) viewed from the x-side and y-side, respectively.	37

4.5	Resistance measured (2-point measurements) on a pristine $V_2O_3/Al_2O_3$ ( $11\bar{2}0$ ) thin film. Across the MIT, the resistance changes by more than seven orders of magnitude, and the transition shows a clear hysteresis, characteristic of first-order phase transitions. . . . .	37
4.6	Near-field infrared microscopy measurements by McLeod <i>et al.</i> from 2017, showing the evolution of domains across the transition. A strong infrared signal (red domains) corresponds to high metallicity, and the hysteretic behaviour across the transition is visible. The scale bars in (b) corresponds to $1\mu m$ and that in (c) to $5\mu m$ . Figure taken from [34]. . . . .	38
4.7	ARPES measurements by Lo Vecchio <i>et al.</i> from 2016. They identified an electron-like pocket around the $\Gamma$ -point, as seen in the magnified energy-momentum maps in (a) and(c) as well as the EDC-stack corresponding to (a) shown in (b). The entire E-k-dispersion shown in (d) shows the dispersive quasiparticle band at the Fermi level, to which this pocket belongs, the lower Mott-Hubbard band around $E_F - 1.5 eV$ , and the O $2p$ band from $E_F - 4eV$ down. Figure taken from [35]. . . . .	39
4.8	Photoelectron spectroscopy measurements on $V_2O_3$ by Mo <i>et al.</i> from 2003. In the V $3d$ region down close to $E_F$ , the QP peak and the MH band are visible. The inset shows the cuts through the reciprocal lattice of $V_2O_3$ for the photon energies they used for their work, with the dotted spectrum being measured at $h\nu = 700 eV$ while the continuous line is averaged over a range of $380 eV$ to $500 eV$ . Figure taken from [36]. . . . .	39
4.9	(A, B) LEED images of $V_2O_3/Al_2O_3$ ( $01\bar{1}2$ ) and $V_2O_3/Al_2O_3$ ( $11\bar{2}0$ ) films, respectively, obtained after <i>in-situ</i> annealing, right before ARPES measurements. . . . .	41
4.10	X-ray and resistance characterizations of the $V_2O_3$ films. (A, B) X-ray diffraction characterization, and (C) resistance measurements on a $V_2O_3/Al_2O_3$ ( $01\bar{1}2$ ) thin film used in some of our ARPES experiments (see Fig. 4.18 below), before (blue) and after (red) the in-situ annealing in UHV. Panel (B) is a zoom over the $V_2O_3$ and $Al_2O_3$ ( $01\bar{1}2$ ) peaks. (D, E) Analogous measurements to (B, C) on the $V_2O_3/Al_2O_3$ ( $11\bar{2}0$ ) thin films used in our ARPES experiments, before (green) and after (yellow) the in-situ annealing in UHV. . . . .	43

4.11 (A) Infrared reflectivity measurements for various temperatures (cooling cycle) in a pristine  $V_2O_3/Al_2O_3$  ( $01\bar{1}2$ ) thin film. (B) Zoom of the previous data over the low-energy excitations. (C, D) Similar to (A, B) on a sample of the same batch that was annealed in UHV prior to ARPES measurements. (E) Reflectivity at 370 meV as a function of temperature for both samples. All these data show that the MIT is still present in the annealed sample studied by ARPES, and the onset of the transition has just shifted down in temperature by about 15 K. . . . . 44

4.12 In-plane and out-of-plane Fermi surfaces in the metallic state of  $V_2O_3$ . (A) Rhombohedral 3D Brillouin zone of  $V_2O_3$ , showing the primitive vectors of the reciprocal lattice, together with a  $(\bar{1}10)$  plane (red) and a  $(11\bar{2})$  plane (light blue). These planes are, respectively, parallel and perpendicular to the surface of the studied  $V_2O_3/Al_2O_3$  ( $11\bar{2}0$ ) films. (B) Same in-plane Fermi surface map (metallic state at 180 K) of a  $V_2O_3/Al_2O_3$  ( $11\bar{2}0$ ). Red open markers show the experimental Fermi momenta with their respective error bars. Data were measured at 86 eV. (C) Out-of-plane Fermi-surface map (2D curvature) of the same sample. Blue open markers show the experimental Fermi momenta with their respective error bars. Data were acquired by varying the photon energy between 55 eV and 120 eV in steps of 0.5 eV using linear horizontal polarized light. . . . . 45

4.13 Raw ARPES energy-momentum maps in the metallic state of  $V_2O_3$ . (A) Same in-plane Fermi-surface map as shown in 4.12(B) indicating the path in reciprocal space for the raw ARPES energy-momentum maps in the metallic state (180 K) presented in panels (B, C). Data in (B) include the VB-top, MH/OV, QP and QLS bands. Panel (C) is a zoom of (B) over the MH/OV, QP and QLS features. . . . . 46

- 4.14 Energy-momentum maps (top: 2D curvature, bottom: raw data) along  $k_{\langle 111 \rangle}$  in the metallic (180 K) and insulating (100 K) states, respectively, showing four bands: an electron-like QP band at the Fermi level, visible at 180 K; a weakly dispersive QLS at  $E - E_F \approx -700$  meV, best observed at 100 K; a broad and weakly dispersing MH/OV band around  $E - E_F \approx -1.1$  eV, seen at both temperatures; and the VB of oxygen p states extending from  $E - E_F \approx -4$  eV downward, also present at all temperatures. The rhombohedral Brillouin zone edges ( $\pm Z$  points) at 180 K and the monoclinic zone edges at 100 K are indicated by red and blue dashed lines, respectively. (C,F) Momentum-integrated raw ARPES - intensities from (A,D) and (B,E), showing the QP, QLS, MH/OV, and VB states. All data were measured at a photon energy of 86 eV, corresponding to a bulk  $\Gamma$  point in the  $\langle 110 \rangle$  direction, using linear horizontal polarized light. . . . . 48
- 4.15 Reconstruction and hysteresis of the electronic structure across the MIT. (A to F) Evolution of the ARPES energy-momentum spectra near  $E_F$  (2D curvature of intensity maps) when cooling from 180 K (metallic state) to 60 K (insulating state) in a  $V_2O_3$  ( $11\bar{2}0$ ) thin film. The sharp pileup of intensity at  $E_F$  is a spurious effect of the 2D curvature analysis on the Fermi-Dirac cutoff. (G to K) Corresponding spectra when heating back to 180 K. The blue dashed parabolas in (A) and (K) represent a quasi-free electron band of effective mass  $m^* \approx 3.5m_e$ , assigned to the QP band. (L to V) Raw data associated to (A) to (K). Red and black markers indicate the positions of the QLS and MH/OV bands, respectively. . . . . 49
- 4.16 Temperature evolution of the spectra at  $\Gamma$  and  $\pm Z$ . (A, B) Energy distribution curves (EDCs) at  $\Gamma$  and  $\pm Z$  (integrated over  $0.03 \text{ \AA}^{-1}$  around each point) over, respectively, a cooling and a heating cycle across the MIT. (C, D) Thermal evolution (cooling and heating) of the EDCs only at the  $+Z$  point. All data in this figure correspond to the spectra shown in Fig. 4.15, including additional temperatures, for a  $V_2O_3/Al_2O_3$  ( $11\bar{2}0$ ) thin film. Spectra at the same temperature on opposite thermal cycles are shown in slightly different color hues, for clarity. . . . . 53

4.17	Fraction of metallic and insulating electronic domains from ARPES. (A) Representation of the fraction of insulating and metallic domains contributing to the ARPES intensity in a $V_2O_3/Al_2O_3$ (11 $\bar{2}$ 0) thin film. Error bars in the fits (Eq. (4.4)) are smaller than the size of the symbols. (B) Resistance as a function of temperature measured in the same sample after UHV annealing and photoemission experiments. The shift in transition temperature and the decrease of the resistivity in the insulating phase with respect to the pristine sample (Fig. 4.5) are ascribed to the slight doping with OVs induced by annealing in UHV (see 4.2.2).	55
4.18	Fraction of metallic and insulating electronic domains from ARPES. (A) Representation of the fraction of insulating and metallic domains contributing to the ARPES intensity in a $V_2O_3/Al_2O_3$ (01 $\bar{1}$ 2) film. Error bars in the fits (Eq. (4.4)) are smaller than the size of the symbols. (B) Resistance as a function of temperature measured in the same sample after UHV annealing and photoemission experiments.	55
4.19	(A) XPS spectrum of one of our $V_2O_3/Al_2O_3$ thin films (middle panel, red curve) after annealing in UHV during 5 min at 650 °C and performing ARPES measurements. The O-1s, V-2p <sub>1/2</sub> and V-2p <sub>3/2</sub> peaks are shown. The side feature of the O-1s peak at (532.68 ± 0.05) eV has been assigned to residual carbon contamination on the oxide surface [68]. The spectrum was fitted using four Lorentzians (blue curves) with a Shirley background (green curve). The fit residuals are shown in the top panel (black curve). The shoulder close to -513 eV seen in our data is a signature of the metallic correlated state of $V_2O_3$ [69]. (B) Reference XPS spectra of different stoichiometric vanadium oxides [68]. The overall shape and separation between the O-1s and V-2p <sub>3/2</sub> peaks in our data, namely 14.75 eV, is in excellent agreement with the ones of the reference spectra for $V_2O_3$ . (c) Zoom over the V-2p doublet for metallic vanadium and for different vanadium oxides, showing the characteristic energy shift of the peaks depending on the compound [70]. The energies of the V-2p peaks in our XPS spectrum correspond to the ones of $V_2O_3$ .	58
5.1	Crystal structure of URu <sub>2</sub> Si <sub>2</sub> . The symmetry is BCT with parameters $a = b = 4.15868 \text{ \AA}$ ; $c = 9.57253 \text{ \AA}$ and $\alpha = \beta = \gamma = 90^\circ$ . An easy cleaving plane exists between the Uranium atoms and the Silicon planes, perpendicular to the c-axis. The Silicon-terminated cleavage plane is marked in yellow. The first Uranium plane below that cleavage (bottom of this graph) will be called the near-surface layer (U1), with progressively bulk-like layers (U2, U3) below.	60

5.2	Reciprocal space symmetry of URu <sub>2</sub> Si <sub>2</sub> . The Brillouin zone corresponding to the crystal structure is drawn in red, and the Brillouin zone corresponding to the simple tetragonal lattice in the HO state, as observed by Bareille <i>et al.</i> in [74], is also drawn in black. Adapted from [74]. . . . .	61
5.3	Specific heat $C/T$ of URu <sub>2</sub> Si <sub>2</sub> as measured by Palstra <i>et al.</i> [72]. The divergence around $T_{HO}$ is clearly visible and indicates a second order phase transition. . . . .	62
5.4	Phase diagram of URu <sub>2</sub> Si <sub>2-x</sub> P <sub>x</sub> . The hidden order phase is marked in yellow and can be suppressed by doping with P in the Si sites. At $x \approx 0.03$ , the hidden order phase is completely suppressed, giving rise to a quantum critical point. Enclosed by the HO phase and marked in red is the superconducting phase, and with strong doping of $x \gtrsim 0.27$ , an antiferromagnetic phase starts to emerge (opaque red). Figure taken from [79]. . . . .	63
5.5	Phase diagram of URu <sub>2</sub> Si <sub>2</sub> as a function of pressure and temperature. The Hidden Order phase is marked in purple, the superconducting phase in green. If the HO phase is suppressed by pressure instead of P-doping, the system directly becomes antiferromagnetic (red), without passing through the paramagnetic phase (yellow, at higher temperatures). Figure taken from [80]. . . . .	63
5.6	The electronic structure across the temperature-induced hidden order transition around $\Gamma$ as measured by Bareille <i>et al.</i> The Fermi surface in the HO phase (a) and paramagnetic phase (b) in the center of the Brillouin zone is formed by an M-shaped band formed by interacting heavy and light states, visible in the energy-momentum maps along (010) (c,g) and (110) (d,i) (all second derivatives). (e,f,i,j) show the raw EDCs corresponding to these dispersions. In the vicinity of the $\Gamma$ -point, a heavy quasiparticle band forms an additional Fermi surface contour that in the Hidden Order state is shaped like 4 petals along (100) and (010), as visible in (a) In the high-temperature phase in (b), these petals are linked, forming a diamond-shape. Figure taken from [74]. . . . .	65
5.7	DFT calculations of the electronic structure of URu <sub>2</sub> Si <sub>2</sub> by Elgazzar <i>et al.</i> [85] predict a change in the Fermi surface around the $\Gamma$ -point, transitioning from a diamond-shaped structure in the PM phase (blue) to petals along the main axis in the HO phase (red). . . . .	66
5.8	ARPES spectra around the $\Gamma$ -point of URu <sub>2</sub> Si <sub>2</sub> measured by Santander-Syro <i>et al.</i> in [84] (figure adapted). As the temperature decreases through $T_{HO}$ , a heavy quasi-particle band (marked by red arrows) appears and crosses the Fermi energy from above. . . . .	66

- 5.9 (a) Reference spectrum of the Si 2*p* corelevel spectrum for Si (green) and U (red) terminated surfaces from [90]. (b) Si 2*p* corelevels for our doped sample ( $x = 0.07$ ). The strong similarity with the Si-terminated spectrum from (a) suggests the same termination on our sample. All spectra were measured with nominal photon energies of 151.5 eV, corresponding to the third harmonics of the monochromator set up for 50.5 eV. The mismatch of  $\sim 200$  meV between the Si-terminated spectrum in (a) and the spectrum in (b) could be explained by a difference in monochromator alignment of  $\sim 100$  meV. . . . . 68
- 5.10 (a-c) In-plane Fermi-surface map of a pure URu<sub>2</sub>Si<sub>2</sub> single crystal (a) in the hidden order state ( $T = 1.4$  K), as well as the  $x = 0.07$  phosphorous-doped specimen (b) in the paramagnetic phase and the  $x = 0.27$  doped sample (c) in the antiferromagnetic state at the same temperature. Pronounced differences in intensity along (110) around the  $\Gamma$ -point are in accordance with previous observations of a temperature-induced phase transition in the pure compound. The ST Brillouin zone is drawn in red for orientation. In the hidden order state (a), the Fermi surface forms four petals around  $\Gamma$ , while in the paramagnetic state (b), these petals are linked, forming a diamond structure. In (c) the petals seem to widen and be separate again. (d) Energy-momentum dispersion (second derivative) along (110) through the  $\Gamma$ -point as marked by a dashed green line in (b). A heavy quasiparticle band with U5-f character is dispersing close to the Fermi level and crossing above it at  $\pm 0.3 \text{ \AA}^{-1}$ , creating the diamond-like Fermi surface. . . . . 70
- 5.11 The changes around the X-point in the first Brillouin zone (border marked in red) through the doping-induced HO-transition. The dispersions along (010) through X are shown in (a) to (c) and are marked as green lines in the corresponding Fermi surface maps in (d) to (f). In the energy-momentum maps, a strongly dispersing hole-like band, likely from a surface state, and a heavy electron band are evolving with the doping. With increased doping, the light hole band shifts down in energy, and hybridization with the heavy band gets visibly suppressed. Note that the spectral weight of the heavy band in (a) is enhanced in the region enclosed by the LHB by the hybridization. In the Fermi surface in the hidden order state (d), at least two contours are resolved around X, made up of buckles with a gap at the center. Neither of these has a circular shape as would be expected for non-interacting bands. Such a circular shape is present for the doped sample out of the hidden order phase in (e) and (f). . . . . 72

6.1	In the phase diagram of $V_2O_3$ , a pure metal-to-insulator transition, unmixed with structural and magnetic changes, should occur along the arrow in bright yellow. . . . .	75
9.1	An example of a 2D cut with complex symmetry, the $(11\bar{2}0)$ cut of $V_2O_3$ at an out-of-plane wave-vector that does not cross the $\Gamma$ point at normal emission. In this region of the Brillouin zone, the shape and symmetry of the cut across the Brillouin zone changes drastically with small changes in in the out-of-plane direction. . . .	81
9.2	Window for creating reciprocal space lattice data . . . . .	82
9.3	Plotting the first BZ border into a 2D FS map. When comparing the symmetry, the angle is not quite correct. The user can then rapidly change the angle of the BZ border to make it correspond to the symmetries of the measured 2D map. . . . .	83
9.4	Plotting the 3-dimensional BZ and the configured cut in a Gizmo plot. . . . .	84
10.1	Reconstruction et hystérésis de la structure électronique à travers la TMI. (A à F) Évolution des spectres énergie-quantité de mouvement ARPES près de $E_F$ (courbure 2D des cartes d'intensité) lors du refroidissement de 180 K (état métallique) à 60 K (état isolant) dans une couche mince de $V_2O_3$ $(11\bar{2}0)$ . Le fort empilement d'intensité à $E_F$ est un effet parasite de l'analyse de la courbure 2D sur la coupure de Fermi-Dirac. . . . .	107
10.2	Fraction des domaines électroniques métalliques et isolants à partir de l'ARPES. (A) Représentation de la fraction des domaines métalliques et isolants contribuant à l'intensité ARPES dans une couche mince $V_2O_3/Al_2O_3$ $(11\bar{2}0)$ . Les barres d'erreur dans les ajustements (Eq. (4.4)) sont plus petites que la taille des symboles. (B) Résistance en fonction de la température mesurée dans le même échantillon après le recuit en UHV et les expériences de photoémission. . . . .	108

- 10.3 (a-c) Carte de la surface de Fermi dans le plan d'un monocristal de  $\text{URu}_2\text{Si}_2$  pur (a) dans l'état d'ordre caché ( $T = 1,4\text{ K}$ ), ainsi que de l'échantillon dopé légèrement au phosphore (b) dans la phase paramagnétique et de l'échantillon fortement dopé (c) dans l'état antiferromagnétique à la même température de  $1,4\text{ K}$ . Dans l'état d'ordre caché (a), la surface de Fermi forme quatre pétales autour du point  $\Gamma$ , tandis que dans l'état paramagnétique (b), ces pétales sont liés, formant une structure en diamant. En (c), les pétales semblent s'élargir et être à nouveau séparés. (d) Dispersion énergie-quantité de mouvement (dérivée seconde) le long de (110) en passant par le point  $\Gamma$  marqué par une ligne pointillée verte en (b). Une bande de quasi-particules lourdes à caractère U5-f se disperse près du niveau de Fermi et passe au-dessus à  $\pm 0,3\text{ \AA}^{-1}$ , créant la surface de Fermi en forme de diamant. . . . . 109
- 10.4 Les changements autour du point X dans la première zone de Brillouin (frontière marquée en rouge) par la transition HO induite par le dopage. Les dispersions le long de (010) à travers X sont montrées dans (a) à (c) et sont marquées par des lignes vertes dans les cartes de surface de Fermi correspondantes dans (d) à (f). Dans les cartes d'énergie-quantité de mouvement, une bande de type trou fortement dispersée, provenant probablement d'un état de surface, et une bande d'électrons lourds évoluent avec le dopage. Avec l'augmentation du dopage, la bande de trou légère se déplace vers le bas en énergie, et l'hybridation avec la bande lourde est visiblement supprimée. Notez que le poids spectral de la bande lourde dans (a) est augmenté dans la région entourée par la BTL par l'hybridation. Dans la surface de Fermi dans l'état d'ordre caché (d), au moins deux contours sont résolus autour de X, constitués de boucles avec un espace au centre. Aucun de ces contours n'a une forme circulaire comme on pourrait s'y attendre pour des bandes non interagissantes. Une telle forme circulaire est présente pour l'échantillon dopé hors de la phase d'ordre caché dans (e) et (f). . . . . 110

## 10 - Synthèse en Français

### 10.1. Motivation

Avec la découverte de la mécanique quantique, la physique a rencontré un défi fondamental: Les scientifiques ont réalisé que la complexité énorme d'un grand nombre de particules en interaction était prohibitive pour une telle approche, et l'idée d'un modèle rendant l'univers évident à toutes les échelles a dû être abandonnée. L'hypothèse réductionniste, selon laquelle quelques principes fondamentaux dictent la physique à toutes les échelles, n'est pas invalidée pour autant et est presque incontestée parmi les physiciens. L'utilité des lois fondamentales pour prédire le comportement des grands systèmes est toutefois fortement limitée, ce qui a poussé les scientifiques à rechercher d'autres approches pour faire de telles prédictions. Cette recherche a conduit à l'émergence de la physique statistique et de la physique à N corps, et la notion de traitement des phénomènes collectifs comme un nouveau type de physique est décrite de manière concise dans le célèbre dicton de Philip W. Anderson "More is different" (Plus, c'est différent).

La puissance du concept de physique à plusieurs corps est illustrée par la façon dont les progrès de la puissance de calcul des dernières décennies ont non seulement été utilisés pour la résurgence des méthodes *ab-initio*, mais ont également conduit à l'essor de la théorie dynamique du champ moyen en tant qu'outil prévalent et au développement de techniques expérimentales, telles que la spectroscopie de photoémission à résolution angulaire, pour aborder les aspects fondamentaux des systèmes à plusieurs corps quantiques et mécaniques.

Cette thèse s'occupe de deux de ces phénomènes émergents: La transition métal-isolant dans  $V_2O_3$  et les transitions de phase quantiques dans  $URu_2Si_2$ .

### 10.2. Cadre Théorique

Dans la théorie des bandes classique, les interactions entre les électrons sont négligées. Selon théorème de Bloch, les solutions pour un Hamiltonian du modèle des liaisons fortes sont les états propres avec la même périodicité que le potentiel du réseau cristallin. Des propriétés de ces états peuvent être décrits comme des quasi-particules (électrons et trous) dont l'énergie  $E$  disperse avec le vecteur d'onde  $\vec{k}$ .

En outre, dans la théorie des bandes classique on définit les métaux et les isolants par l'occupation des bandes à dans l'état fondamental à 0 Kelvin, où les électrons disponibles remplissent progressivement les bandes: Si la dernière bande d'énergie occupée est partiellement remplie, le matériau sera métallique, par contre, si elle est totalement remplie, le matériau sera isolant.

Cette théorie des bandes n'est plus valable dans les matériaux avec une forte

interaction entre les électrons. Un exemple pour les effets d'une telle interaction est donné par la transition métal-isolant de Mott, où la répulsion des électrons dans la même bande entraîne la division de cette bande en deux parties séparées par un gap d'énergie. Un deuxième effet d'interaction est l'hybridation entre des bandes qui interagissent, et l'ouverture d'un petit gap entre les états hybridés, comme vu dans l'effet Kondo.

Les systèmes d'électrons fortement corrélés peuvent présenter différents états fondamentaux concurrents, conduisant à des transitions de phase vers des états exotiques de la matière. Notamment, les transitions de phase à la température de 0 K présentent un intérêt fondamental, car la transition ne peut pas progresser par des excitations thermiques, mais par les incertitudes quantiques. Une telle transition entraîne l'apparition d'un point critique quantique dans le diagramme de phase.

Cette thèse se sert principalement de la photoémission résolue en angle (ARPES) pour explorer les changements de structure électronique à travers deux transitions de phase paradigmatiques des matériaux corrélés. ARPES utilise l'effet photoélectrique pour imager les mesurer occupées (ou plus précisément, la fonction spectrale) dans un échantillon en fonction de leur vecteur d'onde  $\vec{k}$  et leur énergie.

### 10.3. $V_2O_3$

Dans le  $V_2O_3$  volumique, une transition métal-isolant (TMI) de premier ordre se produit à une température de transition de  $T_{TMI} \approx 160$  K, caractérisée par une forte augmentation de la résistivité de plus de 6 ordres de grandeur et l'ouverture d'un gap électronique d'environ 750 meV au niveau de Fermi.

Dans les conditions ambiantes, le  $V_2O_3$  forme des cristaux paramagnétiques avec une symétrie rhomboédrale. La transition métal-isolant est accompagnée par l'apparition d'antiferromagnétisme et un changement vers une structure monoclinique. Jusqu'à présent, la question si la transition antiferromagnétique cause la transition électronique par un gap créé par le pliage était ouverte. Dans des études antérieures, les domaines de la taille de quelques micromètres formés pendant la transition ont été observés parmi autres techniques par microscopie en champ-proche en infrarouge, et des expériences en spectroscopie des photoélectrons ont montré une bande de quasi-particule électronique au niveau de Fermi dans l'état métallique, ainsi que la bande basse de Mott-Hubbard à 1,1 eV en dessous de  $E_F$ .

Cette thèse présente une étude complète des changements de la structure électronique à travers la TMI induite par la température dans des films de  $V_2O_3$  avec une épaisseur d'environ 100 nm, dont l'intégrité cristalline, contrairement aux monocristaux, n'est pas affectée par la transition. Les films étaient déposés sur un substrat de  $Al_2O_3$  avec une surface en  $(11\bar{2}0)$  ou  $(01\bar{1}2)$ , transportés hors vide aux synchrotron SOLEIL ou KEK-PF, et recuits *in situ* pour les nettoyer avant les expériences d'ARPES. Les résultats montrent des bandes dispersives de quasi-

particules et de Mott-Hubbard dans l'état métallique, ainsi que des signatures spectrales uniques, différentes de celles d'une instabilité conventionnelle de la surface de Fermi, accompagnant la TMI: l'ouverture d'un gap au niveau de Fermi, associé à une diminution du poids spectral de la bande de quasi-particules, sans aucun changement de sa masse effective. La bande de Mott-Hubbard reste par ailleurs non affectée par la TMI. Le poids spectral de la bande de quasi-particules est transféré à une bande non dispersive, de caractère orbital différent, dont l'énergie de liaison diminue à mesure que son poids spectral augmente. En outre, les données montrent une hystérésis thermique dans la gap et le poids spectral de la bande de quasi-particule, ce qui est interprété en termes de l'évolution de la concentration des domaines microscopiques métalliques/isolants, et qui capture quantitativement l'hystérésis de la résistivité mesurée dans les mêmes échantillons.

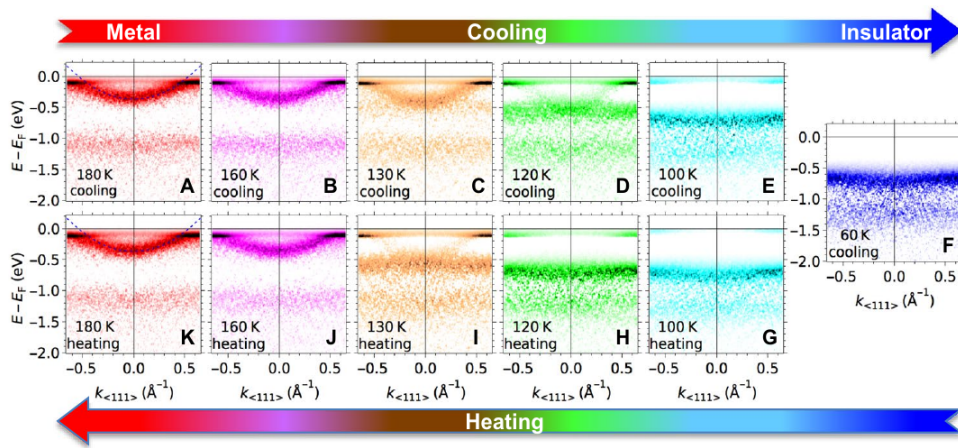


Figure 10.1: Reconstruction et hystérésis de la structure électronique à travers la TMI. (A à F) Évolution des spectres énergie-quantité de mouvement ARPES près de  $E_F$  (courbure 2D des cartes d'intensité) lors du refroidissement de 180 K (état métallique) à 60 K (état isolant) dans une couche mince de  $V_2O_3$  ( $1\ 1\ \bar{2}\ 0$ ). Le fort empilement d'intensité à  $E_F$  est un effet parasite de l'analyse de la courbure 2D sur la coupure de Fermi-Dirac.

#### 10.4. $URu_2Si_2$

L' $URu_2Si_2$  subit quant à lui une transition de phase à 17,5 K, dont le paramètre d'ordre est encore inconnu trois décennies après sa première observation dans des mesures de chaleur spécifique. La température de transition peut être abaissée par un dopage au phosphore jusqu'à sa suppression totale à un point critique quantique. Un dopage encore plus fort donne naissance à un état fondamental antiferromagnétique. Les transitions induites par le dopage sont intéressantes d'un point de

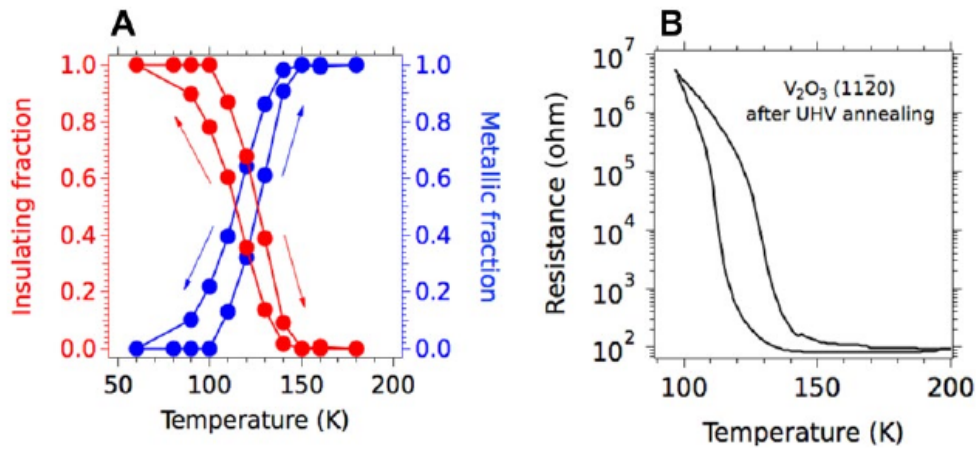


Figure 10.2: Fraction des domaines électroniques métalliques et isolants à partir de l'ARPES. (A) Représentation de la fraction des domaines métalliques et isolants contribuant à l'intensité ARPES dans une couche mince  $V_2O_3/Al_2O_3$  ( $11\bar{2}0$ ). Les barres d'erreur dans les ajustements (Eq. (4.4)) sont plus petites que la taille des symboles. (B) Résistance en fonction de la température mesurée dans le même échantillon après le recuit en UHV et les expériences de photoémission.

vue fondamentale: Une transition de phase continue au zéro absolu implique une criticité quantique, où la transition vers le nouveau état fondamental ne peut pas être induite par des excitations thermique comme dans les transitions de phase conventionnelles, et nécessite plutôt les fluctuations quantiques du point zéro dues à l'incertitude d'Heisenberg. Cette thèse présente des mesures ARPES de la structure électronique de l' $URu_2Si_2$  à travers les transitions à température constante depuis l'ordre caché (HO) vers la phase paramagnétique (PM) et ensuite vers la phase antiferromagnétique (AFM) induites par le dopage au phosphore. Il est constaté que les changements de la structure électronique autour du point Gamma entre ces phases s'apparentent à ceux rapportés précédemment pour les transitions HO-PM-AFM purement induites par la température.

De plus, au point X, nous observons que le dopage en phosphore induit des changements importants dans la dispersion d'un état de surface de type trou et la suppression de son hybridation avec la bande de quasi-particules U-5f dans l'état paramagnétique, contrairement au cas de la transition induite par la température, indiquant qu'une telle hybridation est une caractéristique unique de la phase d'ordre caché. la bande de trou légère se déplace vers le bas en énergie sans changement de sa masse effective.

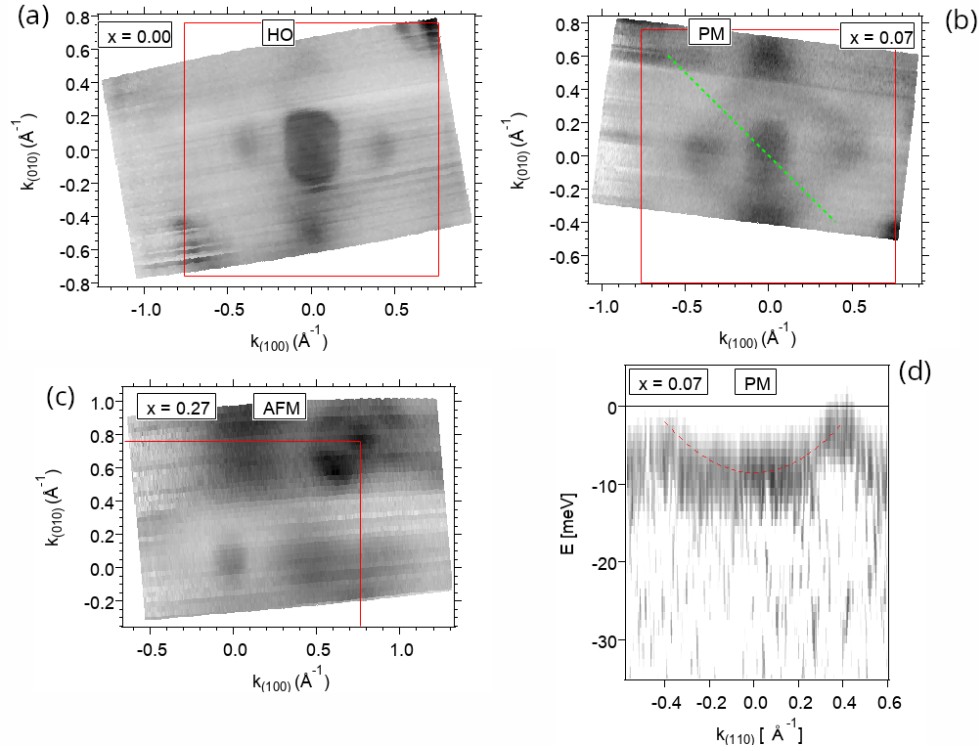


Figure 10.3: (a-c) Carte de la surface de Fermi dans le plan d'un monocristal de  $\text{URu}_2\text{Si}_2$  pur (a) dans l'état d'ordre caché ( $T = 1,4 \text{ K}$ ), ainsi que de l'échantillon dopé légèrement au phosphore (b) dans la phase paramagnétique et de l'échantillon fortement dopé (c) dans l'état anti-ferromagnétique à la même température de  $1,4 \text{ K}$ . Dans l'état d'ordre caché (a), la surface de Fermi forme quatre pétales autour du point  $\Gamma$ , tandis que dans l'état paramagnétique (b), ces pétales sont liés, formant une structure en diamant. En (c), les pétales semblent s'élargir et être à nouveau séparés. (d) Dispersion énergie-quantité de mouvement (dérivée seconde) le long de (110) en passant par le point  $\Gamma$  marqué par une ligne pointillée verte en (b). Une bande de quasi-particules lourdes à caractère  $U_5-f$  se disperse près du niveau de Fermi et passe au-dessus à  $\pm 0,3 \text{ \AA}^{-1}$ , créant la surface de Fermi en forme de diamant.

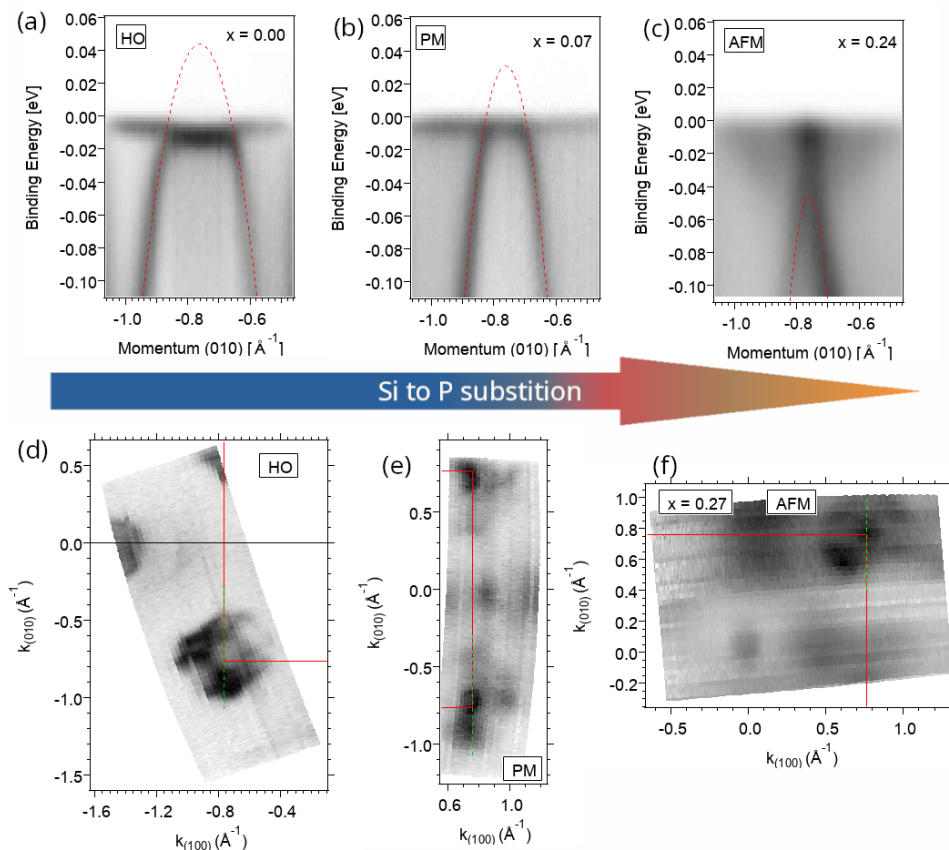


Figure 10.4: Les changements autour du point X dans la première zone de Brillouin (frontière marquée en rouge) par la transition HO induite par le dopage. Les dispersions le long de (010) à travers X sont montrées dans (a) à (c) et sont marquées par des lignes vertes dans les cartes de surface de Fermi correspondantes dans (d) à (f). Dans les cartes d'énergie-quantité de mouvement, une bande de type trou fortement dispersée, provenant probablement d'un état de surface, et une bande d'électrons lourds évoluent avec le dopage. Avec l'augmentation du dopage, la bande de trou légère se déplace vers le bas en énergie, et l'hybridation avec la bande lourde est visiblement supprimée. Notez que le poids spectral de la bande lourde dans (a) est augmenté dans la région entourée par la BTL par l'hybridation. Dans la surface de Fermi dans l'état d'ordre caché (d), au moins deux contours sont résolus autour de X, constitués de boucles avec un espace au centre. Aucun de ces contours n'a une forme circulaire comme on pourrait s'y attendre pour des bandes non interagissantes. Une telle forme circulaire est présente pour l'échantillon dopé hors de la phase d'ordre caché dans (e) et (f).